ER-5997

December 1962

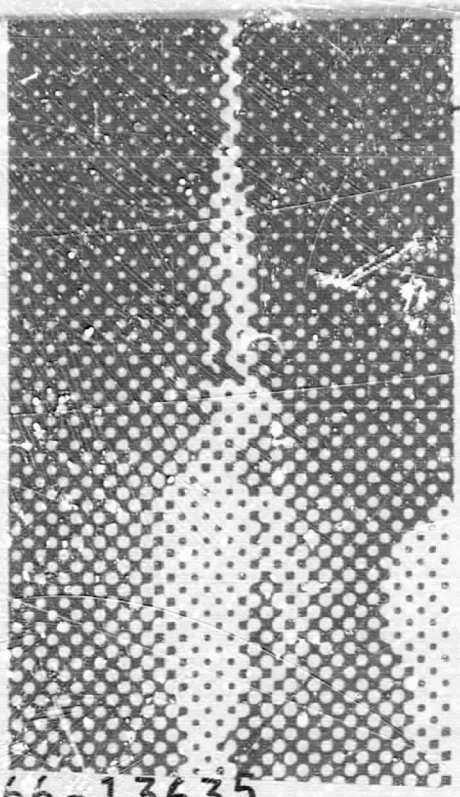

SHIELDING PROBLEMS in MANNED SPACE VEHICLES

NASA CONTRACT NAS8-879

NUCLEAR

ER-5997
December 1962

SHIELDING PROBLEMS IN MANNED SPACE VEHICLES

prepared by: W. M. Schofield
E. C. Smith
C. W. Hill

prepared for: GEORGE C. MARSHALL SPACE FLIGHT CENTER
NATIONAL AERONAUTICS AND SPACE ADMINISTRATION
HUNTSVILLE, ALABAMA
NASA CONTRACT NAS8-879

LOCKHEED NUCLEAR PRODUCTS
Lockheed-Georgia Company
A Division of Lockheed Aircraft Corporation
Marietta, Georgia

If this document is supplied under the requirements of a United States Government contract, the following legend shall apply unless the letter "U" appears in the coding box:

This data is furnished under a United States Government contract and only those portions thereof which are marked (for example, by circling, underscoring or otherwise) and indicated as being subject to this legend shall not be released outside the Government (except to foreign governments, subject to these same limitations), nor be disclosed, used, or duplicated, for procurement or manufacturing purposes, except as otherwise authorized by contract, without the permission of Lockheed-Georgia Company, A Division of Lockheed Aircraft Corporation, Marietta, Georgia. This legend shall be marked on any reproduction hereon in whole or in part.

The "otherwise marking" and "indicated portions" as used above shall mean this statement and includes all details or manufacture contained herein respectively.

Code: U	Contract: NAS8-879

FOREWORD

This report is submitted to the George C. Marshall Space Flight Center, National Aeronautics and Space Administration, Huntsville, Alabama, in accordance with the requirements of Contract NAS8-879.

BLANK PAGE

TABLE OF CONTENTS

		Page
FOREWORD		i
TABLE OF CONTENTS		iii
LIST OF FIGURES		v
LIST OF TABLES		xi
1.0	INTRODUCTION	1
2.0	RIGIDITY THEORY AND SPECTRUM PHYSICS	3
2.1	Electromagnetic Effect on Space Radiation	3
2.2	Conversion Code	7
2.3	Trapping Theory	12
2.4	Solar Flare Physics	23
2.5	Flares of Particular Interest	33
2.6	References	55
3.0	NUCLEAR DATA COMPILATION	57
3.1	Introduction	57
3.2	Elementary Particles	57
3.3	Nuclear Reaction Models	63
3.4	Nucleon-Nucleon Cross Sections	73
3.5	Nucleon-Nucleus Cross Sections	77
3.6	Pions and Pion Reactions	91
3.7	References	97
4.0	RADIATION PENETRATION CODES	119
4.1	Electron Bremsstrahlung	119
4.2	Proton Penetration Calculations	122
4.3	Evaporation Neutron Dose	131
4.4	Monoenergetic Spectrum	136
4.5	Isotropic Flux	142

TABLE OF CONTENTS (Continued)

		Page
4.6	Use of LPPC Results	152
4.7	References	158
5.0	SUMMARY AND CONCLUSION	161
5.1	Radiation Sources	161
5.2	Radiation Transport	161
APPENDIX I		163
APPENDIX II		169
APPENDIX III		185

LIST OF FIGURES

Figure		Page
2-1	Proton Time-of-Flight from Sun to Earth	4
2-2	Charged Particle in a Magnetic Field	5
2-3	Proton Rigidity Vs Proton Kinetic Energy	8
2-4	Charged Particle in a Uniform Magnetic Field	14
2-5	Charged Particle in a Nonuniform Magnetic Field	14
2-6	Charged Particle Drift Normal to Magnetic Field & Field Gradient	15
2-7	Charged Particle Drift Normal to Magnetic Field & Field Gradient	16
2-8	Mirror Reflection of Charged Particle in Convergent Magnetic Field	17
2-9	Dipole Solenoidal Field	18
2-10	Charged Particle Trapped in a Flux Tube	19
2-11	The Guiding Center Orbit	20
2-12	Meridian Plane Projection of the Motion of a Charged Particle Trapped in a Flux Tube	21
2-13	Charged Particle Motion in a Dipole Field	22
2-14	Temporal Distortion of the Sub-Surface Solar Magnetic Field Lines	24
2-15	Verticle Distribution of Solar Field Lines	25
2-16	Undistorted Solar Magnetic Field	27
2-17	Vertical Distortion of Solar Magnetic Field Prior to Flare	27

LIST OF FIGURES (Continued)

Figure		Page
2-18	Solar Magnetic Lines Associated with a Flare	28
2-19	Coriolus Effect on Solar Magnetic Lines Associated with a Flare	28
2-20	Solar Magnetic Bottle	29
2-21	Charged Particle Motion in Solar Magnetic Bottle	29
2-22	Flare Area and Importance	32
2-23	Solar Proton Differential Energy Spectra, Normalized to 1 HAO (by t^{-2})	34
2-24	Solar Proton Differential Energy Spectrum, 23 February 1956, 1 HAO	37
2-25	Solar Proton Differential Energy Spectrum, 10 May 1959, 33.0 HAO	40
2-26	Solar Proton Differential Energy Spectrum, 14 July 1959, 31.5 HAO	43
2-27	Solar Proton Differential Energy Spectrum, 3 September 1960	47
2-28	Solar Proton Differential Energy Spectrum, 12 November, 1960, 5.17 HAO	50
2-29	Solar Proton Differential Energy Spectrum, 15 November 1960, 41.3 HAO	53
3-1	Goldberger Constant K Versus Bombarding Energy	65
3-2	Proton Wave Length	67
3-3	Differential Elastic Scattering of 85 Mev Neutrons	69

LIST OF FIGURES (Continued)

Figure		Page
3-4	Diffraction Scattering	70
3-5	Half Value Angle Diffraction Scattering	71
3-6	Proton-Proton Cross Sections	74
3-7	n-p and p-n Cross Sections	75
3-8	Total Cross Section as a Function of Energy	81
3-9	Total Cross Section as a Function of Mass Number	82
3-10	Nonelastic Cross Section as a Function of Mass Number	86
3-11	Nonelastic Cross Section as a Function of Energy	87
3-12	Energy Spectrum of Protons Scattered from Carbon (C.M.)	90
3-13	π^+-P Total Cross Sections	94
3-14	π^--P Total Cross Sections	95
4-1	Integral Electron Spectrum in the Outer Trapped Belt	120
4-2	Electron Bremsstrahlung Dose Vs Thickness for a Typical Trajectory Through the Van Allen Radiation Belts	123
4-3	Proton Dose Vs Thickness for a Typical Trajectory Thru the Inner Van Allen Radiation Belt	124
4-4	Upper Bound and Best Estimate of Fast Nucleon Doses	130
4-5	Dose Rate Per Unit Flux Vs Energy	140

LIST OF FIGURES (Continued)

Figure		Page
4-6	Dose Rate Per Unit Flux Vs Energy	141
4-7	Differential Dose Rate for a Freden-White Spectrum	143
4-8	Differential Dose Rate for a Freden-White Spectrum	144
4-9	Differential Dose for a Flare Spectrum	145
4-10	Differential Dose for a Flare Spectrum	146
4-11	Geometry of Evaporation Neutron Source Calculation	149
4-12	Relative Angular Dose Emerging from Shield Thickness X Versus Cos θ for Monoenergetic Isotropic Flux	151
4-13	Plane Geometry Dose	153
4-14	Spherical Geometry Dose	154
4-15	Plane Geometry Evaporation Neutron Dose	156
II-1	Dosage as a Function of Thickness	170
II-2	Dosage as a Function of Thickness	171
II-3	Dosage as a Function of Thickness	172
II-4	Dosage as a Function of Thickness	173
II-5	Dosage as a Function of Thickness	174
II-6	Dosage as a Function of Thickness	175
II-7	Dosage as a Function of Thickness	176
II-8	Dosage as a Function of Thickness	177
II-9	Dosage as a Function of Thickness	178

LIST OF FIGURES (Continued)

Figure		Page
II-10	Dosage as a Function of Thickness	179
II-11	Dosage as a Function of Thickness	180
II-12	Dosage as a Function of Thickness	181
II-13	Dosage as a Function of Thickness	182
II-14	Dosage as a Function of Thickness	183
II-15	Dosage as a Function of Thickness	184

BLANK PAGE

LIST OF TABLES

Table		Page
2-1	Importance Values Recommended by IAU	31
2-2	Flare Data	35
2-3	Solar Flare, 23 February 1956	38
2-4	Solar Flare, 10 May 1959	41
2-5	Solar Flare, 14 July 1959	44
2-6	Solar Flares, 3 September 1960	48
2-7	Solar Flare, 12 November 1960	51
2-8	Solar Flare, 15 November 1960	54
3-1	Elementary Particles	59
3-2	Reaction Thresholds	63
3-3	Total Cross Sections	78
3-4	Differential Elastic Cross Sections	83
3-5	σ_{ne} (barns)	85
3-6	$\frac{d^2\sigma}{dEd\Omega}$	89
3-7	Quasi Elastic (p, 2p) Scattering	92
I-1	Dose Angular Distributions - Water	164
I-2	Dose Angular Distributions - Carbon	165
I-3	Dose Angular Distributions - Aluminum	166
I-4	Dose Angular Distributions - Iron	167
I-5	Dose Angular Distributions - Tungsten	168

1.0 INTRODUCTION

Man is the most radiosensitive component in manned spacecraft systems. The necessity of providing radiation protection for personnel in space vehicles imposes restrictions on vehicle design, on mission planning, and especially on payload capability. Previous studies have shown that high thrust escape trajectories through the trapped radiation belts impose modest shielding requirements. However, solar flares may present severe hazards to manned space flights.

It is difficult to assess the flare hazard because of limited data on flux densities and frequency of occurrence. Moreover, it is unlikely that sufficient data will become available in the next few years to permit reliable statistical analyses to be made. Therefore, it seems advisable to investigate the causes and mechanisms of flare production in the hope that understanding of the process will lead to estimates of flare frequency and upper limits on particle fluxes. A discussion of flares is included in this report.

Space radiations incident on material shields produce secondary radiations which may rival or exceed the dose due to primary radiations. A discussion of nuclear interactions is included in this report together with a data compilation which may serve as an introduction to phenomena in the high energy range.

Methods of calculating radiation transport through shields, including secondaries, are discussed and the results of some sample calculations are presented.

The authors wish to acknowledge the assistance of R. G. Allen, W. B. Ritchie, and K. M. Simpson. The authors are also indebted to C. C. Douglass for programming the radiation transport codes.

BLANK PAGE

2.0 RIGIDITY THEORY AND SPECTRUM PHYSICS

2.1 ELECTROMAGNETIC EFFECT ON SPACE RADIATION

In considering the charged particles that cause a radiation problem in space, the study of such charged particles in an electromagnetic field is most essential. The protons and electrons trapped in the earth's magnetic field and the charged particles from a solar flare both suffer unusual motion due strictly to magnetic fields. It is, therefore, necessary to have some knowledge of the equations of motion of charged particles in an electromagnetic field as well as the vernacular associated with this knowledge.

Of special interest is the time of flight from the sun to the earth of energetic particles. In Figure 2-1 the minimum time of flight of protons from the sun to the earth versus energy is given. This plot is derived from the equation

$$t = \frac{d(T + m_o c^2)}{c\sqrt{T^2 + 2Tm_o c^2}} \qquad 2\text{-}1$$

where d is the distance to the sun, T is the kinetic energy, m_o is the rest mass of the particle, and c is the velocity of light.

The next quantity of interest to space radiation is called the magnetic rigidity. One explanation of magnetic rigidity starts with the equation for the Lorentz force:

$$\vec{F} = q\left\{ \vec{E} + \frac{1}{c} (\vec{v} \times \vec{B}) \right\} \qquad 2\text{-}2$$

which is the force on a charge q, with direction and velocity $\vec{v}$, moving in an electric field $\vec{E}$ and a magnetic field $\vec{B}$. The rigidity was originally designed to describe the motion of a charged particle in the magnetic field only, so that the term qE in Equation 2-2 is zero. Furthermore, $\vec{v}$ is taken perpendicular to $\vec{B}$ so that Equation 2-2 reduces to

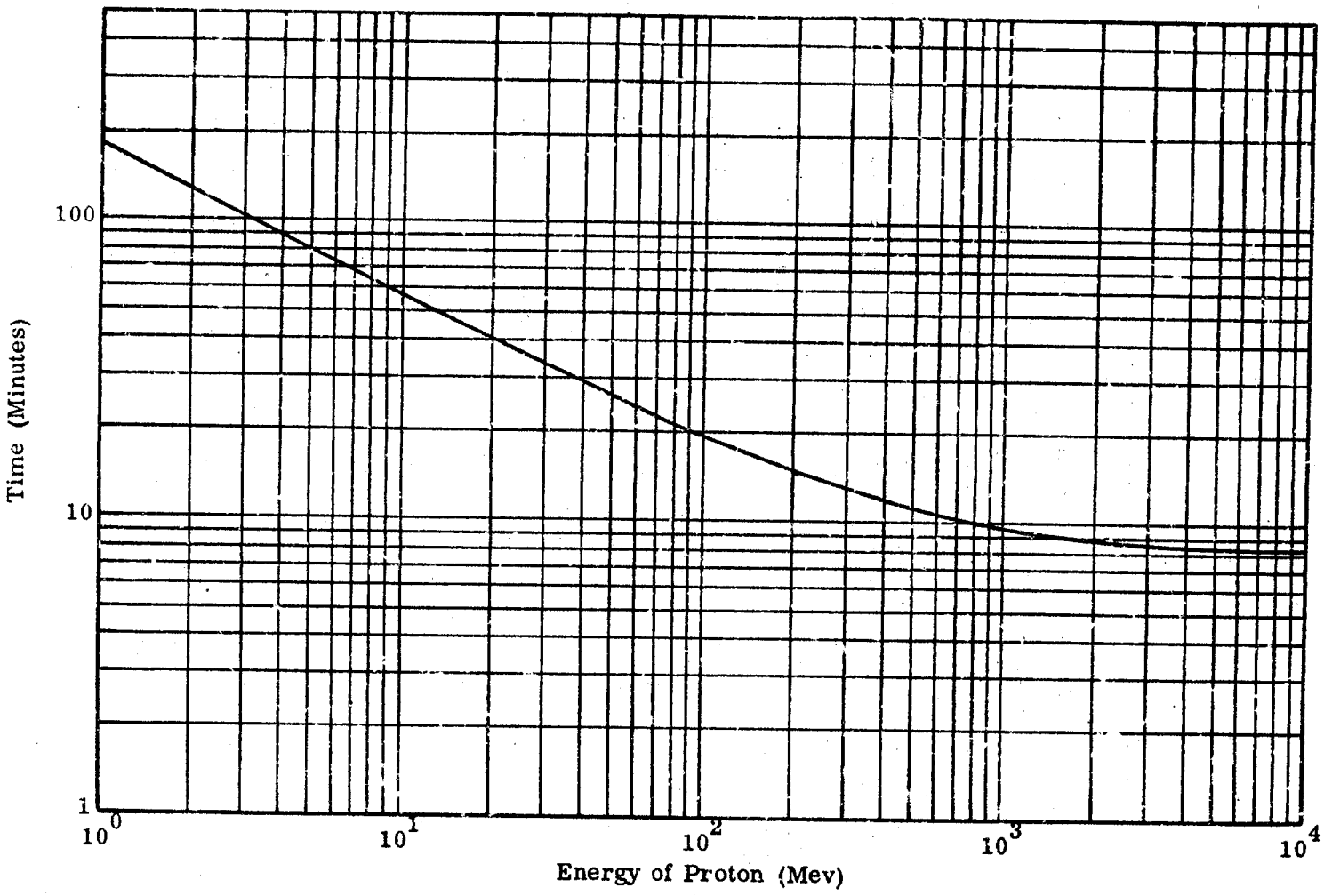

FIGURE 2-1 PROTON TIME-OF-FLIGHT FROM SUN TO EARTH

$$F = \frac{q}{c}(vB) \qquad 2\text{-}3$$

where v and B are the scalar values of $\vec{v}$ and $\vec{B}$. The centrifugal force and the Lorentz force are equal and opposite for the charged particle q in a magnetic field, see Figure 2-2, where t is the trajectory;

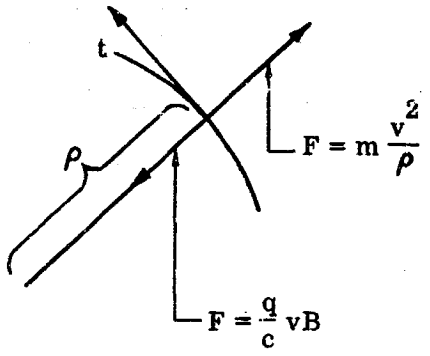

FIGURE 2-2 CHARGED PARTICLE IN A MAGNETIC FIELD

thus,

$$\frac{mv^2}{\rho} = \left(\frac{q}{c}\right)(vB) \qquad 2\text{-}4$$

where ρ is the radius of curvature. Equation 2-4 reduces to

$$mv = \frac{q}{c} B\rho \qquad 2\text{-}5$$

where m is the relativistic mass. Since mv is the relativistic momentum, this may be written as

$$pc = qB\rho \qquad 2\text{-}6$$

where p is momentum.

The charge q for atomic particles is given by $q = Ze$, so that

$$pc = ZeB\rho \qquad 2\text{-}7$$

Since the velocities involved approach those of the speed of light, relativistic conditions prevail. Hence,

$$E = T + E_o = \frac{m_o c^2}{\sqrt{1 - \beta^2}}; \qquad 2\text{-}8$$

$$T = \frac{m_o c^2}{\sqrt{1 - \beta^2}} - m_o c^2; \qquad 2\text{-}9$$

$$p = \frac{m_o v}{\sqrt{1 - \beta^2}}; \qquad 2\text{-}10$$

where E = total energy;

T = kinetic energy;

$E_o = m_o c^2$ = rest energy,

$\beta = v/c$.

Equation 2-8 can be written as

$$E = \sqrt{m_o^2 c^4 + \frac{m_o^2 v^2 c^2}{1 - \beta^2}} \qquad 2\text{-}11$$

or simply from Equation 2-10

$$E = \sqrt{p^2 c^2 + m_o^2 c^4} \qquad 2\text{-}12$$

From 2-8 and 2-12, one has

$$T + m_o c^2 = \sqrt{p^2 c^2 + m_o^2 c^4} \qquad 2\text{-}13$$

which, on squaring and solving yields

$$pc = \sqrt{T^2 + 2T\, m_o c^2} \qquad 2\text{-}14$$

Equation 2-7 may be written as

$$R = B\rho = \frac{pc}{Ze}, \qquad 2\text{-}15$$

where the quantity R is called magnetic rigidity and is related to the radius of curvature of the trajectory of (Ze) in a field B.

The relativistic equation for R is found by combining Equations 2-14 and 2-15 to give

$$R = B\rho = \frac{\sqrt{T^2 + 2T\, m_o c^2}}{Ze} \qquad 2\text{-}16$$

If T and $m_o c$ are in ergs and Ze in esu, then R will be in gauss-cms. If T and $m_o c^2$ are in Mev and Ze in number of electron charges, then R will be in Mv (million volts). For a positive charge, the trajectory is turned in the direction of the vector $\vec{v} \times \vec{B}$; for a negative charge, the trajectory is turned in the direction of $\vec{B} \times \vec{v}$. Solving Equation 2-16 for T gives

$$T = \sqrt{(R\, Ze)^2 + m_o^2 c^4} - m_o c^2 \qquad 2\text{-}17$$

Equation 2-17 is quite useful and values have been tabulated in UCRL 2426 where graphs of $H\rho$ vs T are given. (There $H\rho$ is rigidity measured in gauss-inches.) A plot of rigidity in Mv vs kinetic energy in Mev is given in Figure 2-3.

2.2 CONVERSION CODE

The Lockheed Source Spectrum Converter (LSSC) is written in FORTRAN to facilitate preparation of proton input spectra in a format suitable for the Lockheed Proton Penetration Code (LPPC).

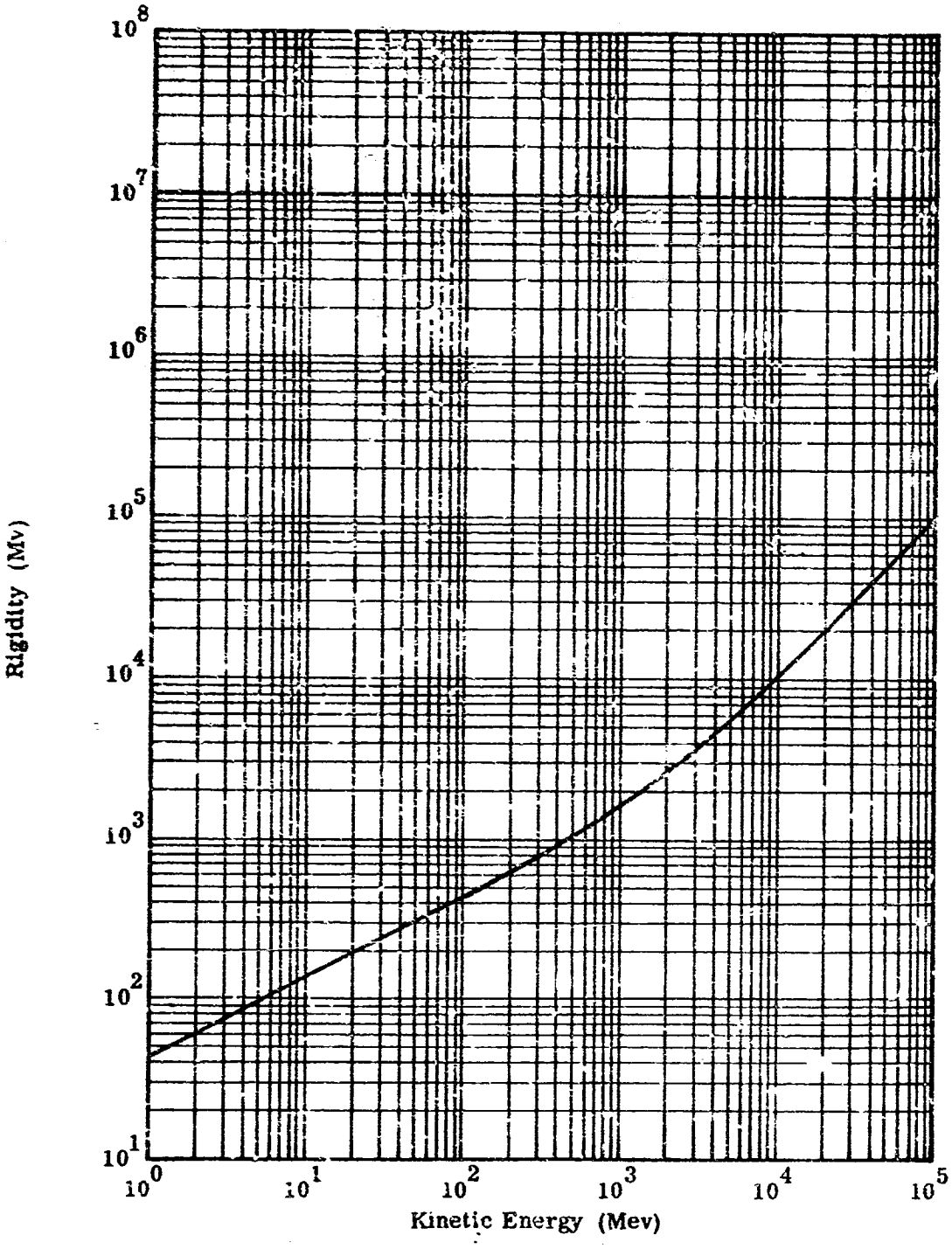

FIGURE 2-3 PROTON RIGIDITY VS PROTON KINETIC ENERGY

Space radiation fluxes reported in the literature are presented in a variety of ways and it is often difficult to reduce them to a common form suitable for comparison and calculation. LSSC is intended to eliminate the laborious hand calculations involved in reducing a given spectrum to a differential energy spectrum. Its principal feature is a systematic (not necessarily accurate) method of differentiating tabulated integral spectra. In practice, LSSC has been found satisfactory for converting trapped and solar flare spectra in the energy range of interest for space shielding, provided that some caution is used in the preparation of input data.

At present, LSSC may be used to convert five types of proton spectral data to the differential energy form. These types are listed below:

Option 1 - Integral rigidity spectrum

Option 2 - Integral energy spectrum

Option 3 - Differential rigidity spectrum

Option 4 - Integral rigidity power law spectrum

Option 5 - Integral energy power law spectrum

Option 1:

In this option, a table of rigidity values and their corresponding integral rigidity fluxes are read into the computer. The rigidities are converted to energies by means of Equation 2-18.

$$E = \sqrt{(Re)^2 + 938^2} - 938 \qquad 2\text{-}18$$

where E represents kinetic energy in Mev, R represents rigidity in Mv, and e represents proton charge (=1.).

The data are now effectively a table of integral energy fluxes versus energy and are treated as such by switching control to Option 2. The comments under Option 2 relating to optimum choice of input data values, to ensure stability, apply to this option also.

Option 2:

The code reads energy values and the corresponding integral energy fluxes. LSSC next reads two cards containing nine quantities which define the output energies for the differential energy flux. The nine quantities are named EMAX, EMIN, EB1, EB2, DEL1, DEL2, DEL3, and DEL4. The output energy values are computed in the following way. EMIN is the lowest energy. Succeeding energies are obtained by adding DEL1 until EB1 is reached or passed. Then DEL2 is added until EB2 is reached or passed. This procedure is folled until EMAX is reached or 250 energy points are computed. Thus, the energy mesh for the output points is divided into four or fewer ranges with constant intervals within each range. This method of defining output energy points is used in Option 1, 2, 4 and 5 since these options all proceed through Option 2.

The integral energy spectrum is assumed to be represented by an analytic power function in the interval E_i to $E_i + 1$:

$$F(E) = \frac{C}{D - 1} E^{1 - D}, \quad E_i \leq E \leq E_{i+1} \qquad 2\text{-}19$$

By definition

$$\frac{d}{dE} F(E) = -f(E) \qquad 2\text{-}20$$

Differentiating 2-20 one obtains the differential energy spectrum,

$$f(E) = CE^{-D} \qquad 2\text{-}21$$

From Equation 2-19

$$C = (D - 1) \frac{F(E)}{E^{1 - D}} \qquad 2\text{-}22$$

An expression for D is obtained by evaluating Equation 2-19 at the end points.

$$D = 1 - \frac{\ln \left\{ F(E_i)/F(E_{i+1}) \right\}}{\ln \left\{ E_i/E_{i+1} \right\}} \qquad 2\text{-}23$$

Substituting Equations 2-22 and 2-23 in Equation 2-21, the differential energy spectrum is:

$$f(E) = \frac{F(E)}{E} \cdot \frac{\ln\left\{F(E_i)/F(E_{i+1})\right\}}{\ln\left\{E_i/E_{i+1}\right\}}, \quad E_i \leq E \leq E_{i+1} \qquad 2\text{-}24$$

Equation 2-24 is evaluated numerically; F(E) is obtained by polynomial interpolation in the log of E and F(E) table. Special provisions are made at those energy points where the size of the energy interval changes.

Option 2 occasionally produces small oscillations in the output spectrum but is more satisfactory than a numerical or graphical differentiation scheme. This is especially true when crude graphs of integral fluxes are to be analyzed. If Option 1 or 2 is used, it is suggested that the values of F(E) be replotted and a smooth curve drawn. Then 5 to 15 (maximum of 50) points may be read off the graph. The replotted data are not more accurate than the original, but fluctuations caused by errors in reading coarse interval graphs are minimized.

The derivative is very sensitive to random fluctuations. For this reason, points should be selected so that differences between successive flux and energy values are large, compared to the graph reading error. All runs should be examined to determine that the solution is satisfactory.

Option 3:

The spectrum converter code reads a table of differential rigidity flux versus rigidity. Rigidity is transformed to energy according to Equation 2-18. The integral flux is transformed as:

$$f(E) = F(R)\,\frac{\sqrt{R^2 + 938^2}}{R} \qquad 2\text{-}25$$

In this option only, the output energy points correspond to the input rigidity points, one to one.

Option 4:

The integral rigidity flux according to a power law is given in Equation 2-26.

$$F(R) = AR^{-B} \qquad 2\text{-}26$$

The code reads A, B, and a table of rigidities. The flux at each rigidity is computed using Equation 2-26. The rigidities are converted to energies using Equation 2-18. Control is then transferred to Option 2.

Option 5:

The integral energy flux according to a power law is given in Equation 2-27.

$$F(E) = AE^{-B} \qquad 2\text{-}27$$

The code reads A, B, and a table of energies. The flux at each energy is computed using Equation 2-27. Control is then transferred to Option 2

A FORTRAN listing of LSSC is given in Appendix III. TRINTF is a Lockheed trapezoidal integration subroutine. Other subroutines may be obtained through SHARE.

2.3 TRAPPING THEORY

Charged particles entering the magnetic field of the earth from outer space undergo a curvature of their trajectory. Since rigidity is related to curvature, it is possible to calculate the energy of a particle if its rigidity can be measured. One of the properties of the earth's field is that the closer an energetic particle approaches to the geomagnetic equator, the greater the rigidity required for the particle to penetrate the earth's magnetic field. As a particle approaches the geomagnetic pole this rigidity value decreases until at the pole the necessary value is zero. Furthermore, since an increase in altitude also decreases the rigidity requirement, it is possible to obtain a more complete rigidity spectrum through the use of balloon or rocket flights. It is common to give spectra in

terms of integral rigidity since it is relatively easy to measure particles with a rigidity in excess of a certain value. For example, all the particles arriving at a certain global point will have a rigidity in excess of a certain given value which is determined by their global position.

The object of this section is to give a heuristic explanation of the effects of a planetary magnetic field on charged particles. For individuals who wish to probe deeper and obtain a mathematical model, references are given in Section 2.6.

In the cases of the sun and the earth, charged particles spiral along magnetic lines connected to the respective astronomical body. The manner in which these lines occur is quite different in the case of the sun (see Section 2.4) from that of the earth. The magnetic lines around the earth are due to its magnetic dipole and are, to a first order approximation, relatively stable in time. This is not the case for some of the solar lines. They form with a flare and in time increase in size while becoming weaker, perhaps even breaking loose from the sun.

Because it is considerably easier to describe the case of the earth first and then extend this case to that of the sun (see Section 2.4), a hypothetical model from which both could be developed will not be used.

From elementary electromagnetic theory, consider the case of a charged particle traversing a uniform parallel magnetic field. According to the Lorentz force which is given by Equation 2-3, the particle will suffer a transverse force. There are two perturbations that will result in a distortion of the purely circular motion which would exist if the field were perfectly straight and parallel. These perturbations produce a drift of the particle.

If a magnetic field is as shown in Figure 2-4 and a charged particle traverses the field at right angles, then its path is curved as stated previously. If the field is not uniform, but decreases in strength as shown in Figure 2-5, the particle will describe a trajectory with ever increasing radius of curvature. If the particle

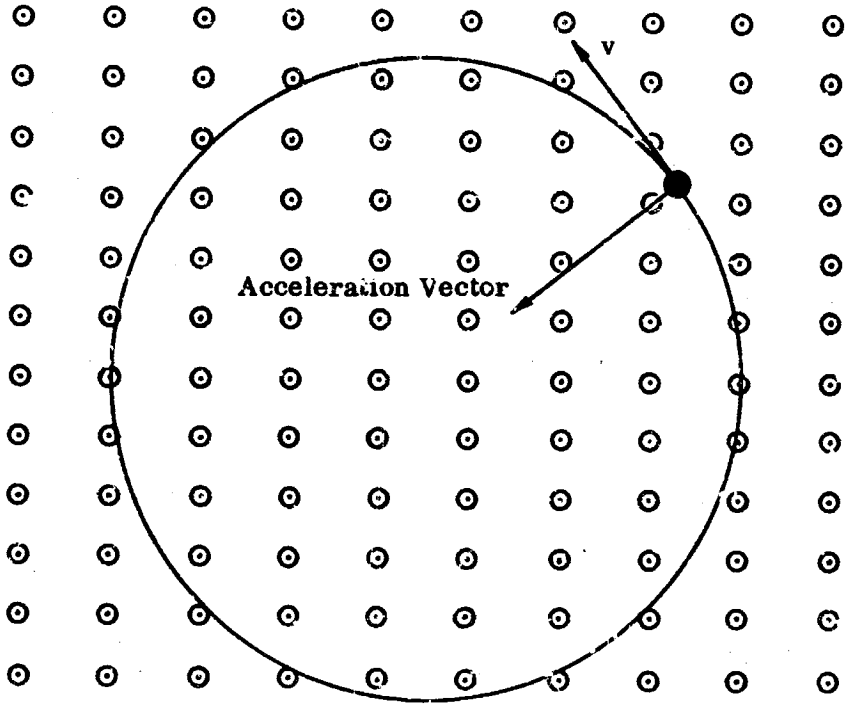

FIGURE 2-4 CHARGED PARTICLE IN A UNIFORM MAGNETIC FIELD

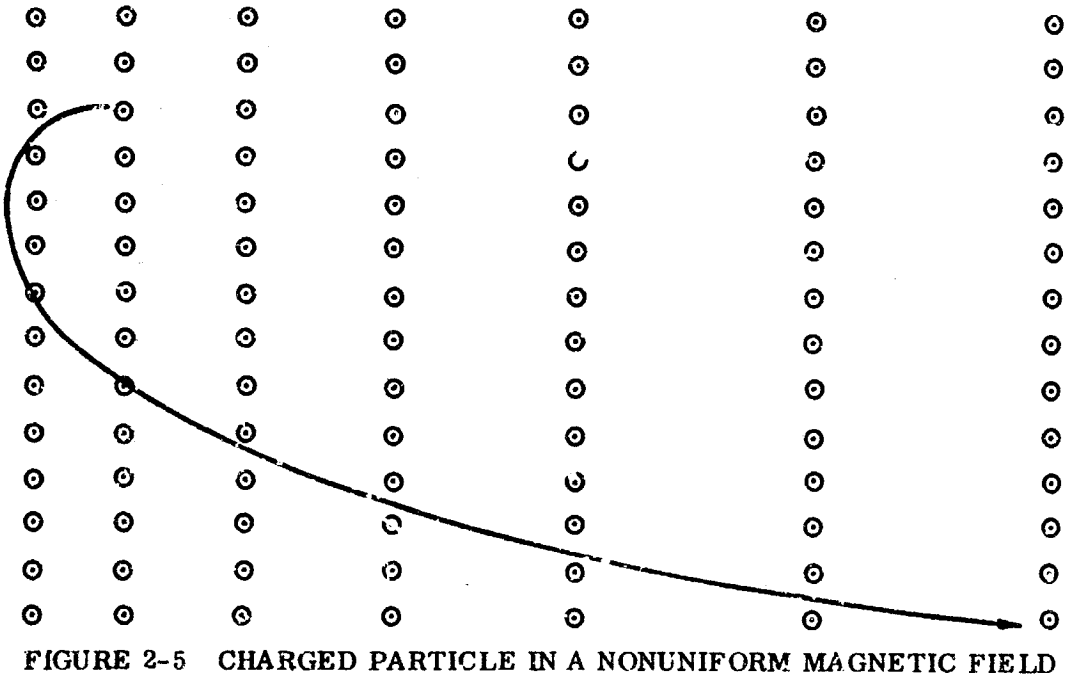

FIGURE 2-5 CHARGED PARTICLE IN A NONUNIFORM MAGNETIC FIELD

path turns past the normal to the field gradient, the particle will again enter the denser part of the field, shortening its radius of curvature. The result is a drift of the particle normal to both the field (B) and the quantity $\nabla_{\perp}B$ as shown in Figure 2-6 and Figure 2-7, where $\nabla_{\perp}B$ is the component of the gradient of B which is perpendicular to B. A second drift results from convergence of the field lines as shown in Figure 2-8.

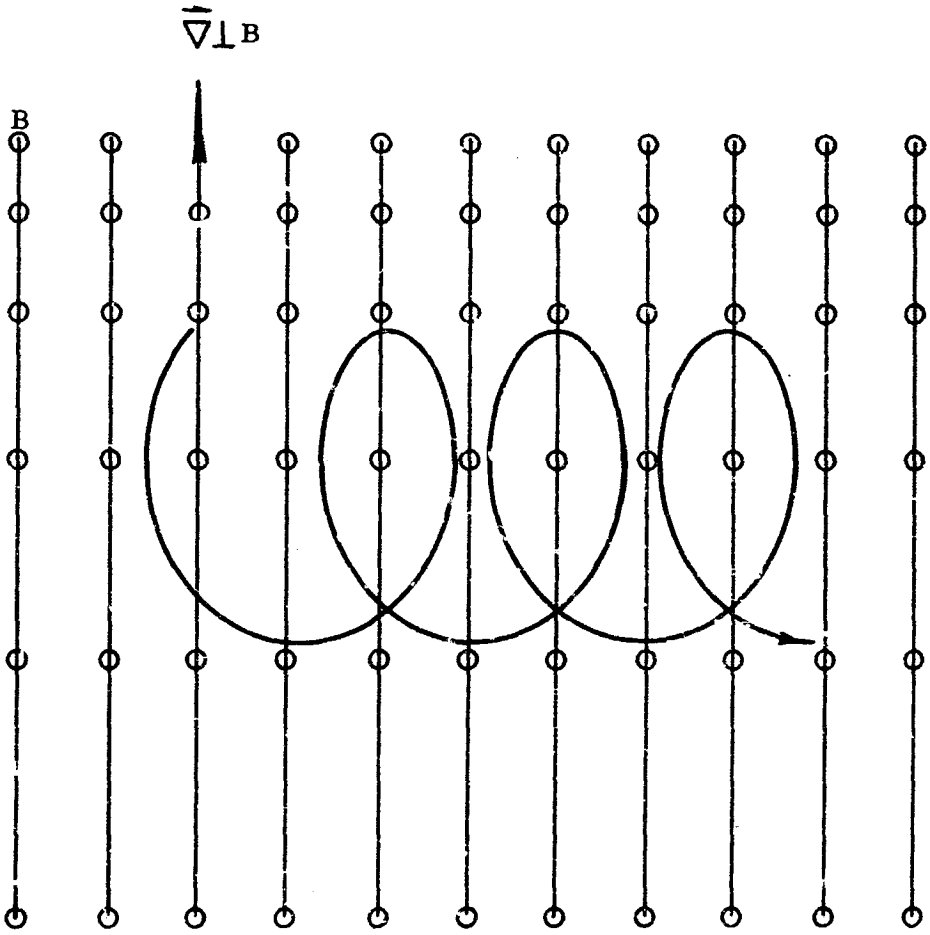

FIGURE 2-6 CHARGED PARTICLE DRIFT NORMAL TO MAGNETIC FIELD & FIELD GRADIENT

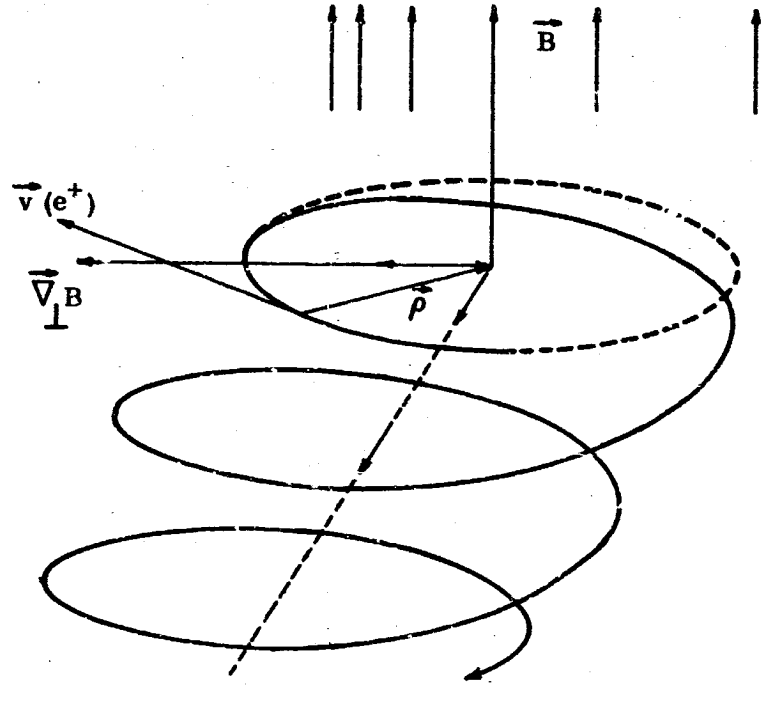

FIGURE 2-7 CHARGED PARTICLE DRIFT NORMAL TO MAGNETIC FIELD AND FIELD GRADIENT

Consider a charged particle following the path P. If the particle is proceeding in the +Z direction, as it cuts the converging lines B, it develops a -Z component as shown by f_z. This tends to decrease its +Z velocity, finally reversing the particle at the mirror plane M-M'. The axis of the motion is called the guiding center as shown in Figure 2-8.

Since the earth itself is one of the best models available, its magnetic dipole solenoidal field will be discussed first. The dipole field is shown in Figure 2-9. For those who will wish to delve further into the theory, the starting point will be the vector potential for a magnetic dipole,

$$\vec{A} = - \vec{\mu} \times \nabla(1/r) \qquad 2\text{-}28$$

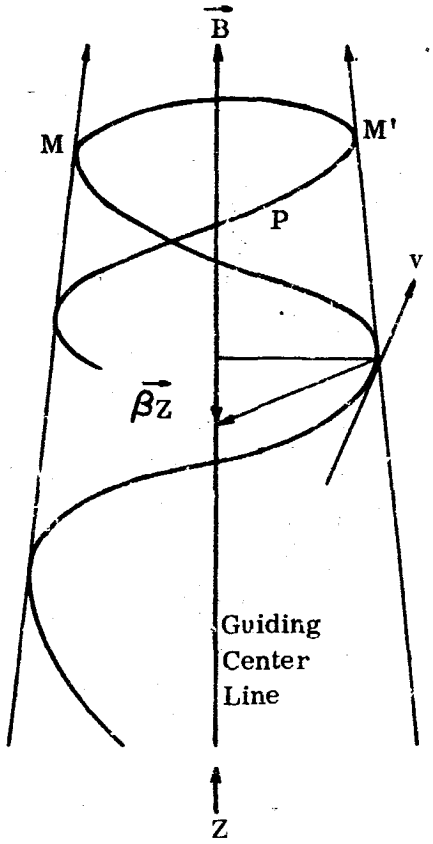

FIGURE 2-8 MIRROR REFLECTION OF CHARGED PARTICLE IN CONVERGENT MAGNETIC FIELD

Here $\vec{\mu}$ is magnetic dipole moment and is given numerically by

$$|\vec{\mu}| = 8.091 \times 10^{25} \text{ ergs/gauss}$$

The vector basis for the derivation is given in earth geomagnetic coordinates (ζ, λ, r) by the unit vectors ($\vec{e_\zeta}$, $\vec{e_\lambda}$, $\vec{e_r}$). Maxwell's equations then give for the magnetic field strength:

$$\vec{H} = \nabla \times \vec{A} = \frac{|\mu|}{r^3}\left[(\cos\lambda)\vec{e_\lambda} - (2\sin\lambda)\vec{e_r}\right] \qquad 2\text{-}29$$

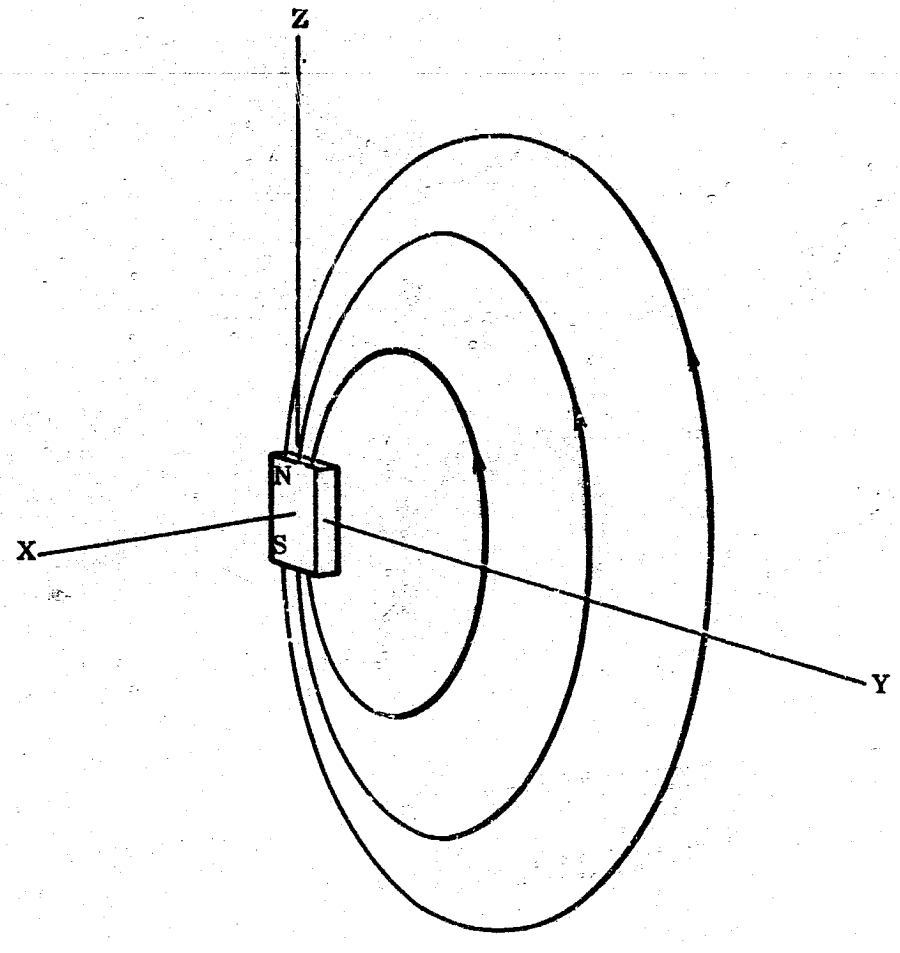

FIGURE 2-9 DIPOLE SOLENOIDAL FIELD

The details of the vector potential and the derivation of the field strength is given in the works of Fermi[F1]. The details of the curl formula, application and reduction, have been passed over, but can readily be found[S1].

Because the earth field line density varies with distance from the dipole and also since the field lines are curved, the particle

spirals about the guiding center line which follows the field lines. Furthermore, the drift velocity is a function of position with respect to the equatorial plane. The guiding center drift velocity is greatest at the equatorial plane, and as the particle moves toward a pole, this drift velocity decreases until finally the particle reverses its drift direction at a point called a mirror point as shown in Figure 2-10. It then travels through the flux tube to a conjugate mirror point near the other pole.

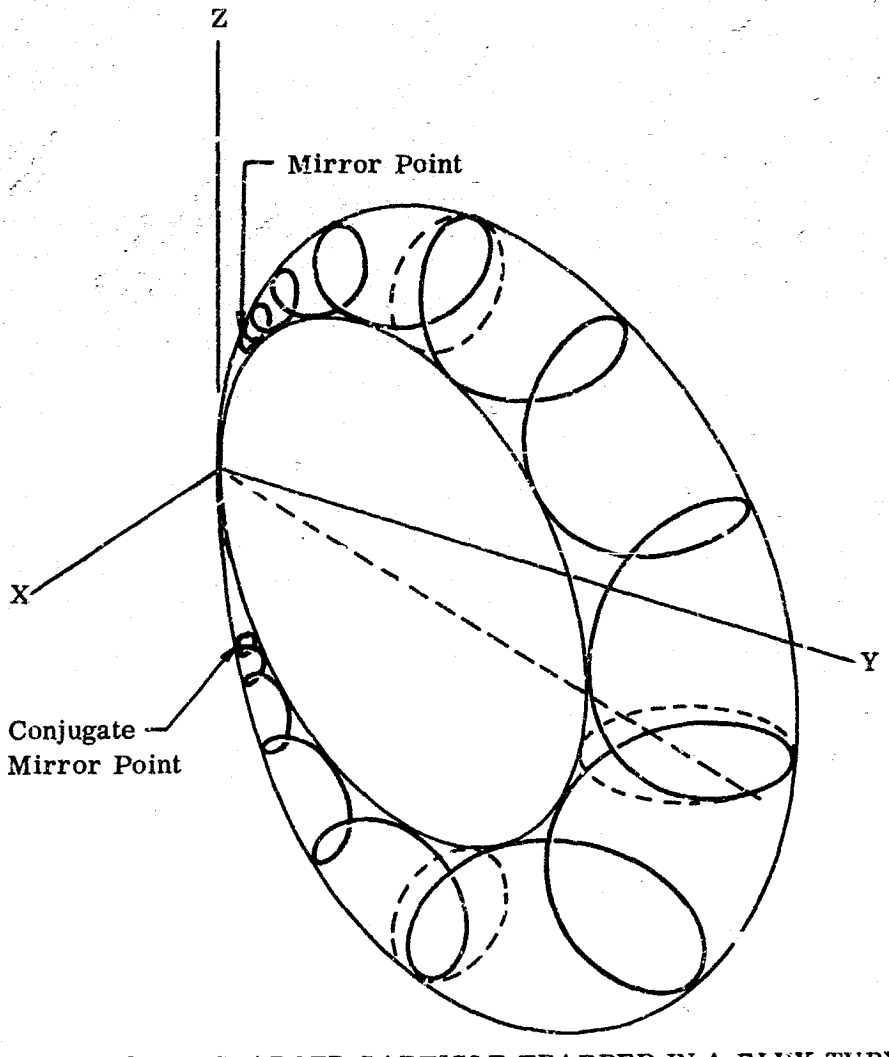

FIGURE 2-10 CHARGED PARTICLE TRAPPED IN A FLUX TUBE

The superposition of the drift along the guiding center with that due to change in magnetic line density, with change in distance from the center of the earth, gives a compound drift to terrestrially trapped radiation as shown in Figure 2-11. In this figure, the guiding center on the dipole shell is shown for trapped particles. The net result is a drift to the east for electrons and a drift to the west for protons.

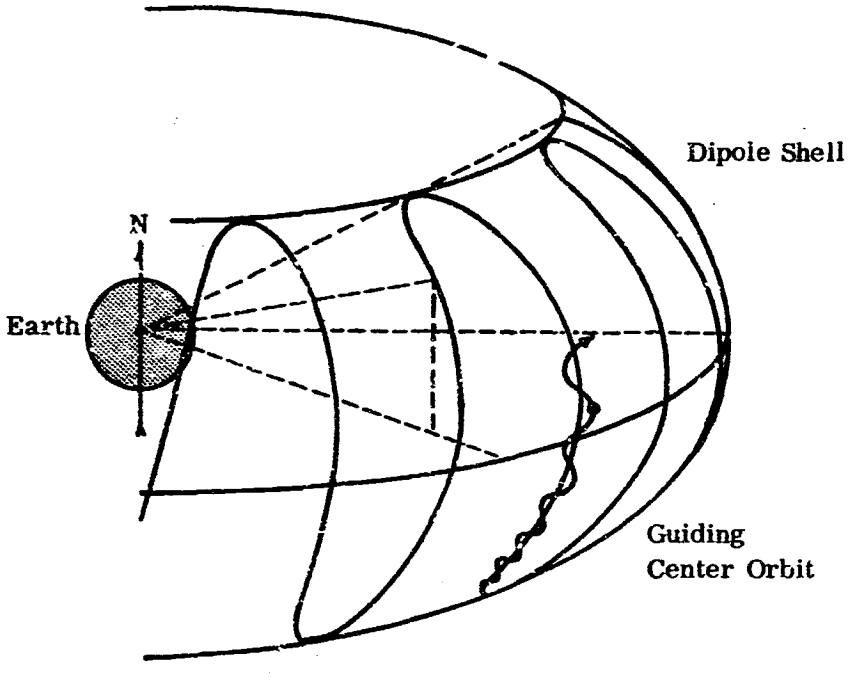

FIGURE 2-11 THE GUIDING CENTER ORBIT

This radiation has been spoken of as trapped. It is now apparent why. Once the particle is injected into a tube to spiral, it is very difficult for the particle to escape, the motion being such as to confine the particle to a flux tube as shown in Figure 2-12.

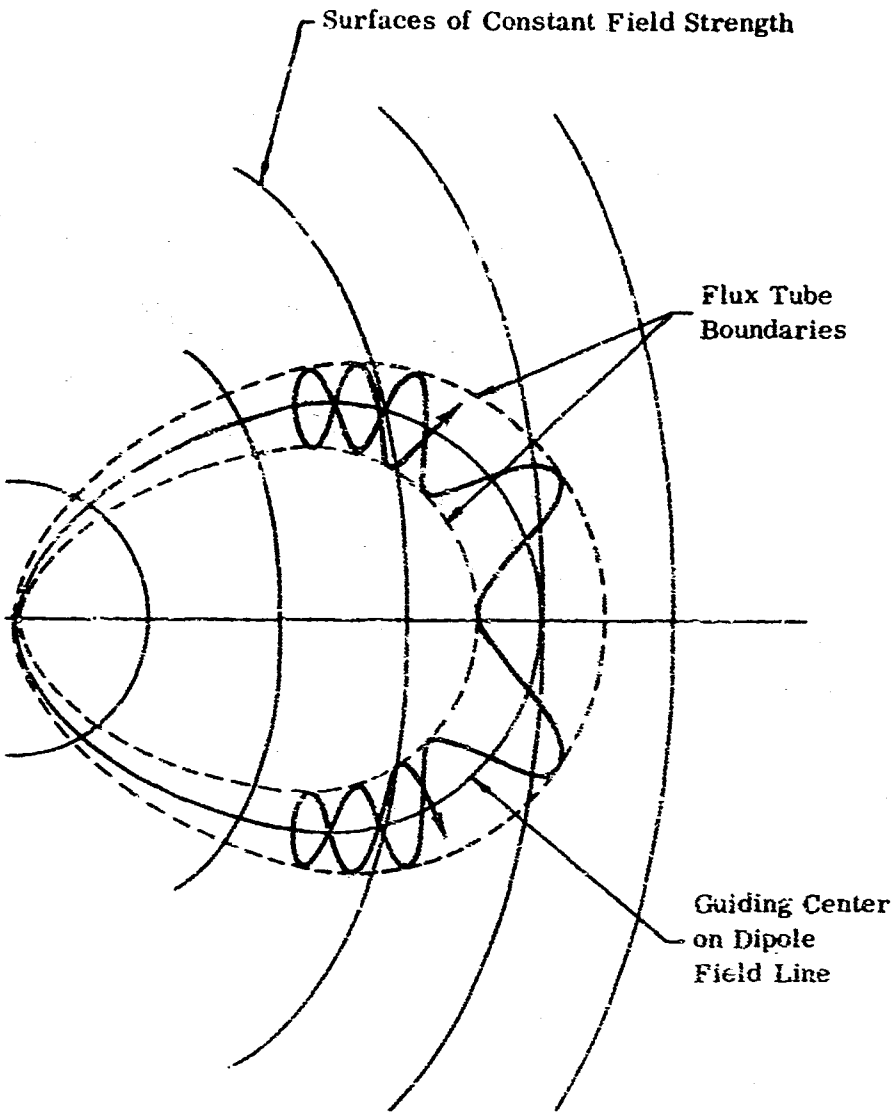

FIGURE 2-12 MERIDIAN PLANE PROJECTION OF THE MOTION OF A CHARGED PARTICLE TRAPPED IN A FLUX TUBE

Next, consider a particle in space traveling as shown in Figure 2-13. Because of the magnetic field the particle will be subjected to a transverse force.

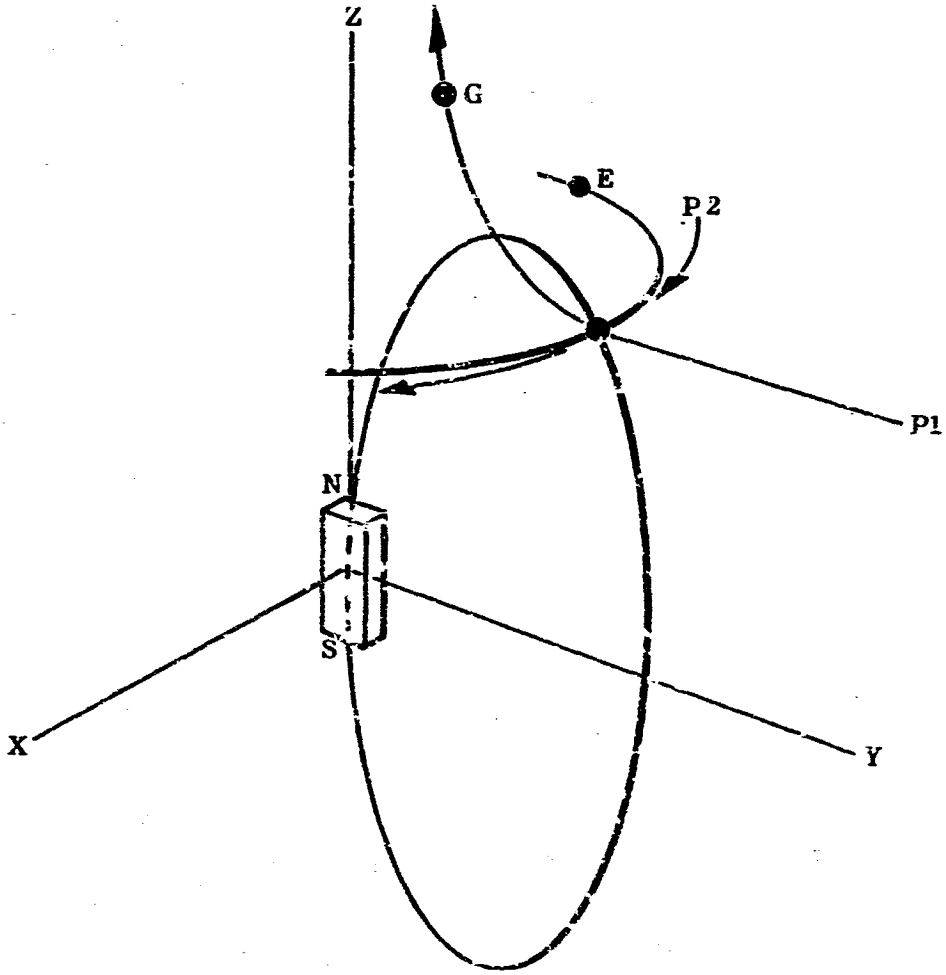

FIGURE 2-13 CHARGED PARTICLE MOTION IN A DIPOLE FIELD

For a particle coming from outer space in the direction P1 in Figure 2-13 the transverse force will be such as to bend the particle in path G and send the particle back out of the terrestial

system. If the particle is already trapped in the earth's magnetic system, such as P2, the magnetic field may force the particle to keep circling the earth as in path E. Thus the motion is confined to a certain volume surrounding the earth as shown in Figure 2-12. The density of particles with respect to position about the earth is beyond the scope of this document but attention is called to two references (A1, L1) which describe such details.

2.4 SOLAR FLARE PHYSICS

The exact cause of solar flares is not known, but there is a good deal that can be said about them and certain conclusions that can be inferred. The outer surface of the sun is a fluid, and its surface suffers from unequal rotation when the sun rotates. It is natural to assume that different surface layers rotate differently, but it may be difficult to rationalize that different zones rotate differently. Nevertheless, the equatorial zones rotate with a period of about 25 days while polar zones rotate with a period of about 34 days.

The sun, like the earth, possesses a magnetic dipole, but because the sun's surface fluids are highly ionized, there are additional magnetic effects not noticeable on earth. It would be beyond the scope of this report to give the details of these effects, but a qualitative description is quite apropos.

Although the cause of solar flares is not firmly established, the work of Babcock(B1) gives a plausible model. One of the assumptions of this model concerns the particular geometry of the solar dipole field. Normally it would be taken for granted that the lines of force would be buried deep within the sun curving monotonically toward and then away from the dipole axis as shown in Figure 2-14. The model used by Babcock assumes that the lines bend toward the surface and thus lie in surface layers, called isotachical layers. This is shown in Figure 2-14. It is these surface lines that will be involved in the following.

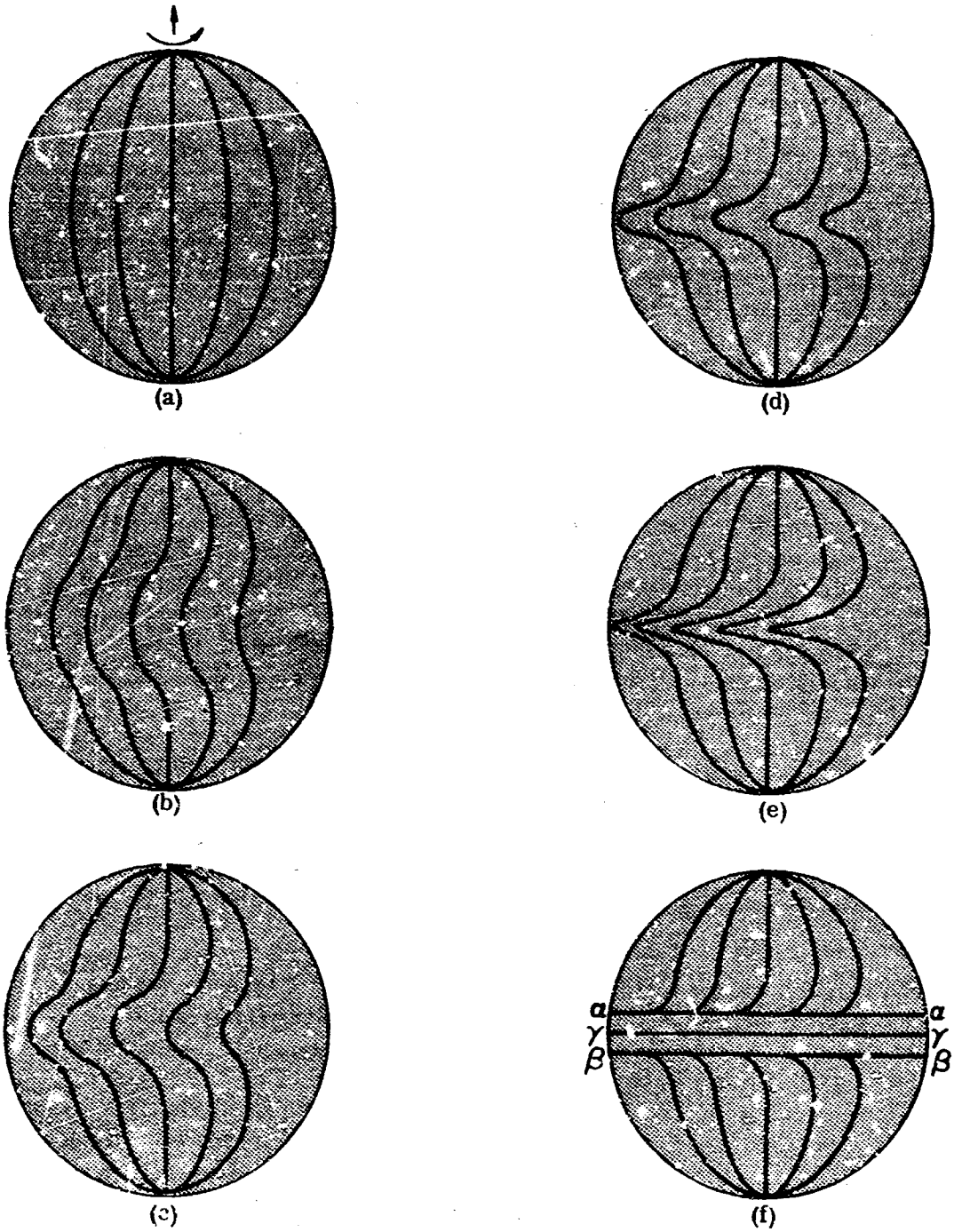

FIGURE 2-14 TEMPORAL DISTORTION OF THE SUB-SURFACE SOLAR MAGNETIC FIELD LINES

The vertical profile of the magnetic field at the equator, according to the Babcock model, is shown in Figure 2-15. In Figure 2-15(a), the lines are shown when no shear exists. In Figure 2-15(b), vertical shear in combination with the equatorial azimuthal effects described above cause a field increasing in depth.

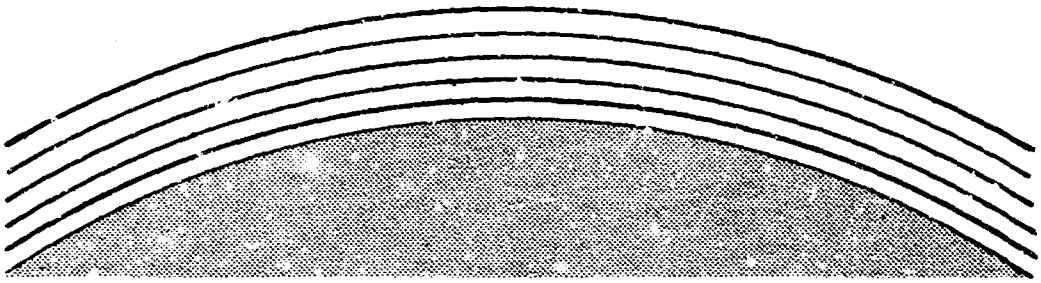

(a) Early in Flare Cycle

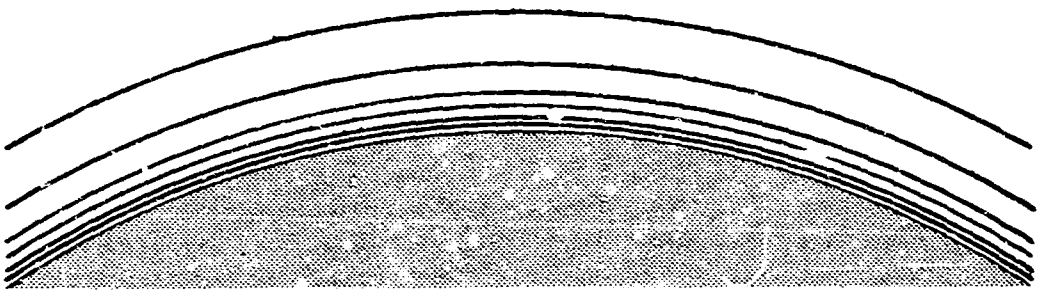

(b) Late in Flare Cycle

FIGURE 2-15 VERTICAL DISTRIBUTION OF SOLAR FIELD LINES

The field lines in the vicinity of the central meridian, i.e., along the line (γ, γ) in Figure 2-14(f), tend to be longitudinal and not comparatively dense. In certain zones off the central meridian where the field is mainly azimuthal, i.e., in the vicinity of the line (α, α) or (β, β), the lines are at maximum density relative to the rest of the solar field. The difference in field strengths of these zones causes tremendous vertical and horizontal magnetic stresses.

Since charged particles possess a magnetic field there is a tendency to reduce the strength of the field into which they move. In Figure 2-16, the particles are located along line (H, H) and the field is parallel. In Figure 2-16, some of the particles have moved to line (J, J) reducing that field, and consequently the lines have become bulged.

As the stress of the magnetic field beneath the surface becomes larger, the charged particles start a migration to the surface forcing the lines outward as in Figure 2-17. The results are shown as they would appear on the surface of the sun. This process continues until there is a considerable bulge as shown in Figure 2-17. This bulge has acquired the name "bottle".

As this bottle grows in size there is a tendency for particles to pour through the orifice "A" in Figure 2-18. At the same time, the lines resist being bulged. Thus, they become bubble shaped on the solar surface. At this point a final effect begins to take place. The solar Coriolis force comes into play and the bottle begins to twist as shown in Figure 2-19. This twisting effect may pinch off the bottle and free it from the solar surface.

The bottle is quite similar to a field caused by a dipole; this is shown in Figure 2-20. If the lines at P were directed toward A they would close as though a dipole were located at D. If particles of the proper energy were enclosed in the bottle, a situation similar to terrestrial trapped radiation would result. These particles would then spiral along a flux tube as shown in Figure 2-21.

Since the bottle is caused by particles traveling outward in space, it is not fixed in size but grows with time. Furthermore, depending upon the influx of particles, the bottle may grow with or without weakening.

It can be shown analytically that the energy of the particles trapped in a given flux tube is confined in energy spread. If the particles are too energetic, the field will not be strong enough to contain them and they will escape. On the other hand, if the particles are not energetic enough, they will be confined to one of the central tubes.

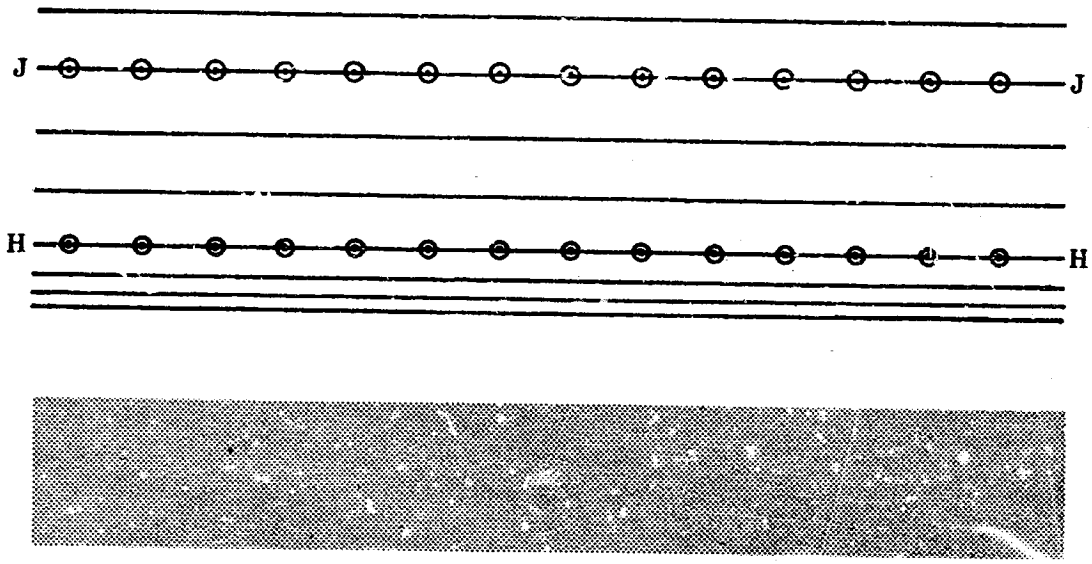

FIGURE 2-16 UNDISTORTED SOLAR MAGNETIC FIELD

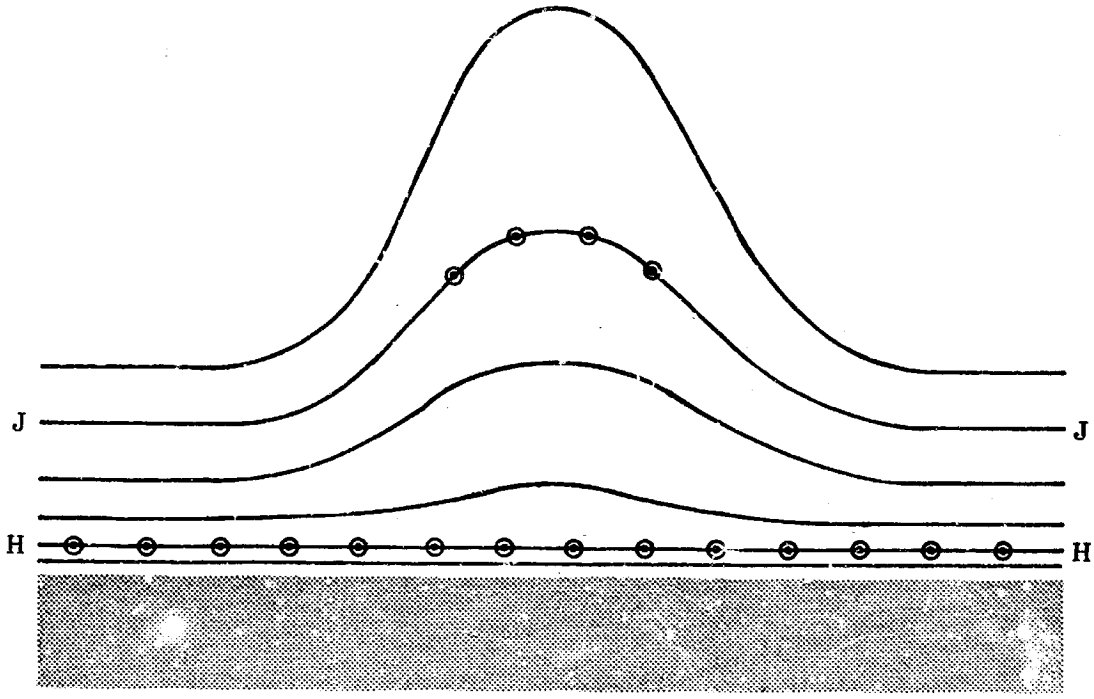

FIGURE 2-17 VERTICAL DISTORTION OF SOLAR MAGNETIC FIELD PRIOR TO FLARE

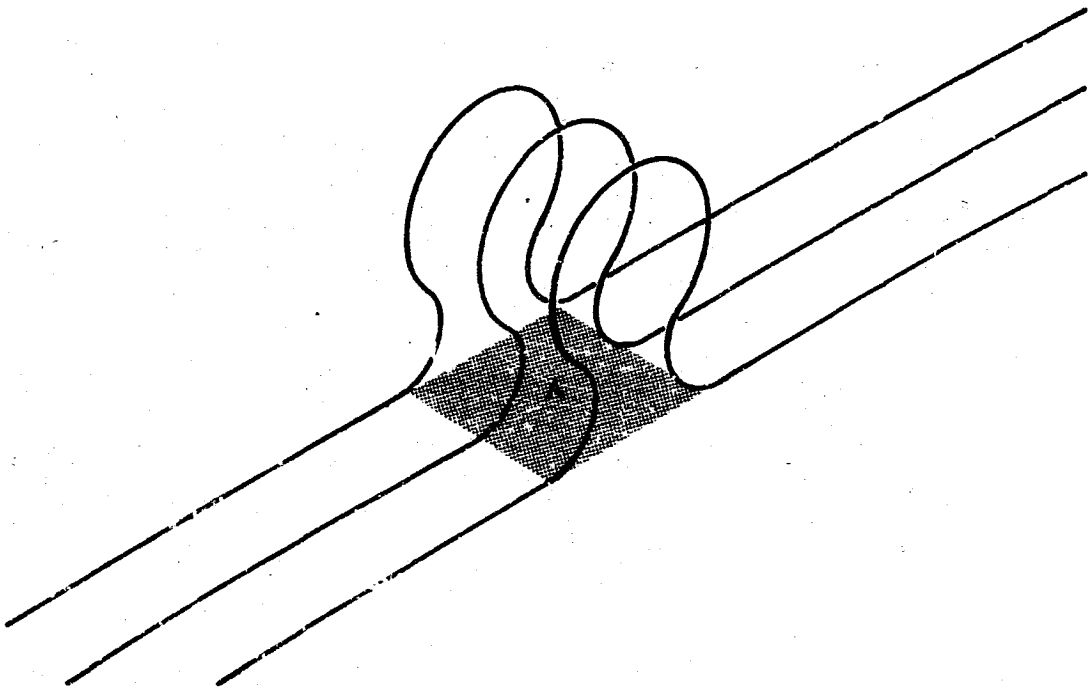

FIGURE 2-18 SOLAR MAGNETIC LINES ASSOCIATED WITH A FLARE

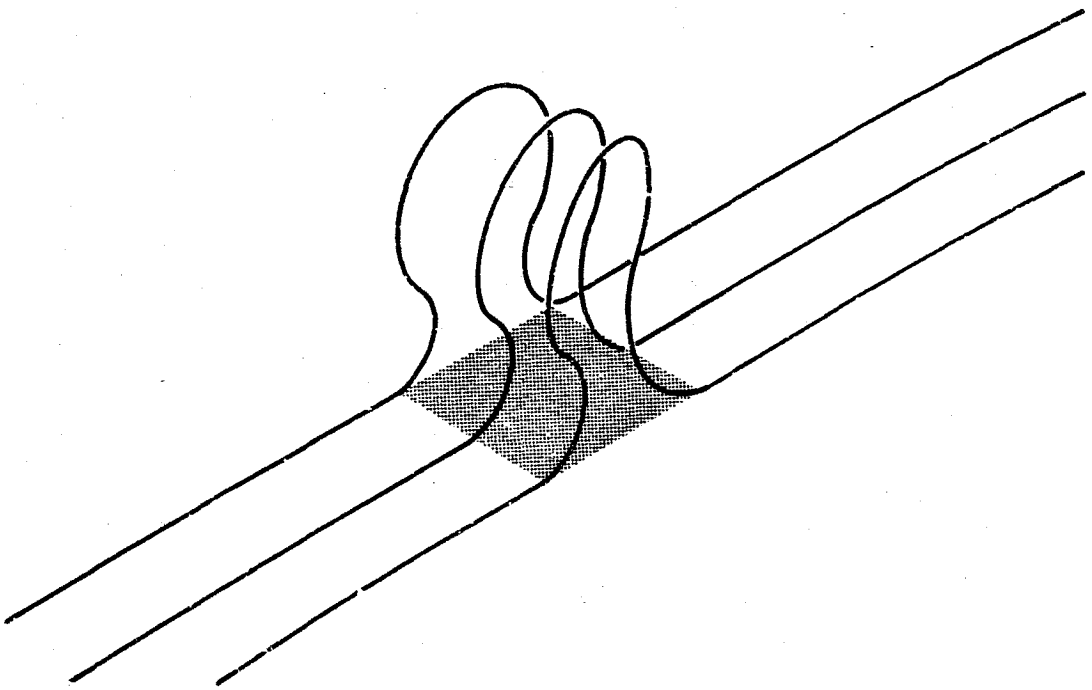

FIGURE 2-19 CORIOLUS EFFECT ON SOLAR MAGNETIC LINES ASSOCIATED WITH A FLARE

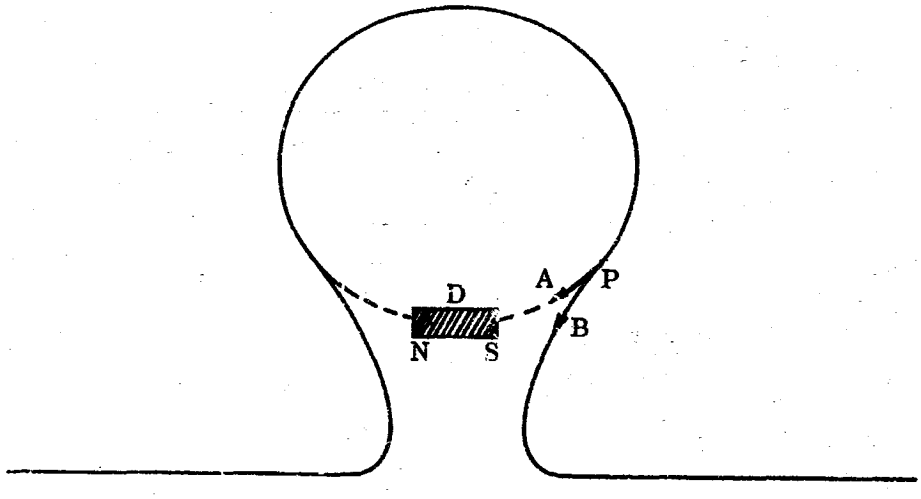

FIGURE 2-20 SOLAR MAGNETIC BOTTLE

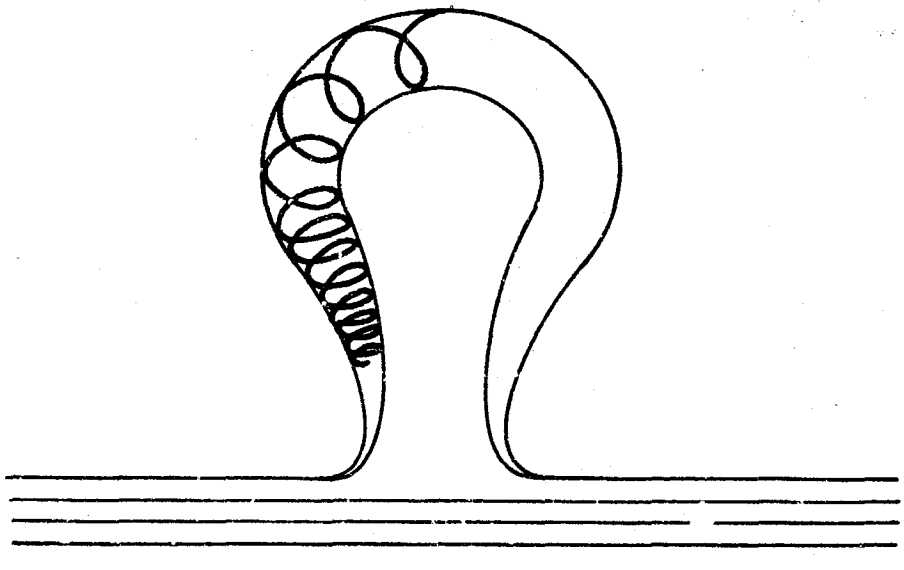

FICURE 2-21 CHARGED PARTICLE MOTION IN SOLAR MAGNETIC BOTTLE

If the particles pouring through the bottle orifice are slightly more energetic than necessary to be contained in the bottle, and if they are copious enough, they will carry the bottle along with them. The bottle in this case will actually grow while maintaining its strength. If the supply of particles is not replenished, however, and if there is an outward diffusion of them, then the bottle will grow; but will become weaker, and will finally be dissipated in space. At this time, the orifice will close and the solar surface will return to normal.

One of the unanswered questions concerns the rate at which particles pour through the orifice. Additionally, the change in spectrum shape, as a function of time, of the particles pouring through the orifice is not known.

Since optical observation is usually the first indication of a solar flare on the sun's surface and the size of the flare can be measured by this technique, this method is the predominant means of classifying a solar flare. An accepted unit of measurement is the "class". The various classes, as fractions of the solar disk, are given in Table 2-1. In determining the size by area measurement of the photograph, care must be taken to correct for the foreshortening. Figure 2-22 gives the correction for this. The actual peculiarities of the optical properties of a flare are quite complex and the existence of other characteristics does not presuppose the existence of an optical characteristic.

The optical characteristics include not only the size of the flare, but its brightness, which is usually indicated by a + or - sign. A large bright flare being, say, a 3+. There are measurements of temperature and shape of the flare, location with respect to the solar equator, and occasionally, magnetic measurements made at the time of the optical observation. Normally the temperature of the corona over the region of a flare is of the order of 2×10^6 ^oK, but during the flare this may increase to 4×10^6 ^oK(P1). The speed of the expanding coronal wave is closely linked with this temperature and is, in itself, a significant characteristic. This coronal wave is much slower moving than other burst irradiations and is the cause of the solar wind geomagnetic storm.

TABLE 2-1

IMPORTANCE VALUES RECOMMENDED BY IAU

Area in Square Degrees	Area in Millionths of Solar Hemisphere	Area in Millionths of Solar Disk	Importance
2.06 - 5.15	100 - 250	200 - 500	1
5.15 - 12.40	250 - 600	500 - 1200	2
12.40 - 24.70	600 - 1200	1200 - 2400	3

Area in Square Degrees = (0.020626) · Area in Millionths of Solar Hemisphere

= (0.010313) · Area in Millionths of Solar Disk

(Method used by Climax, Hawaii, Lockheed and Sacramento peak as of October 1, 1960)

$$\text{Corrected Area} = \frac{\text{Measured Area}}{\sqrt{1 - r^2} + 0.2r} = \frac{\text{Measured Area}}{\cos\theta + 0.2\sin\theta}$$

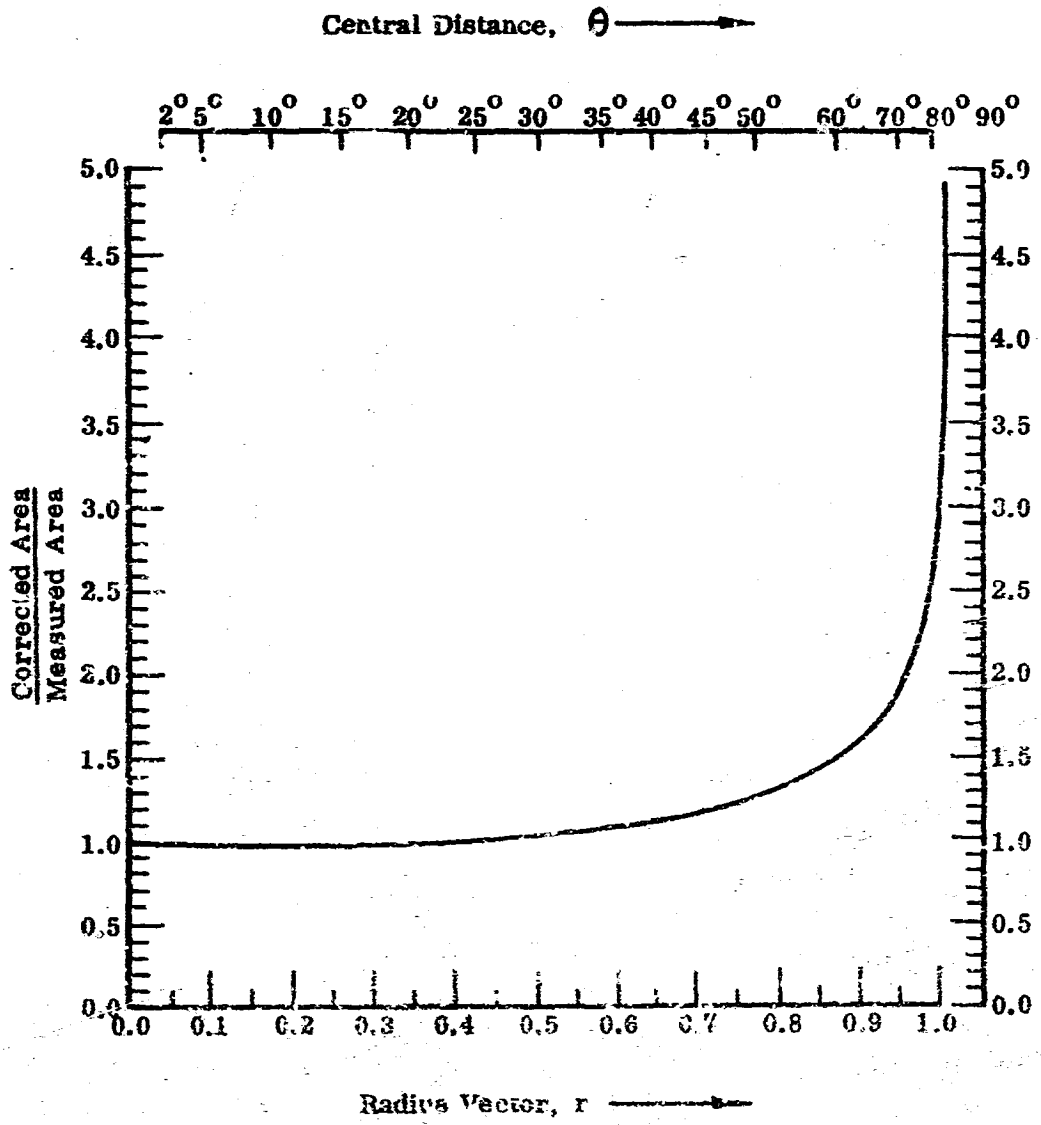

FIGURE 2-22 FLARE AREA AND IMPORTANCE

2.5 FLARES OF PARTICULAR INTEREST

A few of the more important flares are separately considered and will be discussed. In Figure 2-23 the differential energy spectra, normalized to 1 h. a. o. *, is given for six flares. The normalization to 1 h. a. o. is obtained by multiplying the spectra at T h. a. o. by T^2; thus, $f(E, t = 1) = T^2 f(E, t = T)$. In the following figures, spectra for other times after onset are given.

The primary purpose of the accompanying brief descriptions is to familiarize those new to the field with the literature and more common spectral characteristics. Accompanying each flare description there is a bibliography for that flare. Some references are repeated from flare to flare but this is necessary in order that each flare description be self-contained.

Table 2-2 gives information on each of the flares that should be useful to the user. They are given in a composite table for comparison purposes.

---

* hour after onset

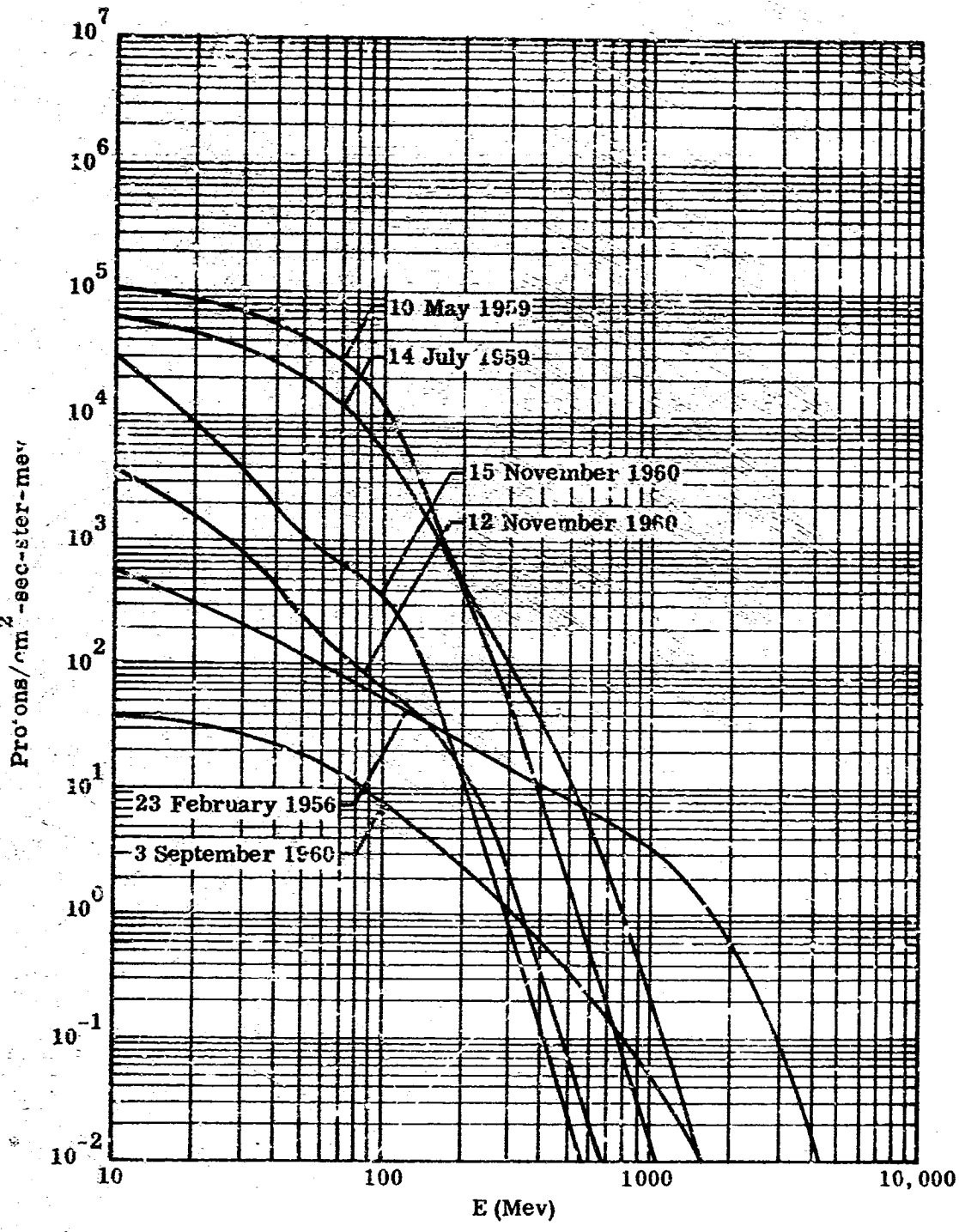

FIGURE 2-23 SOLAR PROTON DIFFERENTIAL ENERGY SPECTRA, NORMALIZED TO 1 HAO (BY t^{-2})

TABLE 2-2

FLARE DATA

Date	Optical Onset	Solar Position	Optical Duration	Geomagnetic Storm Duration	Solar Area	Importance
23 February 1956	0338 U. T. *	25°N 85°W	10 h 45 m		66.17 deg^2	3+
10 May 1959	2000 U. T.	19°N 50°E	3 h	24 h	25 deg^2	3+
14 July 1959	0342 U. T.	16°N 07°E	3 h	28 h	25 deg^2	3+
3 September 1960	0037 U. T.	20°N 88°E	1 h 20 m	26 h		3
12 November 1960	1316 U. T.	27°N 02°W	6 h	21 h	25 deg^2	3+
15 November 1960	0207 U. T.	26°N 33°W	2 h 20 m		15.16 deg^2	3+

* U. T. is universal time and is identical to Greenwich mean time.

23 February 1956

The most famous flare from the standpoint of having a large high energy particle flux is that of 23 February 1956 (Figure 2-24, Table 2-3). This flare contained more high energy particles than any other tabulated flare. The low energy section was not as copious as some later flares, and the exact reason for this is not known at this time. The dose inside the shield calculated for this flare showed that for thin shields (< 20 gms/cm^2) this flare was not as significant as some others. However, for exceedingly thick shields (> 200 gms/cm^2) this flare would generate many secondaries and the dose ratio would rise considerably in comparison to other flares at this shield thickness.

Historically this flare is unique in that it is the first flare for which a large amount of data was compiled. The most interesting article written on this flare is that of Meter, Parket, and Simpson (Reference 5). At the time this article was written, there had been no satellites in orbit and information was obtained from balloon flights and ground measurements only. Not only are the data presented in useful form, but these data formed the basis for the first flare model suitable for space shielding investigations.

The article considers the following:

1. Proton spectrum.
2. Neutron spectrum (resulting from proton bombardment of the earth's atmosphere).
3. Time decay of the flare.
4. Solar flare model.
5. The solar magnetic field holding the protons in a slowly expanding solar magnetic bottle.

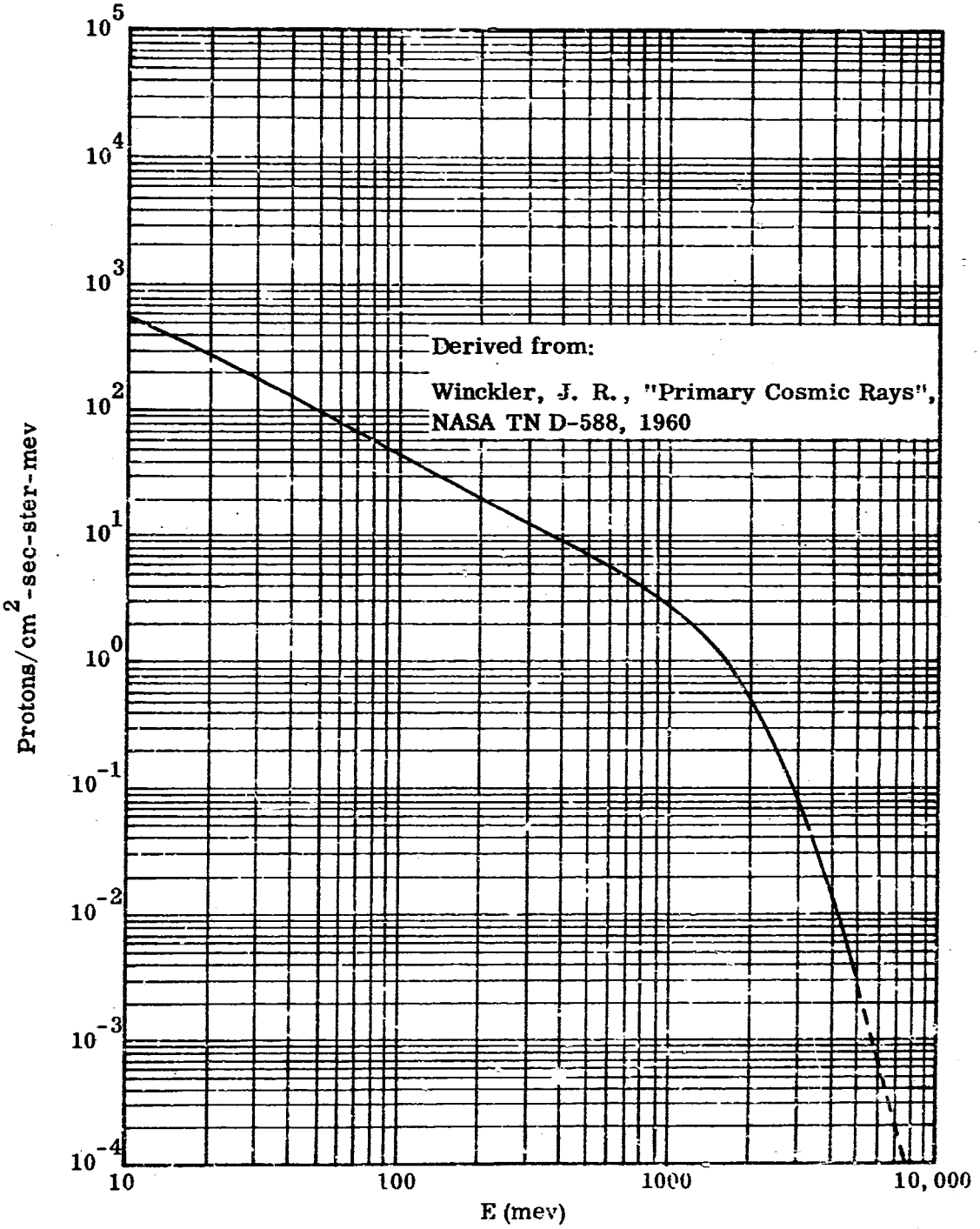

FIGURE 2-24 SOLAR PROTON DIFFERENTIAL ENERGY SPECTRUM, 23 FEBRUARY 1956, 1 HAO

TABLE 2-3

SOLAR FLARE, 23 FEBRUARY 1956

	Author	Title	Reference
1.	Anderson, K. A.	Solar Particles & Cosmic Rays	Sci. Am. 202 (6), 64-71, June 1960
2.	Gold, T.	Plasma & Magnetic Fields in the Solar System	J. Geophy. Res, 64 (11), 1665-1674, November 1959
3.	Obayashi, T. Hakura, Y.	Solar Corpuscular Radiation & Polar Ionospheric Disturbances	J. Geophy. Res. 65 (10), 3131-3142, October 1960
4.	Lockwood, J. A. Shea, M. A.	Variations of the Cosmic Radiation in November 1960	J. Geophy. Res. 66 (10), 3083-3093, October 1961
5.	Meyer, P. Parker, E. N. Simpson, J. A.	Solar Cosmic Rays of February 23, 1956 and Their Propagation Through Interplanetary Space	Phys. Rev. 104 (3), 768-783, November 1, 1956
6.	Van Allen, J. A. Winckler, J. R.	Spectrum of Low-Rigidity Cosmic Rays During the Solar Flare of February 23, 1956	Phys. Rev. 106 (5), 1072-1073, June 1, 1957
7.	Bailey, D. K.	Abnormal Ionization in the Lower Ionosphere Associated with Cosmic Ray Flux Enhancements	Proc. of the IRE 47, 255-261, February 1959
8.	Knecht, R. W. Davies, K.	Solar Flare Effects in the F Region of the Ionosphere	Nature, Vol. 190, 797-798, May 27, 1961
9.	Peterson, L. E. Winckler, J. R.	Gamma Ray Burst from a Solar Flare	J. Geophy. Res. 64 (7), 697-707, July 1959

Solar Flare of 10 May 1959

This was one of the largest flares ever reported. It began with extreme intensity bursts of solar radio noise. Solar particles were observed at the earth within 5 hours of the optical beginning and exhibited their maximum effect approximately 12 hours after onset.

This flare for the first time provided good exposures to nuclear emulsions carried aloft by five balloons released 30 hours after onset. The measured particles were almost entirely protons. A flux of 10^3 protons/cm^2-sec above 110 Mev and an integral spectrum of $N(E)dE = KE^{-4.8}\,dE$ between 110-220 Mev was observed.

Based on different time exposures the decay of proton intensity may be construed to follow a t^{-2} decay rate. Figure 2-25 is a plot of the solar proton differential energy spectrum for this event for data measured 33 hours after onset. This spectrum is normalized to 1 hour after onset by multiplying the original data by $(33)^2$, and the result is presented in Figure 2-23. This spectrum exhibits a large differential energy flux in the range from 10-20 Mev, but there is a rapid decrease at higher energies, following an E^{-7} distribution for energies above 300 Mev. See Table 2-4 for references.

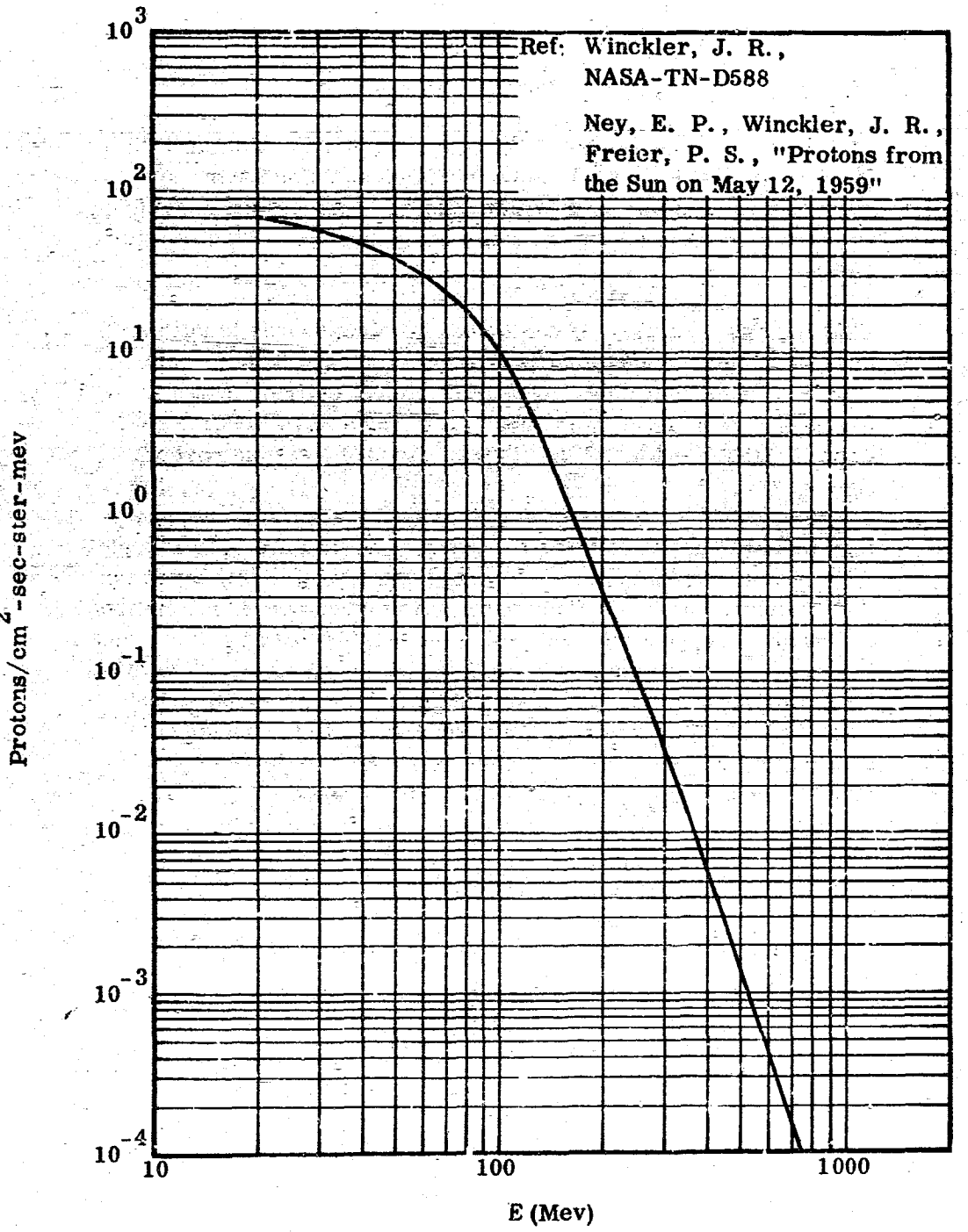

FIGURE 2-25 SOLAR PROTON DIFFERENTIAL ENERGY SPECTRUM, 10 MAY 1959, 33.0 HAO

TABLE 2-4

SOLAR FLARE, 10 MAY 1959

Author	Title	Reference
1. Barnes, T. G. Finkelman, E. M. Barazotti, A. L.	Radiation Shielding of Lunar Space Craft	Astronautical Sci. Rev., 11-18 January, March 1961
2. Winckler, J. R.	Non-Relativistic Proton from Solar Flares	AAAS Meeting, Chicago, Illinois, 28 December 1959
3. Ney, E. P. Winckler. J. R.	Protons from the Sun on May 12, 1959	Phys. Rev. Letters 3 (4), 183-185, August 15, 1959
4. Biswas, S.	Forbush Decrease of the Flux of Heavy Primary Nuclei of Cosmic Rays on May 12 & July 12, 1959	J. Geophy. Res. 66 (9), 2653-2647, September 1961

The Flare Group of July 1959

The great flare that occurred on 14 July 1959 (Figure 2-26, Table 2-5) was one of three that occurred on 10, 14, and 16 July 1959. All of the flares were of importance 3+[5]. This creates an extremely hazardous situation to space flight, as the possibility of two such flares so close together had been considered remote. This situation was to repeat itself in November 1960.

The second flare of these three was the most severe and is the flare most widely reported. The 16 July 1959 flare was variously reported as 3 and 3+; Brown and D'Arcy[5], Ehmert[6], and Obayashi and Hakura[8] consider it as a 3+ flare; but Warwick and Hourwitz[9] consider it only as a 3 flare.

A comprehensive article on this group of flares is that of Winkler, Blavson, and Peterson[7]. While no spectra are given as plots, general descriptions and the exponential fall of the spectra are well depicted.

Despite the reports that the 16 July 1959 flare was not as significant as the other two, the article by Winckler, et al, states that the rigidity spectrum extends to about 1 Bv. This article also gives a qualification on the low energy content in stating that the low energy group content was not greater than observed in other events of the July series.

The 14 July flare was the greatest of the three and there is an implication that the flare contained two maxima[7]. One occurred at 0349 U. T. and the other at 0527 U. T. The nature of this flare was such that it had a copious content of low energy particles. Furthermore, the high energy content was exceeded only by the 23 February 1956 flare.

A description of the magnetic storm and other details can be found in the Winkler article[7].

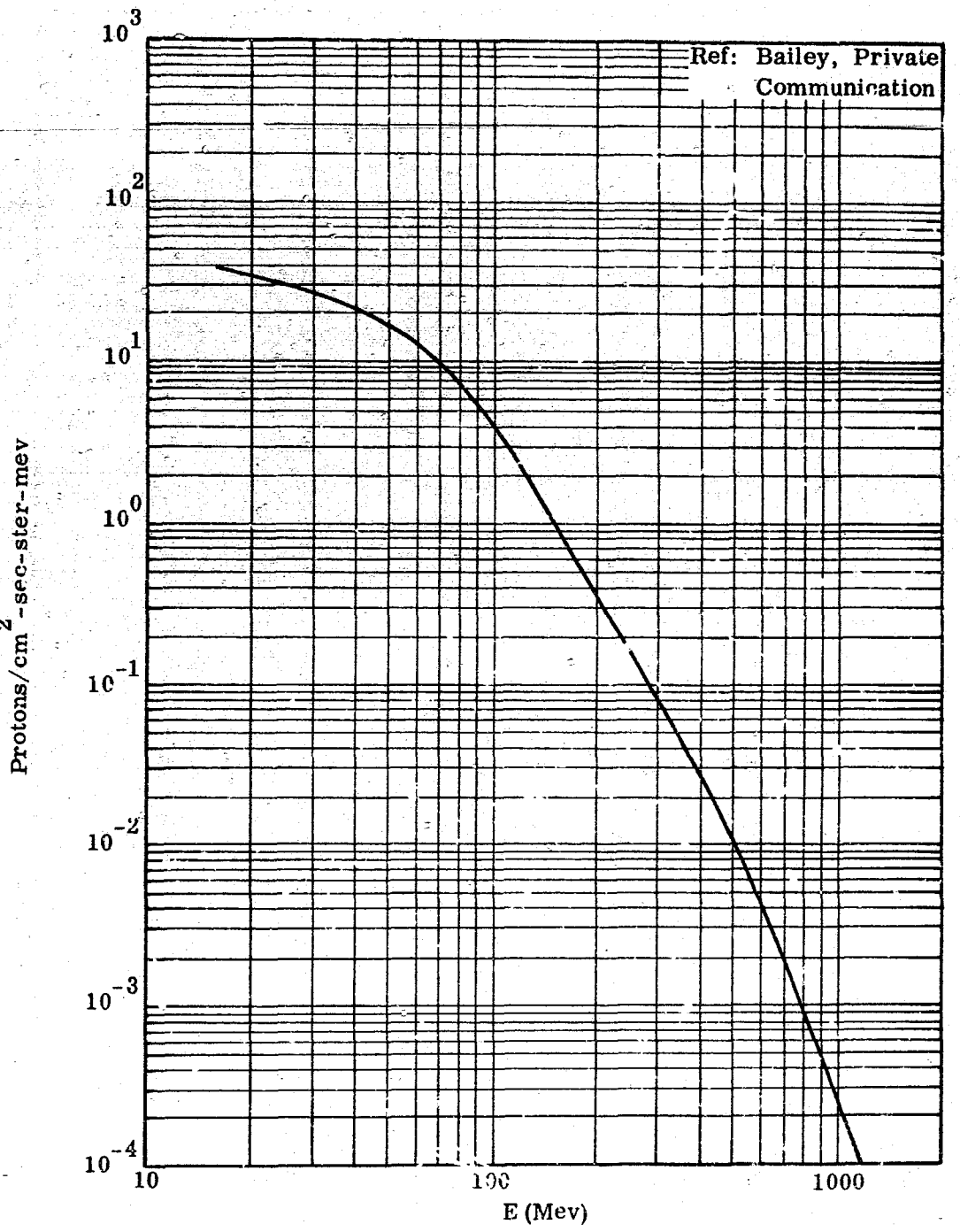

FIGURE 2-26 SOLAR PROTON DIFFERENTIAL ENERGY SPECTRUM, 14 JULY 1959, 31.5 HAO

TABLE 2-5

SOLAR FLARE, 14 JULY 1959

Author	Title	Reference
1. Barnes, T. C. Finkelman, E. M. Barazotti, A. L.	Radiation Shielding of Lunar Spacecraft	Astronautical Sci. Rev. 11-18, Jan. March 1961
2. Earl, J. A.	Balloon Measurement of Solar Cosmic Rays at Fort Churchill, Canada, During July 1959	J. Geophys. Res. 66 (10), 3095-3102, October 1961
3. Reid, G. C.	A Study of the Enhanced Ionization Produced by Solar Protons During a Polar Cap Absorption Event	J. Geophys. Res. 66 (12), 4071-4085, December 1961
4. Armstrong, A. H. Harrison, F. B. Heckman, H. H. Rosen, L.	Charged Particles in the Inner Van Allen Radiation Belt	J. Geophys. Res. 66 (2), 351-357, February 1961
5. Brown, R. R. D'Arcy, R. G.	Observations of Solar Flare Radiation at High Latitude during the Period July 10-17, 1959	Phys. Rev. Letters 3 (8), 390-392, 15 October 1959
6. Ehmert, A. Erbe, H. Pfotzer, G. Anger, C. D. Brown, R. R.	Observations of Solar Flare Radiation & Modulation Effects at Balloon Altitudes July 1959	J. Geophys. Res. 65 (9), 2685-2694, September 1960

TABLE 2-5 (Continued)

Author	Title	Reference
7. Winckler, J. R. Bhavsar, P. D. Peterson, L.	The Time Variation of Solar Cosmic Rays During July 1959 at Minneapolis	J. Geophys. Res. 66 (4), 995,
8. Obayashi, T. Hakura, Y.	Solar Corpuscular Radiation and Polar Ionospheric Disturbance	J. Geophys. Res. 65 (10), 3131, October 1960
9. Warwick, C. S. Haurwitz, M. W.	A Study of Solar Activity Associated with Polar-Cap Absorption	J. Geophys. Res. 67 (4) 1317, April 1962

3 September 1960

The flare that occurred 3 September 1960 (Figure 2-27, Table 2-6) was not in the same category as the other flares considered in this report. It was deemed important, however, to examine at least one well documented small flare. It is conceivable that the relatively large number of small flares that occur is enough to warrant their examination.

By 1960 is was apparent that better monitoring of solar flares was required and consequently a 24-hour-a-day standby for observation of solar conditions was instituted by NASA at Fort Churchill. As soon as various stations around the world notified Fort Churchill, sounding rockets were sent aloft for measurement of solar particle beams. As a result of this vigil two rockets were launched to observe this particular flare. The flare commenced at 0040 U. T. on 3 September 1960 and rockets NASA 1019 and 1020 were sent aloft at 1408 and 1730 U. T., respectively, the same date.

Many previous flares had been observed but not with the same insight as was possible in this case. The flare was preceded by flares of smaller importance, and the interplanetary spatial effects of these earlier flares upon the particles of this flare were quite evident. The earlier flares definitely caused electromagnetic distrubances in the earth's magnetic field which caused some noticeable effect on the less energetic particles of the 3 September 1960 flare. Yet the high energy particles of the 3 September 1960 flare easily spiraled through the solar clouds from the preceding flares. These observations, more than an evaluation of the spectra, were the important aspects of this particular flare.

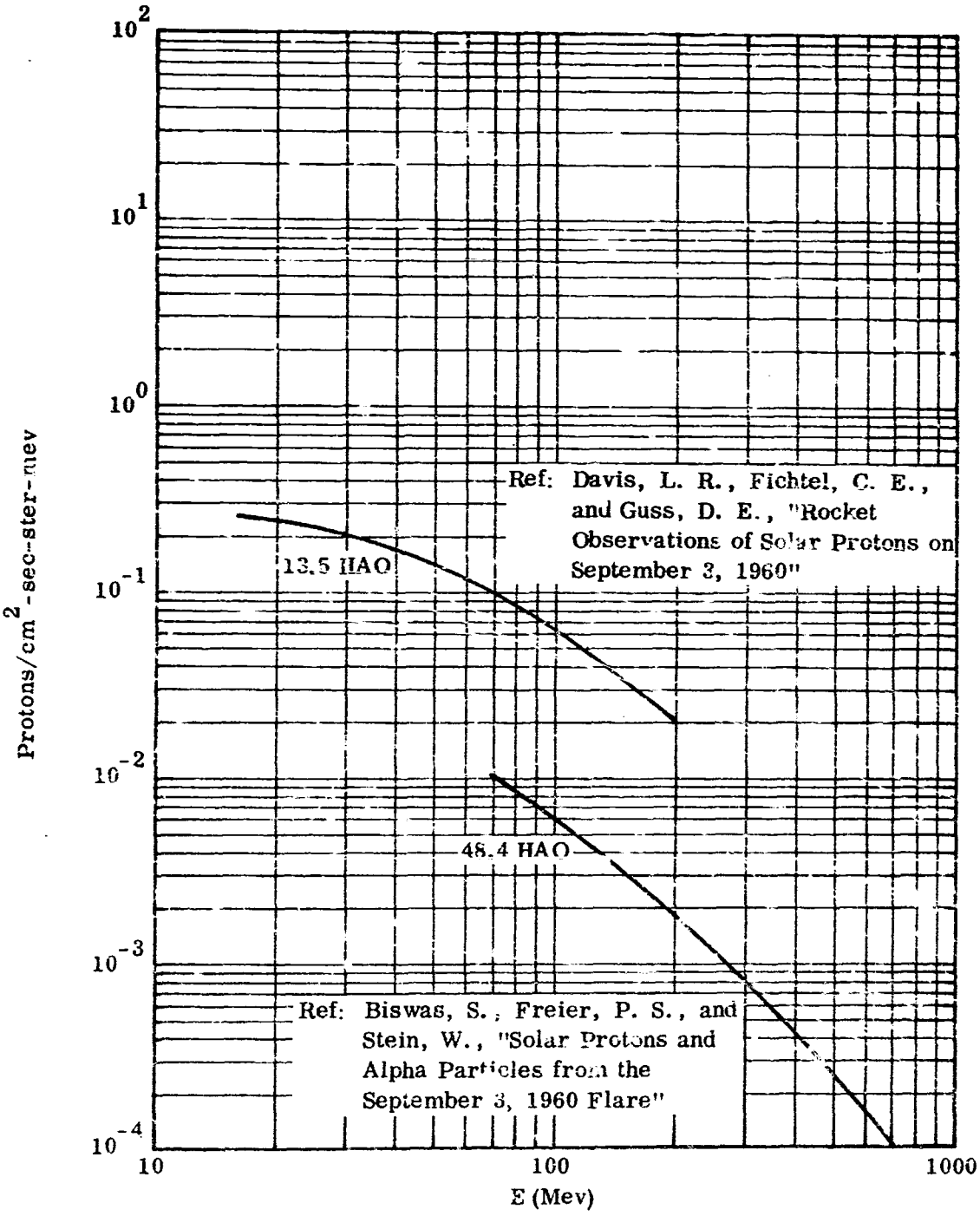

FIGURE 2-27 SOLAR PROTON DIFFERENTIAL ENERGY SPECTRUM, 3 SEPTEMBER 1960

TABLE 2-6

SOLAR FLARES, 3 SEPTEMBER 1960

Author	Title	Reference
1. Davis, L. R. Fichtel, C. E. Guss, D. E. Ogilvie, K. W.	Rocket Observations of Solar Protons on September 3, 1960	Phys. Rev. Letters 6 (9) 492-494, May 1, 1961
2. Lockwood, J. A. Shea, M. A.	Variations of the Cosmic Radiation in November 1960	J. Geophy. Res. 66 (10) 3083-3093, October 1961
3. Naugle, J. E. Kniffen, D. A.	Flux & Energy Spectrum of the Protons in the Inner Van Allen Belt	Phys. Rev. Letters 7 (1) 3-6, 1 July 1961
4. Biswas, S. Freier, P. S. Stein, W.	Solar Protons and X Particles from the September 3, 1960 Flare	J. Geophy. Res. 67 (1), 13-18, January 1962
5. Fichtel, C. E. Guss, D. E.	Heavy Nuclei in Solar Cosmic Rays	NASA, GSFC, 1961, Kyoto Conf. on Cosmic Rays
6. Mosley, A. J. Goedike, A. D.	Space Radiation - Its Nature and Properties	Aerospace Engineering, June 1962

November 1960 Flare Group

The flare group of November 1960 was more intense than the July 1959 1959 flare group, although the 14 July 1959 flare was greater than any one of the November 1960 flares. As with the 3 September 1960 flare, the Churchill group again sent aloft sounding rockets.

The two main flares, as in the case of the September 1960 flares, were affected by both the particles and the magnetic fields of the earlier flares[10]. The 12 November 1960 flare (Figure 2-28, Table 2-7) had an onset time of 1316 U.T. and a NASA sounding rocket was launched at 1840 U.T. This was Rocket NASA 1024 and contained emulsions that were recovered. There were three rockets sent aloft, NASA 1024, NASA 1015 (launched at 2332, 12 November 1960) and NASA 1016 (launched at 1603, 13 November 1960).

The details of the results of these rocket shots have been presented in a NASA report by Ogilvie, Bryant, and Davis[7] which details also the type of detector and the rocket trajectory specifications. The change of spectrum with time is very well tabulated and the radiation was observed with emulsions, Geiger counters and scintillation counters.

The 15 November flare (Figure 2-29, Table 2-8) had an onset time of 0207 U.T. Three balloon flights were made during this event. The first flight was made 9 hours after onset of the flare and before the disturbance of the earth's geomagnetic cutoffs. The second flight was made 19 1/2 hours after onset of the flare and showed the absence of geomagnetic cutoffs as particles with low energies were detected. The third flight was made 38 hours after onset of the flare and at this time the earth's geomagnetic cutoffs were in effect again as the solar proton intensity was only a few times higher than normal cosmic-ray background. McCracken[8] states that the protons exhibited anisotropy during the first 45 minutes of measurement by neutron riometers and by 90 minutes the protons had become isotropic.

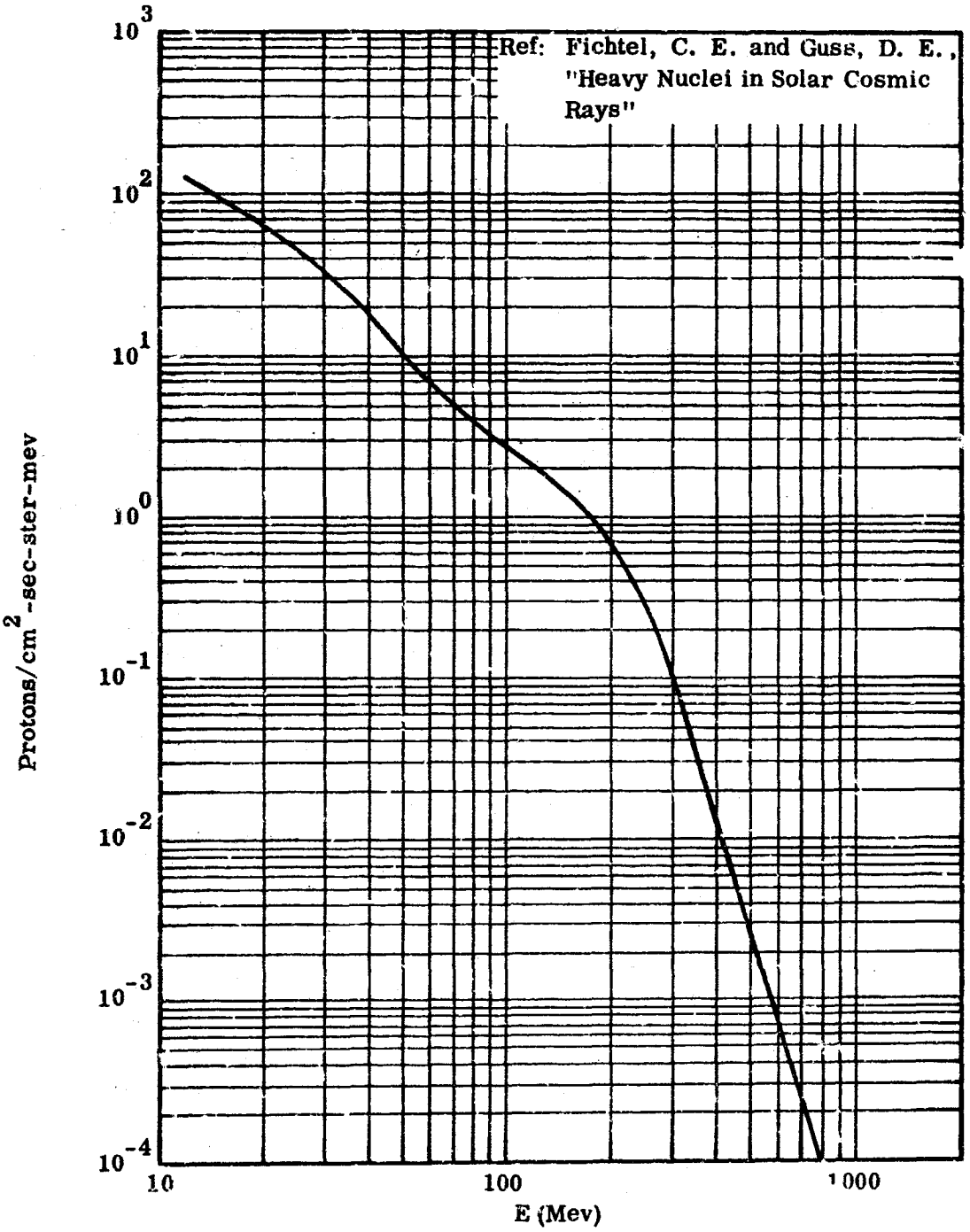

FIGURE 2-28 SOLAR PROTON DIFFERENTIAL ENERGY SPECTRUM, 12 NOVEMBER, 1960, 5.17 HAO

TABLE 2-7

SOLAR FLARE, 12 NOVEMBER 1960

Author	Title	Reference
1. Dodson, H. W.	McMath-Hulbert Observatory Observations of the Cosmic Flare of 12 November 1960	McMath-Hulbert Obs. Report, University of Michigan
2. Gregory, J. B.	Antarctic Observations of the Solar Proton Event November 11-23, 1960	State University of Iowa Report
3. Lockwood, J. A.	Variations of the Cosmic Radiation in November 1960	J. Geophy. Res. 66 (10), 3083-3093, October 1961
4. NERA Staff	The Cosmic Ray Flare on November 12, 1960, and Solar Activity during the Period November 10-15, 1960	Nature, Vol. 189, 438-440, 11 February 1961
5. Obayashi, T.	List of Major Events, Nov. 6-21, 1960	
6. Knecht, R. W. Davies, K.	Solar Flare Effects in the F Region of the Ionosphere	Nature, Vol. 190, 797-798, 27 May 1961
7. Ogilvie, K. W. Bryant, D. A. Davis, L. R.	Rocket Observations of Solar Protons during the November 12, 1960 Event	NASA, GSFC, contributions to 1961 Kyoto Conf. on Cosmic Rays & Earth Storms. J. Geophy. Res. 67 (3), March 1962
8. McCracken, K. G.	The Cosmic Ray Flare Effect - The Flare Effects of May 4, November 12 & 15, 1960	J. Geophy. Res. 67 (2), 435-446, February 1962

TABLE 2-7 (Continued)

Author	Title	Reference
9. Fichtel, C. E. Guss, D. E.	Heavy Nuclei in Solar Cosmic Rays	NASA, GSFC, 1961 Kyoto Conference
10. Ney, E. P. Stein, W. A.	Solar Protons, Alpha Particles, and Heavy Nuclei in November 1960	J. Geophys. Res. 67 (6), 2087-2105, June 1962

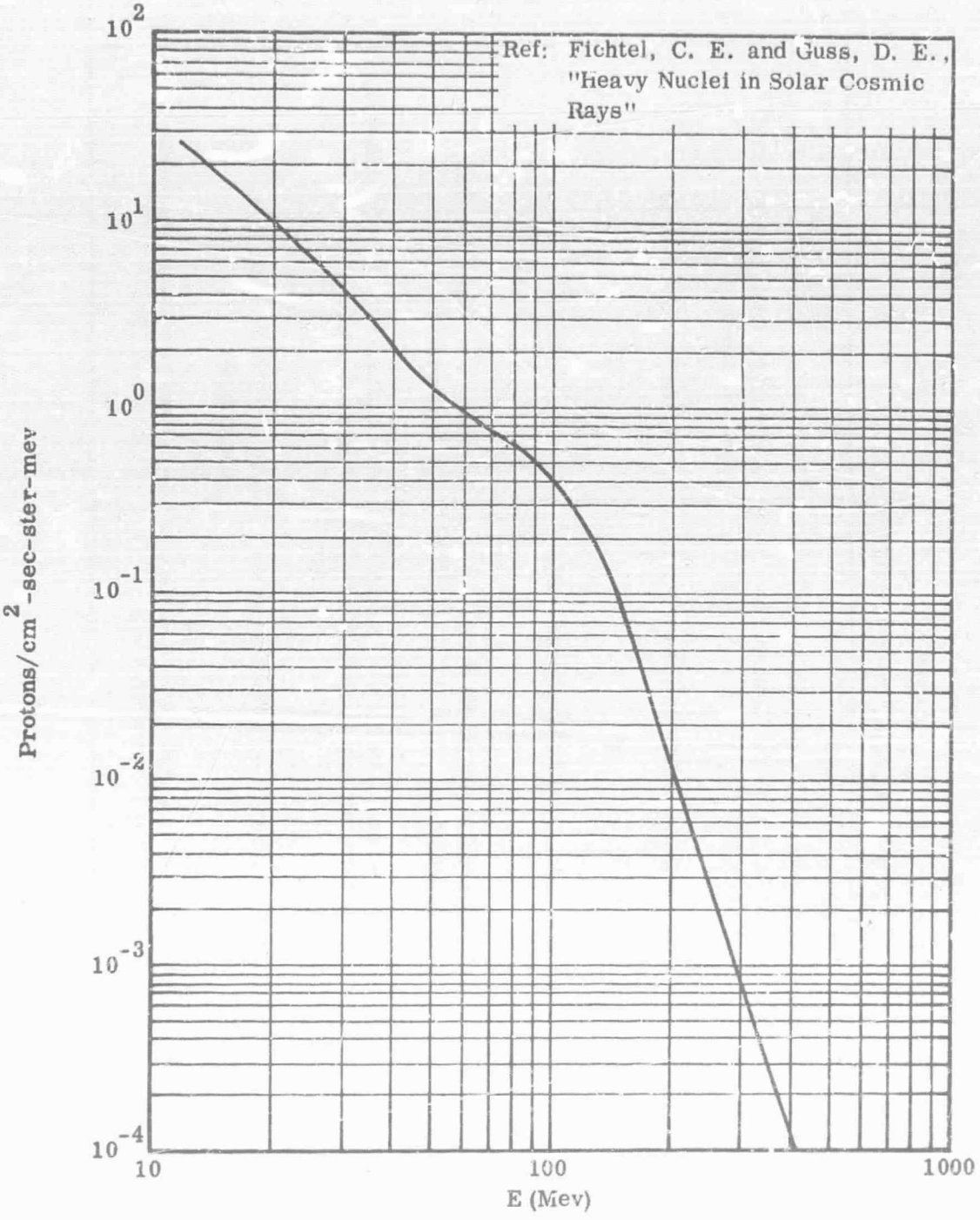

FIGURE 2-29 SOLAR PROTON DIFFERENTIAL ENERGY SPECTRUM, 15 NOVEMBER 1960, 41.3 HAO

TABLE 2-8

SOLAR FLARE, 15 NOVEMBER 1960

Author	Title	References
1. Lockwood, J. A. Shea, M. A.	Variations of Cosmic Radiation in November 1960	J. Geophy. Res. 66 (10), 3083-3093, October 1961
2. Nagasawa, S. Takakuro, T. Tauchiya, A.	A Very Unusual Flare on November 15, 1960	Publ. Astro. Soc. Japan
3. Obayashi, T.	List of Major Events, November 6-21, 1960	
4. Knecht, R. W. Davies, K.	Solar Flare Effects in the F Region of the Ionosphere	Nature, Vol. 190, 797-798, 27 May 1961
5. McCracken, K. G.	The Cosmic Ray Flare Effect - The Flare Effects of May 4, November 12 & 15, 1960	J. Geophy. Res. 67 (2), 435-455, February 1962
6. Fichtel, C. E. Guss, D. E.	Heavy Nuclei in Solar Cosmic Rays	NASA, GSFC, 1961 Kyoto Conference
7. Ney, E. P. Stein, W. A.	Solar Protons, Alpha Particles, and Heavy Nuclei in November 1960	J. Geophy. Res. 67 (6), 2087-2105, June 1962

2.6 REFERENCES

A1 Apel, J. R.: Geomagnetic Field Perturbation Due to Trapped Particles, AFCRL-420, April 1961

B1 Babcock, H. W.: The Topology of the Sun's Magnetic Field and the 22-Year Cycle, Astrophysical Journal, Vol 133 (3), p. 572, May 1961

F1 Fermi, E.: Nuclear Physics, University of Chicago Press, p. 225, 1955

L1 Liemohm, H.: Radiation Belt Particle Orbits, D1-82-0116, June 1961

P1 Parker, E. N.: Sudden Expansion of the Corona Following a Large Solar Flare and the Attendant Magnetic Field and Cosmic Ray Effects, Astrophysical Journal, Vol 133 (3), p. 1014, May 1961

S1 Stratton, J. A.: Electromagnetic Theory, McGraw Hill, 1961

W1 Willis, B. H.; Stableford, C. V.: High-Energy Particle Data, Vol I, UCRL-2426 (Rev), November 1956

BLANK PAGE

3.0 NUCLEAR DATA COMPILATION

3.1 INTRODUCTION

Conventional shielding analyses have generally dealt with noncharged particles with energies below 14 Mev, and as a result, the shield investigator became versed in the physical phenomena pertinent to this energy range. The advent of the manned spacecraft program has stimulated interest in a field of high energy physics which has heretofore been primarily the province of the physicist. The accompanying data are intended to serve as an introduction to the types of phenomena pertinent to these new shielding problems. This is not intended to be a complete guide to all the work in a field which has been quite active for a period well in excess of a decade. Excellent topical reviews appear from time to time, and the literature search in this compilation has usually terminated with the most recent review of adequate scope without necessarily checking original sources. In other instances, data have been accumulated only to the point of demonstrating order-of-magnitude or trends of variation. If the best estimates of quantities are desired, the original sources should be consulted. It is hoped, however that the references contained in these articles will assist the researcher materially in this search for primary data.

A number of books and monographs are available in the field of high energy physics. They range in complexity from the two-volume "Mesons and Field" by Schweber, Bethe, and de Hoffmann[S3], * to a simple monograph such as "High Energy Physics" by Lock[L6]. The latter is recommended as an introduction both to experimental and theoretical techniques and to the results obtained.

3.2 ELEMENTARY PARTICLES

As the energy range of interest is increased, the number of elementary particles involved in particle collisions also increases.

---

* References are listed at end of section.

The accompanying table of elementary particles (Table 3-1) gives some of the known elementary particles, their rest masses in Mev derived from the relation $E = mc^2$, their mean lives, and a set of quantum numbers which characterize the particle further. The quantum numbers are defined as follows:

Spin: Spin is the intrinsic angular momentum of a particle measured in units of $\hbar = h/2\pi = 6.582 \times 10^{-16}$ ev-sec.

Isotopic Spin: (T, T_Z) Isotopic spin is a quantum number related to the charge of the particles. It also is given the name "isobaric spin" and "isospin" in the literature. Like angular momentum, it has integral of half-integral values for the total quantum number (T), and also for its components along an axis in a hypothetical space (T_Z). However, isotopic spin is not a true intrinsic angular momentum.

Parity: The parity of a system is determined by whether the wave function describing the system does or does not change sign upon an inversion of the space coordinates. It is + for no change and - for a change. The intrinsic parity of a particle is determined by the effect of its absorption upon the parity of a system containing the particle.

Strangeness (S): The "strangeness" is related to the charge center of a particle multiplet as explained below.

In addition to the quantum numbers, typical decay products are given.

TABLE 3-1

ELEMENTARY PARTICLES

Particle		Rest Mass (Mev)	Mean Life (sec)	Spin	Isotopic Spin	T_Z	(S)*	Some Decay Products	Baryon Number
Photon	γ	0	Stable	1			0		0
Leptons									
Neutrino	ν^0	$< 2 \cdot (-4)$	Stable	1/2			0		0
Antineutrino	ν^0	$< 2 \cdot (-4)$	Stable	1/2			0		0
Electron	e^-	.510976	Stable	1/2			0		0
Positron	e^+	.510976	Stable	1/2			0		0
Muon	μ^-	105.7	2.22(-6)	1/2			0	$e^- + \nu^0 + \overline{\nu}^0$	0
Antimuon	μ^+	105.7	2.22(-6)	1/2			0		0
Mesons									
Pions	π^+	139.63	2.56(-8)	0	1	+1	0	$\mu^+ + \nu^0$, $e^+ + \nu^0$	0
	π^-	139.63	2.56(-8)	0	1	-1	0	$\mu^- + \nu^0$	0
	π^0	135.04	2.(-16)	0	1	0	0	$\gamma + \gamma$	0
K Meson	K^+	494.0	1.224(-8)	0	1/2	+1/2	+1		0
	K^0	497.9	#	0	1/2	-1/2	+1	See Reference G2	0
Anti K Meson	K^-	494.0	1.224(-8)	0	1/2	-1/2	-1		0
	K^0	497.9	#	0	1/2	+1/2	-1		0
Baryons									
Proton	P^+	938.213	Stable	1/2	1/2	+1/2	0		+1
Antiproton	P^-	938.213	Stable	1/2	1/2	-1/2	0		-1
Neutron	N^0	939.506	1.011(3)	1/2	1/2	-1/2	0	$P^+ + e^- + \nu^0$	+1

TABLE 3-1 (Continued)

Particle		Rest Mass (Mev)	Mean Life (sec)	Spin	Isotopic Spin	T_Z	S*	Some Decay Products	Baryon Number
Baryons (cont'd)									
Antineutron	$\overline{N}^o$	939.506	1.011(3)	1/2	1/2	+1/2	0		-1
Lambda$^+$	Λ^o	1115.2	2.42(-10)	1/2	0	0	-1	$P^+ + \pi^-$, $N^o + \pi^o$	+1
Antilambda$^+$	$\overline{\Lambda}^o$	1115.2	2.42(-10)	1/2	0	0	+1		-1
Sigma	Σ^+	1189.3	7.9(-11)	1/2	1	+1	-1	$P^+ + \pi^o$, $N^o + \pi^+$	+1
	Σ^-	1196.4	1.7)(-10)	1/2	1	-1	-1	$N^o + \pi^-$	+1
	Σ^o	1190.0	< (-11)	1/2	1	0	-1	$\Lambda^o + \gamma$	+1
Antisigma	$\overline{\Sigma}^-$	1189.3	7.9(-11)	1/2	1	-1	+1		-1
	$\overline{\Sigma}^+$	1196.4	1.71(-10)	1/2	1	+1	+1		-1
	$\overline{\Sigma}^o$	1190.0	< (-11)	1/2	1	0	+1		-1
Xi	Ξ^-	1321.0	(4.6, 200)(-10)	1/2	1/2	-1/2	-2	$\Lambda^o + e^-$	+1
	Ξ^o	?	?	1/2	1/2	+1/2	-2		+1
Anti Xi	$\overline{\Xi}^+$	1321.0	(4.6, 200)(-10)	1/2	1/2	+1/2	+2		-1
	$\overline{\Xi}^o$	?	?	1/2	1/2	-1/2	+2		-1
# K^o	K_1^o	497.9	1.05(-10)	0	1/2	-1/2	+1		0
	K_2^o	497.9	8.1(-8)	0	1/2	-1/2	+1		0
# K^c	K_1^o	497.9	1.05(-10)	0	1/2	+1/2	-1	See Reference G2	0
	K_2^o	497.9	8.1(-8)	0	1/2	+1/2	-1		0

* "Strangeness" Quantum Number

The "elementary" particles, as shown in Table 3-1, are grouped in four classes: photons, leptons, mesons, and baryons(G1)(O1). The class of photons contains only one member, the photon, which is coupled to all other particles through the electromagnetic field. The second class, the leptons, are fermions possessing no strong couplings (fermions are those particles with half integral spin). The third class, mesons, are unstable, spinless particles which have strong coupling. The fourth class, the baryons, are fermions which possess strong couplings and are conserved. The respective antiparticles of these elementary particles are believed to have the same properties, except the sign of the following should be reversed: the charge, the magnetic moment, the Z-component of isotopic spin (T_Z), the strangeness value (S), and the baryon number (N). The charge is related to T_Z, S, and N by the following equation(T1).

$$Q = T_Z + \frac{N}{2} + \frac{S}{2} \qquad 3\text{-}1$$

Isotopic spin (or isobaric spin, as some call it) is associated with the charge of a particle and not with any real intrinsic spin(G2)(J1)(S3).

The following conservation laws apparently hold for all elementary particle interactions:

1. Conservation of charge
2. Conservation of mass-energy
3. Conservation of momentum (linear & angular)
4. Conservation of baryons
5. Conservation of leptons
6. Conservation of "strangeness"*

---

* May not be conserved in weak interactions

7. Conservation of parity*

"Strangeness" can be partly described by considering the nucleons (i.e. the protons and the neutrons) as the basic particles (historically) in the baryon group and the pions (π - mesons) as the basic particles in the meson group. The neutron and the proton constitute a doublet with charges 0 and 1 respectively and with "charge center" at 1/2. Hence, any particle multiplet in the baryon group (except antiparticles) with a "charge center" not at the "expected" 1/2 value is "strange". The strangeness number is twice the value of the shift from the expected value. For example, the neutral lambda particle has charge center at 0; the shift is -1/2 from the expected, thus the strangeness value is -1. Further, the (Xi) doublet, (Ξ^0, Ξ^-), has the charge center -1/2 and is shifted -1 from the expected value. Thus it has a strangeness value of -2. Similarly, in the meson group, the charge center for the triplet (π^-, π^0, and π^+) is at 0; however, the charge center for the (K^0, K^+) doublet is at +1/2; hence a strangeness value of +1. As stated above, the strangeness value for the antiparticle is the same as that for the particle except for a change in sign.

In Table 3-1, the K^0 meson is indicated as being in one of two different states. Each of these states has a different mean lifetime and a different decay mode. K_1^0 decays into two pions and conserves parity; K_2^0 decays into three pions and does not conserve parity.

The approximate thresholds for some particle interactions are given in Table 3-2. The charge is to be supplied and no conservation law must be violated in these strong interactions. N indicates nucleon and the bar indicates the antiparticle.

---

* May not be conserved in weak interactions.

TABLE 3-2

REACTION THRESHOLDS[J1]

Reaction		Threshold (Bev)
π + N →	Λ + K	0.76
	Σ + K	0.90
	N + K + $\bar{K}$	1.36
	Ξ + K + K	2.22
N + N →	N + Λ + K	1.56
	N + Σ + K	1.76
	N + N + K + $\bar{K}$	2.49
	N + Ξ + K + K	3.75

Due to conservation of strangeness, strange particles are produced more than one at a time in nucleon-nucleon or pion-nucleon reactions. The production of antibaryons from nucleon-nucleon interactions requires very energetic particles. For example, the threshold for the reaction P + P → $\bar{P}$ + P + 2P is 5.4 Bev. This is the minimum threshold energy for antibaryon production in nucleon-nucleon interactions.

3.3 NUCLEAR REACTION MODELS

Within their limits of validity, theoretical nuclear reaction models have proved to be useful in explaining systematic variations in experimental data. As a consequence, the models provide excellent guides for making the interpolations and extrapolations so necessary for practical penetration calculations. In some instances,

sufficient experimental data are lacking and calculations from models are used almost exclusively. A discussion of the pertinent nuclear models, with references, follows:

Free Particle Model

According to a model first proposed by Serber[S4], when the bombarding energy is sufficiently high, the motion of the incident nucleon within the target nucleus can be treated classically as a series of successive two-body collisions between the incident nucleon and the individual nucleons of the target nucleus. The Pauli principle is accounted for by requiring a momentum transfer greater than the Fermi momentum of the nucleus considered statistically as an assembly of independent particles. The effect of this is to reduce the effective nucleon-nucleon cross section within the nucleus. A recent paper by Winsberg and Clements[W5] gives the effective nucleon-nucleon cross sections in terms of the Goldberger factor $(1 - KE_f/E_i)$, where E_f is the Fermi energy, E_i is the effective bombarding energy within the nucleus, and K is the parameter calculated by using the differential nucleon-nucleon cross sections to obtain momentum transfers. A plot of K as a function of E_i taken from their paper is given in Figure 3-1. The Fermi energy, of a neutron or a proton, is given by the expression[R6]

$$E_f(i) = \frac{(9\pi)^{2/3}}{2^{2/3}} \frac{\hbar^2}{Mr_o^2} \left(\frac{N_i}{A}\right)^{2/3} \qquad 3\text{-}2$$

where r_o is related to the nuclear radius, R, by $R = r_o A^{1/3}$ and N_i is the number of neutrons or protons within the nucleus. The Fermi energy is approximately 30 Mev for values of $r_o \simeq 1.3 \times 10^{-13}$cm. Due to the forward bias of elastic scattering at high energies, the effect of the Pauli principle is important at quite high bombarding energies. Earlier work used a factor K = 7/5 which was derived by Goldberger[G4] by assuming that the nucleon-nucleon scattering is isotropic in the center-of-mass system.

A fundamental assumption of the Serber model is that $\lambda/2\pi$, where λ is the nucleon wave length, will be much smaller than the average nucleon-nucleon spacing, approximately 2×10^{-13} cm.

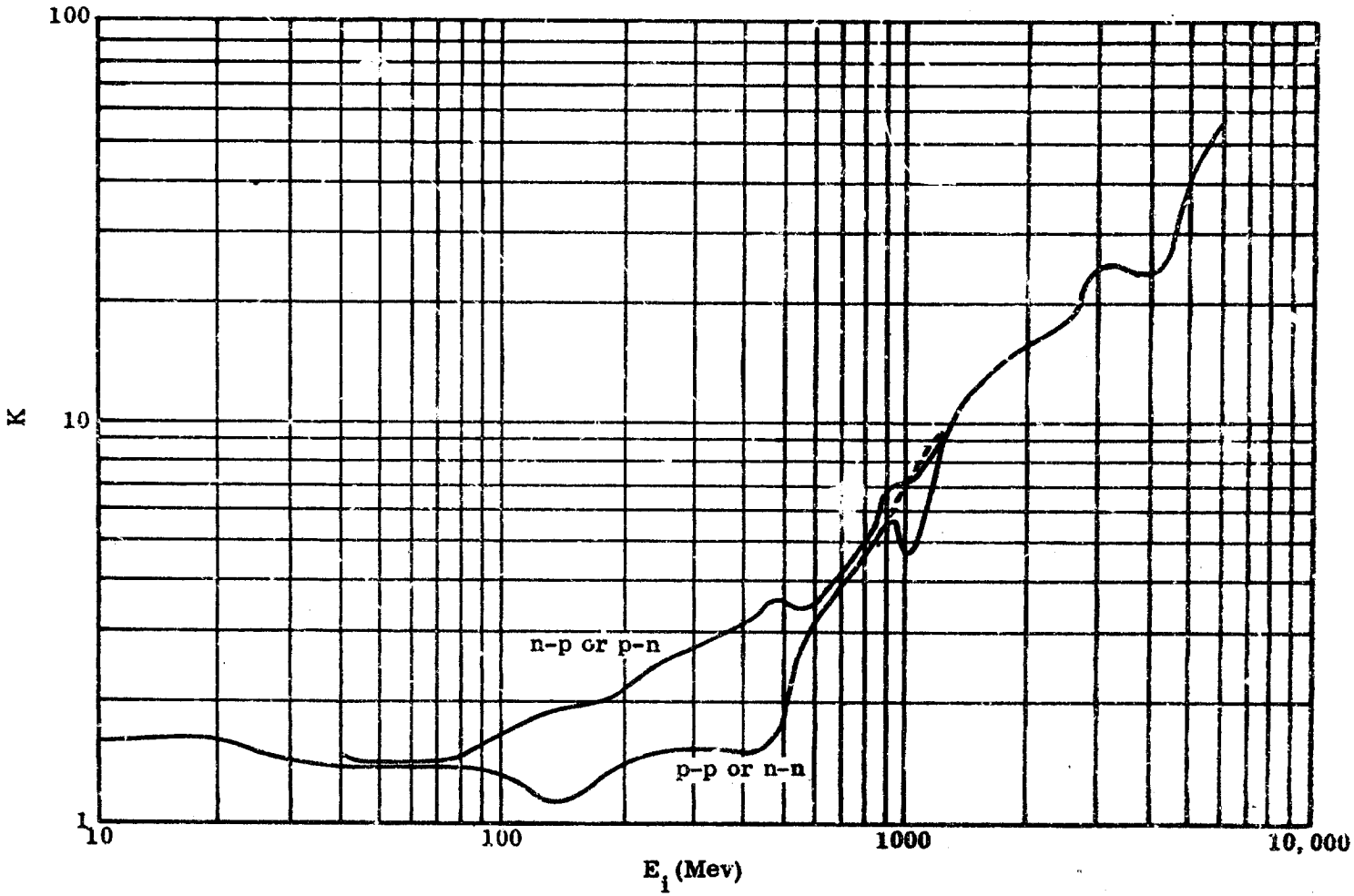

FIGURE 3-1 GOLDBERGER CONSTANT K VERSUS BOMBARDING ENERGY

A plot of ($\lambda\!\!\!^{-} = \lambda/2\pi$) as a function of energy is given in Figure 3-2. If the target nucleons are to be considered as free particles, then wave lengths in the center-of-mass system, which are also shown in Figure 3-2, should be used. It is clear that at energies above 100 Mev, the Serber model is valid. At lower energies, however, we may expect some discrepancies between theory and experiment.

This model was used by Goldberger[G4] and by Metropolis[M7], et al, to calculate the energy spectra and angular distribution of secondary particles produced by direct interactions.

Optical Models

The optical models have been very fruitful in "explaining" the data at almost all bombarding energies. A comprehensive review article by Feshbach[F3] gives the theoretical basis of the model, approximations used to obtain solutions to the problem, and a collection of model parameters obtained by empirical fits of the data at energies up to 300 Mev. In this model, the various many-body reactions are replaced by a potential, V, between the incident particle and the nucleus.

The energy spread of the beam is assumed to be much larger than the spacing between levels in the nucleus so that only average effects of energy levels of the system will be seen. Even though this hypothesis is not fulfilled for the very light elements, differential elastic cross sections have been fitted remarkably well even for 14 Mev neutrons on beryllium.

A semi-classical calculation by Fernbach, Serber, and Taylor[F1] gives results suitable for sufficiently high incident energies. Here it is assumed that the neutron wave length is small compared to internucleon spacing and that scattering has a strong forward bias. The nucleus is described in terms of the nuclear radius R, an absorption constant K, and the increment in the wave number inside the nucleus k_1. Calculated are the absorption cross section σ_a, the total cross section σ_t and the differential elastic cross section $d\sigma/d\Omega$.

For a simple square well, if $KR > 1$, $d\sigma/d\Omega$ is very similar to the diffraction scattering from a cylinder (or black disc), namely

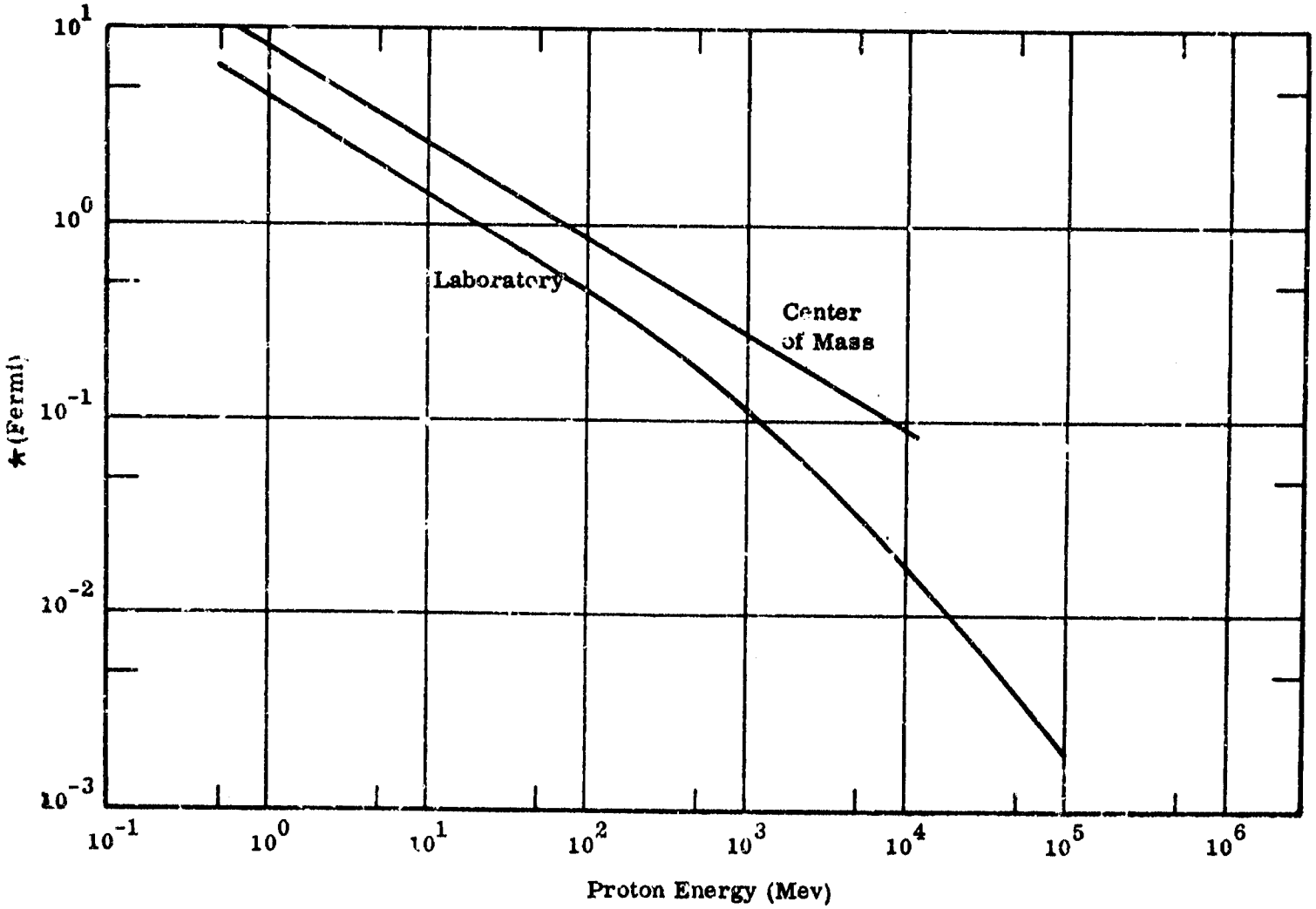

FIGURE 3-2 PROTON WAVE LENGTH

$$\frac{d\sigma}{d\Omega} \sim k^2 (R')^4 \left[\frac{J_1(2kk' \sin \theta/2)}{2kk' \sin \theta/2} \right]^2 \qquad 3\text{-}3$$

where J_1 is a first order Bessel function, $R' = R + 1/k = R + \lambda\!\!\!^{-}$, $1/k = \lambda\!\!\!^{-}$, and k' is the bombarding particle's wave number after collision.

A typical result is shown in Figure 3-3 which shows the experimental data on several elements at 82 Mev compared with the above equation.

The applicability of diffraction scattering is so general that a plot of $[J_1(x)/x]^2$ is presented in Figure 3-4. The angle, at which $d\sigma/d\Omega$ is half maximum to the extent that $\theta \simeq \sin \theta$, is given by

$$\theta_{1/2} = \frac{1.7}{kR} = 1.7 \frac{\lambda\!\!\!^{-}}{R} \qquad 3\text{-}4$$

A plot of $\theta_{1/2}$ as a function of bombarding energy is given in Figure 3-5 for several nuclides of interest. It has been assumed that

$$R = r_o A^{1/3} \qquad 3\text{-}5$$

with $r_o = 1.28 \times 10^{-13}$ cm.

The large forward bias at high energies is apparent. Experimental deviations from this model are usually attributed to a diffuse nuclear boundary and to transparency effects.

The parameters K and k_1 can be expressed in terms of the average nucleon-nucleon cross section $\bar{\sigma}$, the nucleon-nucleon forward scattering amplitude f(0), and the mean nuclear potential.

$$K = A \bar{\sigma}/(4/3)\pi R^3 \qquad 3\text{-}6$$

$$k_1 = 2\pi\rho \lambda\!\!\!^{-} \text{ Re } f(0) = V/hc\beta \qquad 3\text{-}7$$

where ρ is the nuclear density and V the mean nuclear potential. The average cross section for bombarding particles of type i is given by

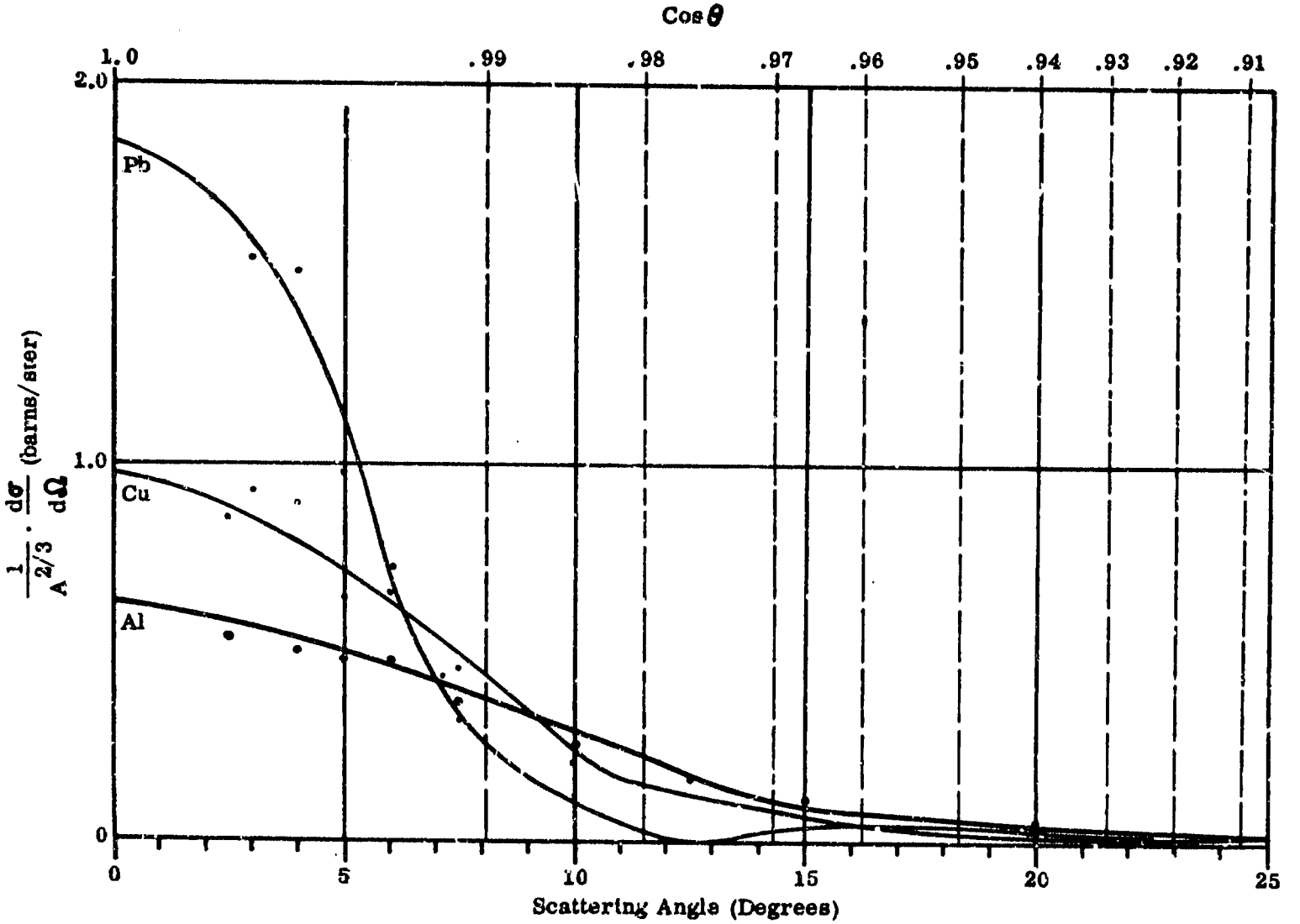

FIGURE 3-3 DIFFERENTIAL ELASTIC SCATTERING OF 83 MEV NEUTRONS

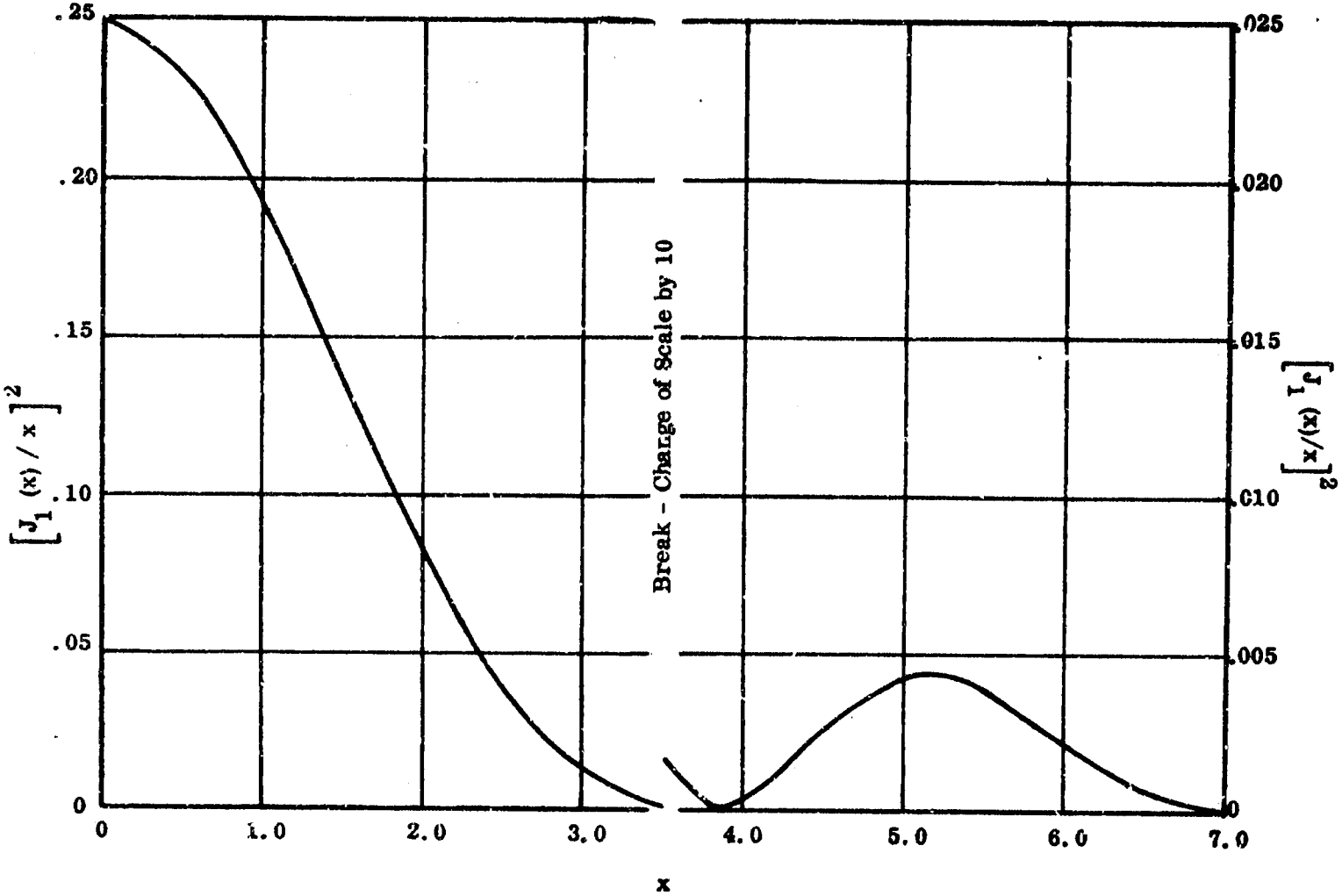

FIGURE 3-4 DIFFRACTION SCATTERING

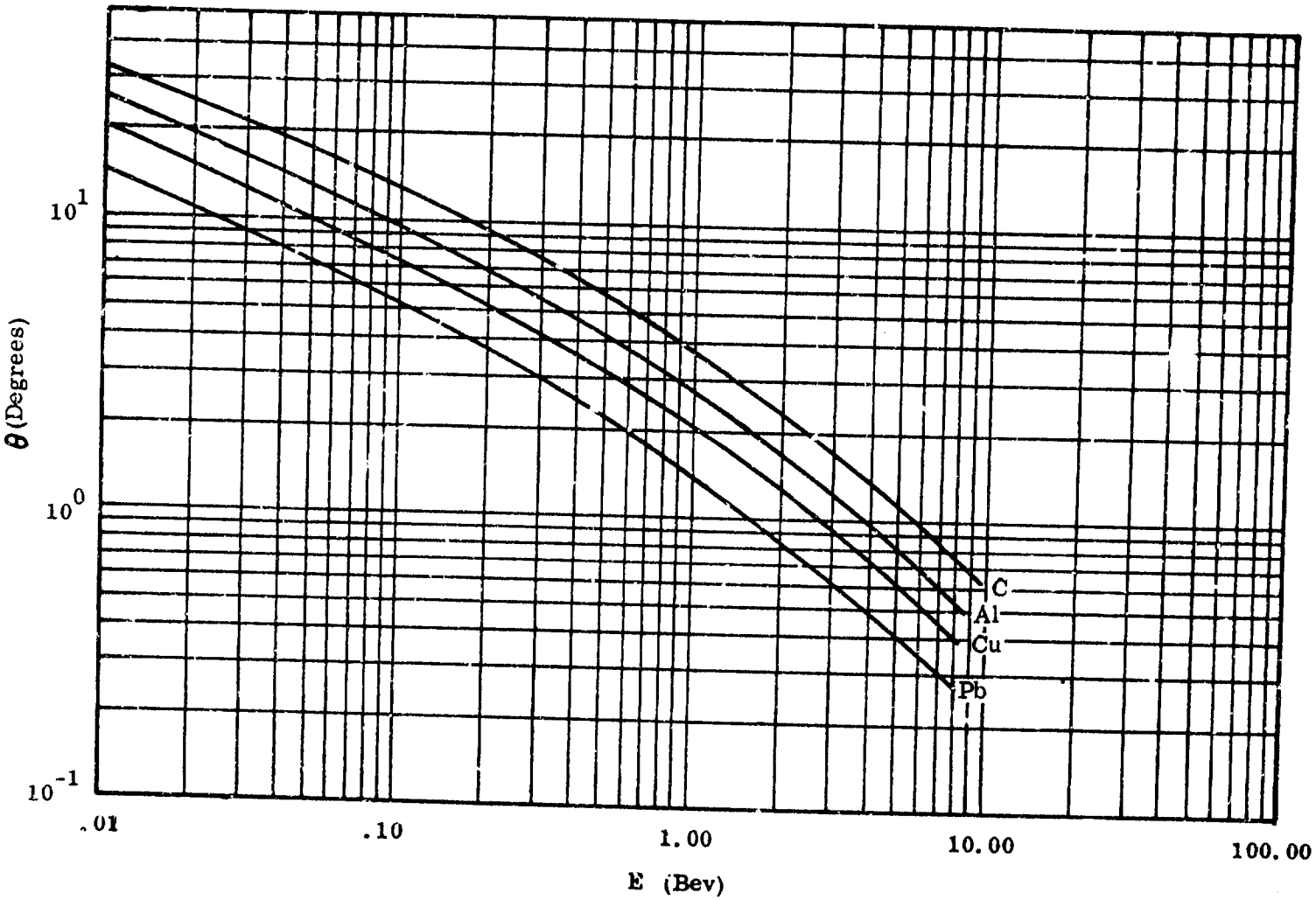

FIGURE 3-5 HALF VALUE ANGLE DIFFRACTION SCATTERING

$$\sigma_i = \frac{N_i \sigma_{ii} + (A - N_i)\sigma_{ij}}{A} \qquad 3\text{-}8$$

where N_i = number of nucleons of type i (neutron or proton) in the nucleus, σ_{ii} is the effective proton-proton (neutron-neutron) cross section and σ_{ij} is the neutron-proton (proton-neutron) cross section. The absorption cross section for a uniform density of nucleons is given by

$$\sigma_a = \pi R^2 \left\{ 1 - \frac{(1 - 2KR)e^{-2KR}}{2K^2R^2} \right\} \qquad 3\text{-}9$$

A phenomenological model developed from the "cloudy crystal ball" of Weisskopf, et al., [W4] has been quite successful in explaining the data for neutron or proton bombarding energies. The nuclear interaction is represented by a potential of the form

$$V = -V_c \rho_c(r) + i W_c q_c(r)$$

$$+ \lambda_\pi^2 \left[V_{so} \frac{1}{r} \frac{d\rho_{so}}{dr} + i \frac{W_{so}}{r} \frac{dq_{so}}{dr} \right] \vec{\sigma} \cdot \vec{L} \qquad 3\text{-}10$$

where λ_π is the Compton wave length of the pi meson (1.4×10^{-13} cm), V_{xx} and W_{xx} are constants depending on bombarding energy, ρ and q are functions of r to express the effects of a diffuse nuclear surface, $\vec{\sigma}$ is the particle spin vector, and $\vec{L}$ is the orbital angular momentum vector.

A table of the various functions ρ and q used in the literature is given in the article by Feshbach [F3]. Bjorklund and Fernback [B11] obtain excellent fits to all the data up to several hundred Mev with

$$\rho_c = \rho_{so} = q_{so} \qquad 3\text{-}11$$

and

$$\rho_c(r) = \left[1 + \exp (r - R)/a\right]^{-1}; \; a = 0.65 \times 10^{-13} \text{ cm} \qquad 3\text{-}12$$

$$q(r) = \exp\left[-(r - R)^2/b^2\right]; \; b = 0.98 \times 10^{-13} \text{ cm} \qquad 3\text{-}13$$

$$R = r_o A^{1/3}; \; r_o = 1.25 \times 10^{-13} \text{ cm} \qquad 3\text{-}14$$

These models are used for calculating

σ_t = total cross section

$\sigma_c = \sigma_a + \sigma_{fl}$, the cross section for compound nucleus formation

$\frac{d\sigma_{se}}{d\Omega}$ = shape-elastic differential cross section

Here σ_{fl} is the "fluctuation" cross section; it is associated with compound elastic scattering at low bombarding energies and is negligible at higher energies.

This model should be used if accurate cross sections are desired at energies up to, say, 80 Mev. Beyster[B10] gives tables enabling cross section calculation for neutrons on 26 elements for bombarding energies up to 18 Mev. Potential parameters are given by Bjorklund and Fernback[B12] and by Feshbach[F3] for energies up to 300 Mev for protons and neutrons.

3.4 NUCLEON-NUCLEON CROSS SECTIONS

Basic nucleon-nucleon cross sections are important because hydrogen and hydrogen-bearing plastics are likely materials for space radiation shielding. Furthermore, it is indicated in Section 3.3 that non-elastic cross sections for nucleons on complex nuclei may be calculated from nucleon-nucleon cross sections. The data presented here are largely from the review by Hess[H4] supplemented by references to the more recent literature. These cross sections are plotted in Figures 3-6 and 3-7.

The only reaction of significance below the threshold for meson production at 290 Mev is elastic scattering. Single meson production predominates for bombarding energies below 1 Bev. At higher bombarding energies, multiple meson production and the production of other particles becomes possible. The threshold energies for these reactions are given in Section 3.2.

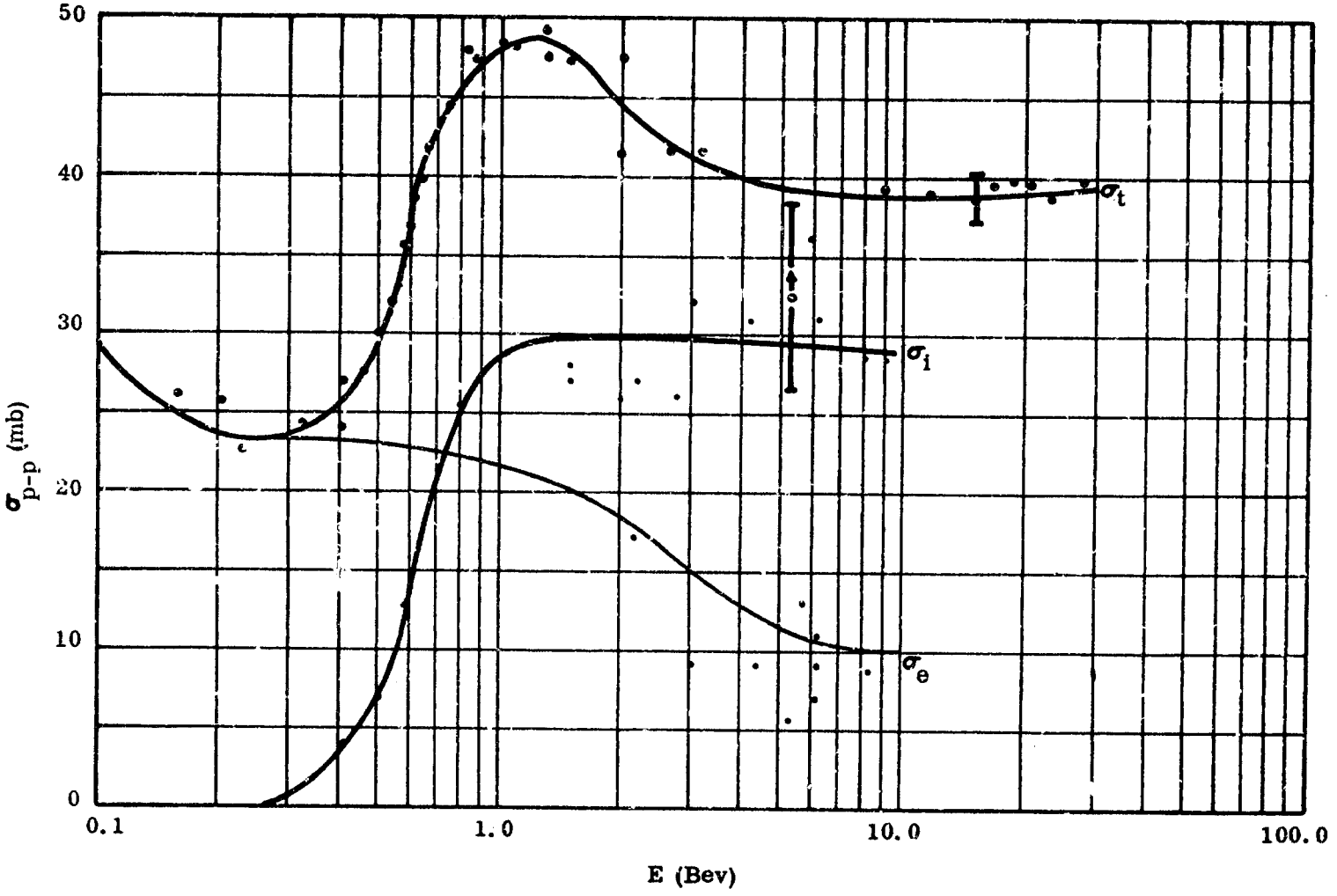

FIGURE 3-6 PROTON-PROTON CROSS SECTIO.

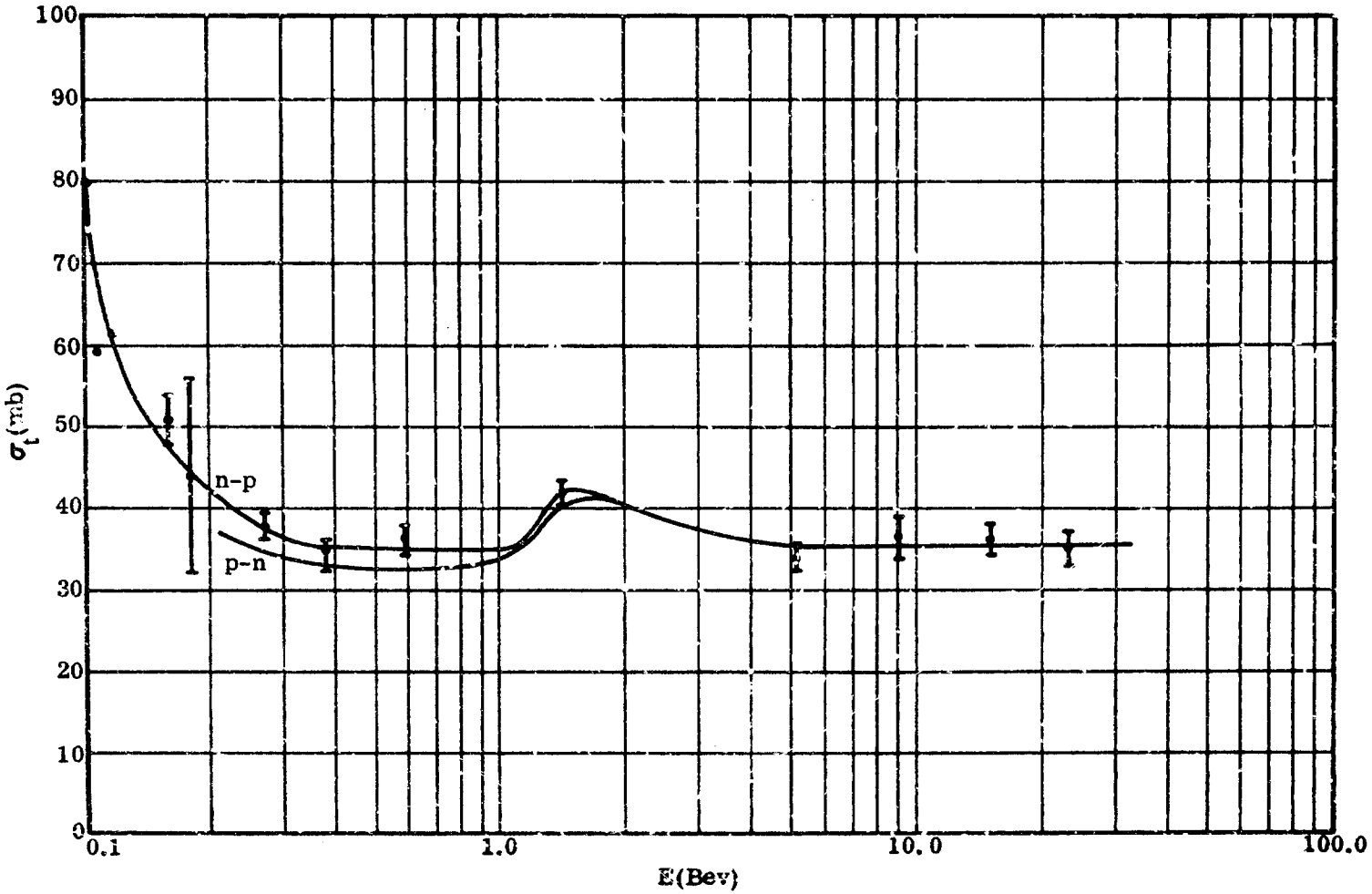

FIGURE 3-7 n-p AND p-n CROSS SECTIONS

The proton-proton cross sections are easiest to measure. Beams of precisely known energy may be extracted from an accelerator to bombard liquid hydrogen. Total cross sections have been measured at bombarding energies up to almost 30 Bev. Disregarding Coulomb effects, the neutron-neutron cross section is assumed in current theories to be equal to the proton-proton cross section. No evidence to the contrary has been found.

Angular distributions have been measured both for elastic and inelastic events. The reivew by Hess[H4] gives the differential elastic proton-proton cross sections at several bombarding energies up to 4400 Mev. Neutron-neutron scattering has been measured at 300 and 590 Mev and is similar to proton-proton scattering. The p-p scattering becomes peaked in the forward direction in the neighborhood of 20 Mev, largely due to Coulomb and Coulomb-nuclear effects; the scattering becomes more peaked in the forward direction as bombarding energy is increased, particularly at bombarding energies above 500 Mev. The neutron-proton and proton-neutron cross sections (which are the same) are somewhat more difficult to measure. High energy beams of neutrons well defined in energy are difficult to obtain. Energy spreads of the order of 20% (full width at half maximum) are not uncommon. The proton-neutron cross section may be measured by the difference between proton-deuteron and proton-proton cross sections. There is a large correction for screening by the "spectator" particle in the deuteron with a resultant uncertainty in cross section. The correction becomes smaller as bombarding energies are increased. In Figure 3-7, separate curves are drawn for the p-n cross sections measured by the difference method and for the n-p cross sections measured directly. Angular distributions for elastic scattering are also given by Hess[H4]. They are approximately symmetrical about 90° in the center-of-mass system and are almost flat below 40 Mev; the "dip" at 90° increases rapidly with bombarding energy above 50 Mev.

3.5 NUCLEON-NUCLEUS CROSS SECTIONS

3.5.1 Total Cross Sections

The total nucleon-nucleus cross sections are measured in a "good geometry" attenuation experiment. In practice, transmissions must be corrected for elastic scattering into the finite solid angle subtended by the detector. Coulomb effects for high energy protons (Energy > 1 Bev) or for high Z materials make these corrections large. As a consequence, total proton cross sections have been measured at the higher bombarding energies only for low Z materials. The experimental techniques for total cross section measurement is simple in principle, and data exist for a large number of bombarding energies and target nuclei. Representative data are given in Table 3-3. Plots of cross section as a function of bombarding energy for several elements are given in Figure 3-8 and as a function of mass number of target nuclei for several bombarding energies in Figure 3-9. From the table, it is evident that neutron and proton cross sections are approximately the same. No distinction of bombarding particles is made in Figure 3-8. The increase in cross section at bombarding energies above 300 Mev is often attributed to meson threshold effects, but no such rise is observed in non-elastic cross sections, as will be shown later. From Figure 3-9, a smooth dependence on mass number is observed for bombarding energies above 95 Mev. The structure in the curves at lower energies is due to "giant resonance" effects described by the optical model with a diffuse surface described in Section 3.3.

Total cross sections as such are not used directly in penetration calculations of high energy protons. However, the elastic scattering cross sections are obtained from the difference between total and non-elastic cross sections.

3.5.2 Differential Elastic Scattering Cross Sections

The general characteristics of elastic scattering of nucleons by nuclei is discussed in Section 3.3. In that section, typical experimental data are also presented. References of pertinent experimental data are given in Table 3-4, which is largely self-explanatory. In this table, θ_{max} and θ_{min} give the maximum

TABLE 3-3

TOTAL CROSS SECTIONS (BARNS)

Bombarding Energy (Mev) - Particle			14N	20N	28.8N	42N	95N	400P	470N	490N	510P	550N	580N	630N	650N	660P	1400N	5000N	410N	408P
Energy "Resolution"								±4			±							400		
Reference			Mc3	D1	Mc3	H8	D5	D3	D4	F4	D3	A4	D12	D12	D12	D12	B18	C12	A10	N1	M6
Cross Section Precision								2%	1-3%	1-2%								5%	5%		
Element	Z	A																			
n	0	1.00										0.0333	0.033	0.030	0.036	0.040					
H	1	1.00	0.720		0.338	0.203	0.073	0.0365	0.038	0.033	0.0345	0.0375	0.034	0.035	0.036	0.037			0.0336	0.0337	0.0216
D	1	1.00	0.860			0.289	0.104	0.0610	0.057	0.049	0.0568	0.0569	0.057	0.055	0.073	0.077				0.0630	0.0351
He	2	4.00		0.816																	
Li^6	3	6.00	1.45																		
Li	3	6.94	1.50			0.654				0.164											
Be	4	9.01	1.51			0.853	0.390	0.247	0.229	0.225	0.289		0.232	0.249	0.261	0.274		0.310		0.231	0.242
B	5	10.82				0.985															
C	6	12.01	1.31	1.45	1.32	1.080	0.498	0.296	0.288	0.279	0.292	0.293	0.286	0.306	0.319	0.338	0.342	0.360	0.319	0.297	0.285
N	7	14.00				1.220	0.570														
O	8	16.00				1.358	0.663	0.395	0.372	0.380	0.279	0.386	0.376	0.398	0.407	0.422				0.278	0.406
F	9	19.00	1.77	1.64	1.75	1.603															
Ne	10	20.18																			
Na	11	22.90				1.67															
Mg	12	24.32	1.79			1.723															
Al	13	26.96	1.75	1.84		1.782	0.993	0.592	0.553	0.566	0.560	0.565	0.582	0.612	0.631	0.645	0.823	0.700	0.614	0.587	
Si	14	28.09		1.84																	
P	15	30.98																			
S	16	32.07				1.974		0.680			0.686									0.072	
Cl	17	35.46				2.11	1.28	0.740			0.740									0.742	
A	18	39.94																			
K	19	39.10																			
Ca	20	40.08				2.210															
Sc	21	44.96																			
Ti	22	47.90	2.35		2.42																
V	23	50.95																			
Cr	24	52.01	2.42		2.26																
Mn	25	54.94																			
Fe	26	55.85	2.54	2.23		2.441															

TABLE 3-3 (Continued)

Bombarding Energy (Mev) - Particle			14N	20N	28.8N	42N	95N	208P	270N	280N	310P	350N	380N	500N	590N	630N	900P	1100N	6000N	410N	406P
Energy "Resolution"								±4			±8								400		
Reference			Mc3	31	Mc3	H8	D5	D3	D4	F4	D3	A8	D12	D12	D12	D12	B16	C13	A10	N1	M6
Cross Section Precision								2%	1-3%	1-2%								3%	5%		
Element	Z	A																			
Co	27	58.94			2.41																
Ni	28	58.71	2.70		2.37	2.510															
Cu	29	63.54	2.95	2.56	2.46	2.540	3.00		1.145	1.19		1.138	1.170	1.210	1.250	1.310	1.530	1.390	1 158	1.167	
Zn	30	65.38	3.11		2.52	2.618															
Ga	31	69.72	3.18		2.56																
Ge	32	72.60	3.34		2.61																
As	33	74.91																			
Se	34	78.96																			
Br	35	79.92		2.98		2.93															
Kr	36	83.80																			
Rb	37	85.48																			
Sr	38	87.63				2.99															
Y	39	88.92																			
Zr	40	91.22	3.93	3.60	2.87																
Nb	41	92.91																			
Mo	42	95.95	3.96		2.90	3.11															
Pd	46	106.40	4.29		3.16																
Ag	47	107.88	4.33		3.17	3.229															
Cd	48	112.41	4.51		3.25															1.648	
In	49	114.82	4.62		3.31																
Sn	50	118.70	4.66		3.38	3.251	3.18		1.87	1.83		1.887	1.890	1.930	1.980	2.030		2.200	1.986		
Sb	51	121.76	4.68		3.41																
Te	52	127.61																			
I	53	126.91				3.51															
Xe	54	131.30																			
Cs	55	132.91																			
Ba	56	137.36				3.57															
La	57	138.92																			
Hf	72	178.50																			
Ta	73	180.95	5.10		4.52	4.20															

TABLE 3-3 (Continued)

Bombarding Energy (Mev) - Particle			24N	40N	28.8N	42N	95N	208P	270N	280N	310P	350N	380N	500N	590N	630N	900P	1400N	5000N	410N	408P
Energy "Resolution"								±4			±8								400		
Reference			Mc3	D1	Mc3	H8	D6	D3	D4	F4	D3	A8	D12	D12	D12	D12	B13	G12	A10	N1	M6
Cross Section Precision								2%	1-3%	1-2%								3%	5%		
Element	Z	A																			
W	74	183.86	5.40		4.70	4.31			2.61				2.690								
Pt	78	195.09	5.38		4.92																
Au	79	197.00			4.99																
Hg	80	200.61				4.51				2.80											
Tl	81	204.39	5.45		5.19																
Pb	82	207.21	5.42	5.96	5.38	4.44	4.46		2.84	2.89		2.838	2.310	2.850	2.920	2.940		3.210	2.534	2.890	
Bi	83	209.00	5.44	5.69	5.39	4.58												3.280			
Th	90	232.05				5.03															
U	92	238.07		5.94		5.12	4.92		3.22	3.14			3.250	3.270	3.290	3.300		3.640		3.210	
U^{235}	92	235.00			5.81															3.230	
U^{238}	92	238.00	5.90		5.79																

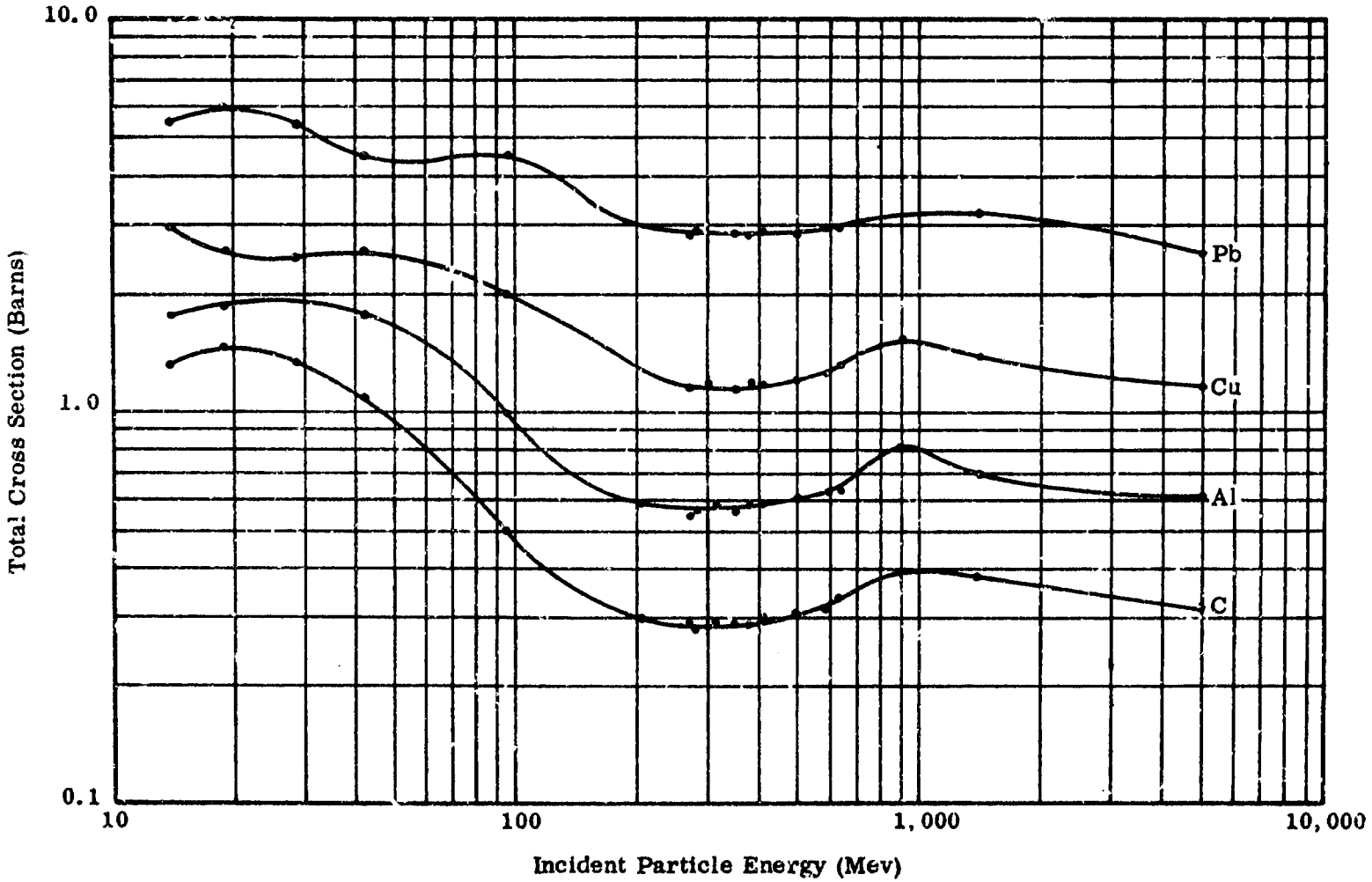

FIGURE 3-8 TOTAL CROSS SECTION AS A FUNCTION OF ENERGY

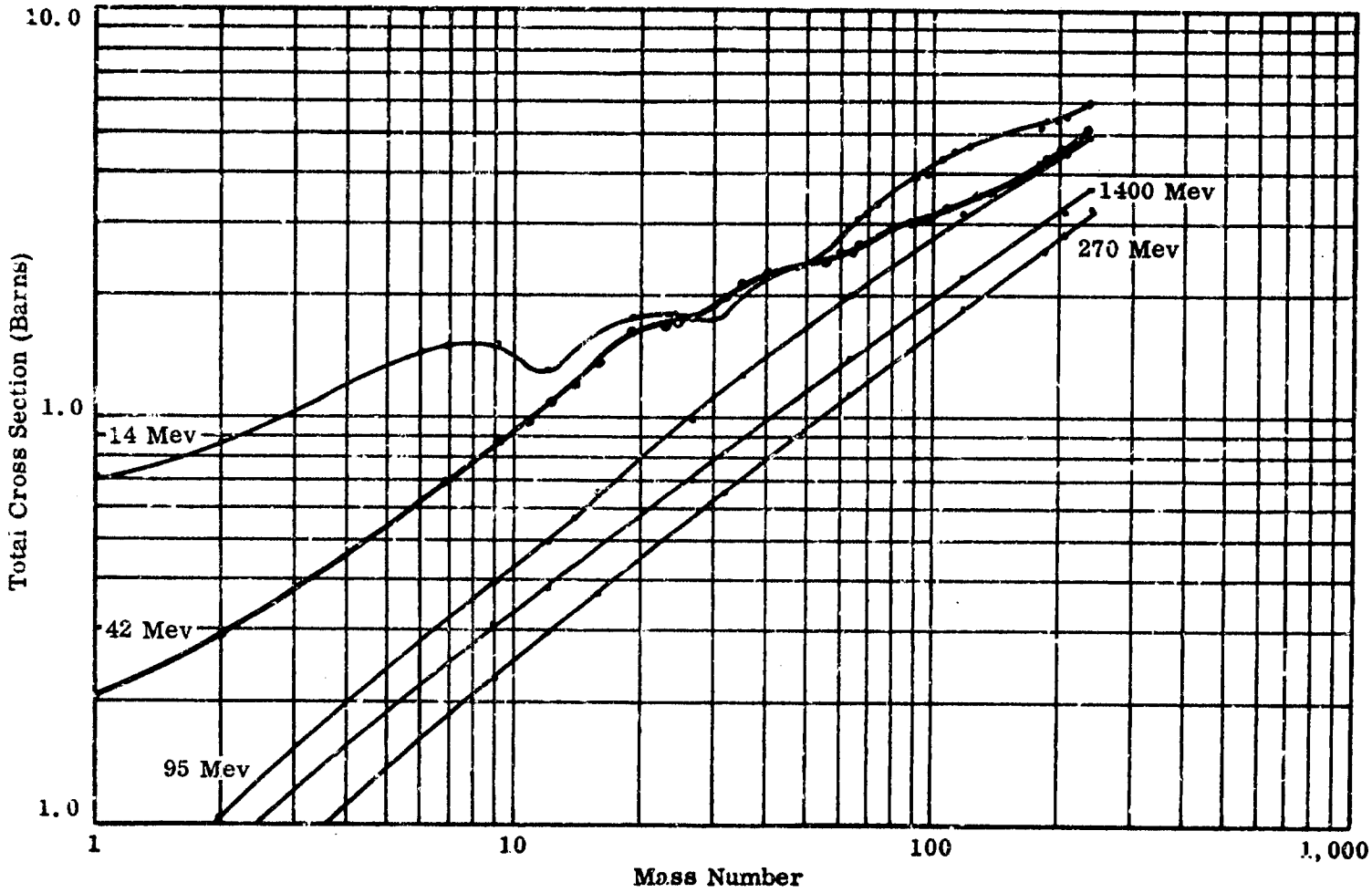

FIGURE 3-9 TOTAL CROSS SECTION AS A FUNCTION OF MASS NUMBER

TABLE 3-4

DIFFERENTIAL ELASTIC CROSS SECTIONS

Particle	Bombarding Energy (Mev)	θ_{min} (degrees)*	θ_{max} (degrees)*	Target(s)	Comments	Ref.	Author	Year
Neutron	84	2.5	25.0	Al, Cu, & Pb	σ_t & σ_e given	B21	Bratemahl	1950
Proton	340			C, Mg, Al, Si, S, Cu, Ag, Ta, W, Pb, & Bi	$(d\sigma/d\Omega)$ given graphically Same σ_e's given	P1	Richardson	1952
Neutron	83	2.0	25.0	Be, C, Al, Cu, Ag, & Pb	Same σ_t & σ_e	H7	Hildegrand	1951
Proton	300			Pb, Al, Ca, Fe, Ta, He, Be, & C	Presented graphically Optical Model	B13	Bjorklund	1957
Neutron	4.1, 7, 14			Sn, Cu, Fe, Al, Pb, Ta, Bi, & Zn	Presented graphically Optical Model	B14	Bjorklund	1958
Proton	14-20	7.0	86.0	Carbon	Tables for 14 energies	P3	Peelle	1957
Neutron	300	2.0	18.0	C, Al, Cu, & Pb	σ_e, σ_i, & σ_t also given	B3	Bail	1952
Neutron	96	1.0	28.5	U, Pb, Be, Cd, Cu, Li, Al, & C	θ in C.M. system	S1	Salmon	1960
Proton	142	4.0	20.0	Be, C, N, O, & Al	σ_t also given	T1	Taylor	1951
Neutron	0-14	0.0	180.0	Many	Cos θ in C.M. system	H11	Hughes	1956
Neutron	14.6	18.9	167.0	Be, C, Fe, Ag, Cd, Sn, & Pb		Mc3	McGregor	1958

* Lab angle unless stated otherwise in comments.

and minimum angles at which data were observed. In some instances the authors have integrated the differential elastic curve to obtain the elastic cross section. In order to do this the data must be extrapolated to 0^{o} and 180^{o}. A relatively large error is possible in this process.

3.5.3 Non-Elastic Cross Sections

Non-elastic cross sections are usually measured in a "poor geometry" experiment when the elastic scattering is predominant in the forward hemisphere. Sphere transmission techniques are also available for lower bombarding energies. Both techniques are often difficult to apply in practical cases so that the data are not so prolific as total cross section measurements. Representative data are given in Table 3-5 and are plotted in Figures 3-10 and 3-11. The smooth dependence on mass number, except at energies below 100 Mev, is significant. Furthermore, cross sections change very little at bombarding energies above 200 Mev. Recent measurements in the neighborhood of 25 Bev[L8] found non-elastic cross sections almost identical to those at 1.4 Bev. These data suggest that the number K in Equation 3-6 may be considered a constant of nuclear matter at these bombarding energies, at least for the accuracy of present secondary production calculations. Futhermore, there is apparently no significant difference between neutron and proton cross sections at the high energy range. For neutrons less than 100 Mev, additional non-elastic cross sections may be found in BNL 325[H12].

3.5.4 Other Cross Sections

Of particular interest to secondary particle analysis are the details of non-elastic collisions. Reactions of the type $(p, xp' + yn)$, where x and y are integers, can be measured by radiochemical techniques. A review by Miller and Hudis[M9] summarizes the earlier work in this field. The number of reaction products for a given bombarding energy and target nucleus can be quite large, as is exemplified in a recent paper by Rudstam, et al[R8] on the so-called spallation of copper by high energy protons. Radiochemical techniques do not yield information as to the energy and angular distribution of reaction products.

TABLE 3-5

σ_{ne} (barns)

Energy (Mev)	Incident Nucleon	Ref.	Be	C	Al	Fe	Cu	Sn	Pb	Bi	U
14.2	N	Mc3	.49 ±.02	.56 ±.02	.97 ±.02	1.36 ±.03	1.49 ±.02	1.9 ±.03	2.56 ±.03	2.56 ±.04	
25.5	N	Mc3	.38 ±.05	.44 ±.04	.81 ±.05	1.21 ±.07	1.53 ±.07	1.77 ±.08	2.56 ±.10	2.43 ±.10	
29.2	N	Mc3		.45 ±.04			1.30 ±.07	1.83 ±.10	2.6 ±.10		
34 ±2.5	P	G7		.445 ±.02	.60 ±.042	.902 ±.072		1.93 ±.10	1.78 ±.12		
84	N	H9			.467		.838		1.77		
95	N	D5		.224 ±.02			.782		1.75		
160-205	P	H6	.172 ±.008	.204 ±.012	.408 ±.025		.746 ±.045		1.55 ±.11		1.90 ±.13
205-270	P	H6	.169 ±.006	.202 ±.007	.383 ±.012		.667 ±.031		1.57 ±.07		1.77 ±.07
270	N	D4		.145			.570		1.443		
270-335	P	H6	.151 ±.004	.187 ±.006	.334 ±.009		.608 ±.022		1.48 ±.06		1.60 ±.06
300	N	B3		.203 ±.033	.390 ±.023		.755 ±.033		1.72 ±.08		
900	P	B18		.230 ±.02	.370 ±.029		.740 ±.052		1.66 ±.05		
1400	N	C12	.187 ±.012	.200 ±.013	.410 ±.023		.670 ±.034		1.73 ±.045	1.79 ±.055	1.89 ±.098
2200	P	L8	.236 ±.004	.260 ±.006	.503 ±.016		.914 ±.044				
2800	P	B20		.230 ±.012		.690 ±.028			1.63 ±.075		
3600	N	B5			.430 ±.056		.704 ±.14		1.93 ±.3		
5000	N	A10		.235 ±.016	.381 ±.027		.586 ±.025		1.67 ±.08		
24,000	P	L8	.180	.210	.400		.710				
61 ±4.5	P	M8		.20 ±.013	.392 ±.025	.617 ±.04		.995 ±.07	1.49 ±.077		
860	P	C3	.169 ±.015	.209 ±.022	.394 ±.01		.728 ±.017	1.11 ±.03	1.68 ±.04		

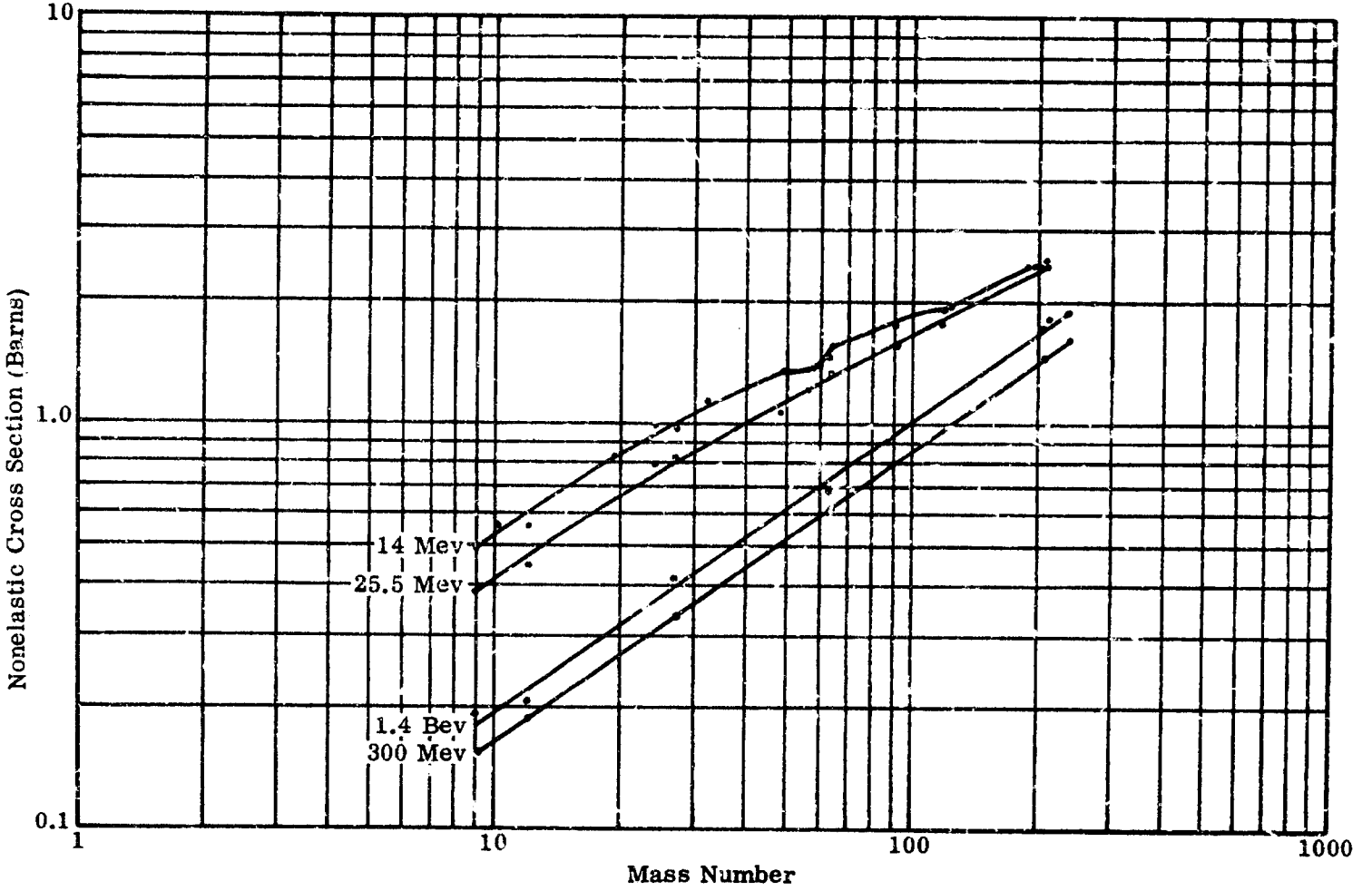

FIGURE 3-10 NONELASTIC CROSS SECTION AS A FUNCTION OF MASS NUMBER

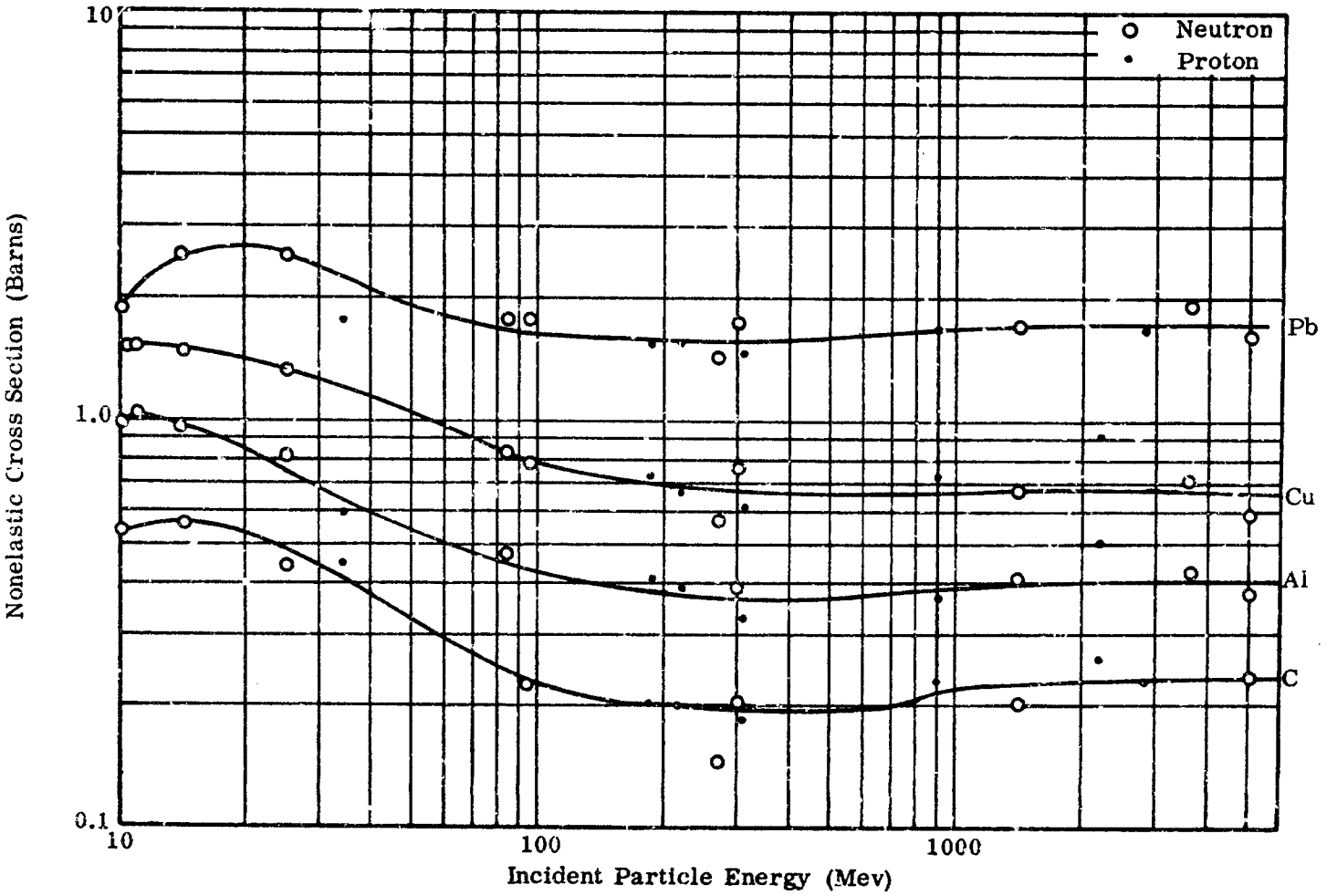

FIGURE 3-11 NONELASTIC CROSS SECTION AS A FUNCTION OF ENERGY

A few measurements of the energy distribution of reaction products have been performed. In these instances measurements have been made of $d^2\sigma/d\Omega dE$ as a function of energy of the secondary particle and as a function of angle of observation. References to some of these measurements are given in Table 3-6. A typical spectrum of protons from inelastic scattering of 95 Mev protons incident on carbon is given in Figure 3-12. A number of fluctuations which correspond to energy levels of the target nucleus can be observed in the spectral intensity. The magnitude of these fluctuations decreases as the mass number of the target is increased and as the bombarding energy is increased. The simple structural models of Section 3.3 are incapable of predicting the details which are observed. Tyren and co-workers(T3 through T7) integrated the intensity under the peaks observed at energy levels corresponding to 4.3 and 9.6 Mev excited in carbon by 182 Mev protons to obtain cross sections for excitations of 5.3 and 2.4 millibarns respectively.

The total inelastic cross sections of carbon at this bombarding energy is 200 millibarns according to Figure 3-11. Thus the effects of the peaks are only a few percent of the total. Tyren and Maris(T4, T5, T6, T7) have observed that for 185 Mev protons the angular distribution of secondaries depends on the energy of the secondaries; that is to say, the spectra depend on the angle of observation. For some energies of the inelastically scattered protons a dip in the forward direction was observed together with peaks at, say, 20° in the laboratory system.

A particular type of nucleon-nucleus (p, 2p) interaction has been named "quasi-elastic scattering". Two spectrometers in coincidence are used for the measurements, and the distribution in energy and angle of coincident protons is observed. From these measurements, the energy distribution in the nucleus of the nucleons participating in direct interactions is inferred. If a target nucleon is at rest, a nucleon-nucleon collision results in two moving nucleons with coplanar trajectories at 90 degrees to each other. The sum of the energies of the two nucleons is equal to the bombarding energy. A distribution of motion of target nucleons, such as those within a nucleus, will result in a distribution in summed energy and in angle of the resultant nucleons. Measurements

TABLE 3-6

$$\frac{d^2\sigma}{dEd\Omega}$$

Ref.	Bombarding Energy	Outgoing Particle	E_{min}	E_{max}	Angles Measured	Targets	Detector
A1	315P	N	5		53, 90, 127(lab)	Be^9, N^{14}, Al^{27}	Bubble Chamber
S9	96P	P	~30		40		
G11	18P	P				Al, Fe, Ni, Cu, Ag, Sn, Pt, Au	
H10	19P	P	4		30 to 160	O^{16}	
E2	31P	P	5		30, 45, 60, 90, 135	Pb, Au, Ta, Sn	
B1	190P	P				C, Al, Ni, Ag, Au	
	205α	d	~5	~90	45, 90, 135	C, Al, Ni, Ag, Au	
G10	190P	N	0.5	14			
B6	31P	P, d, HC	50 mg/cm^2 Al		15-150 in lab	Be	
C9	23P	P, d	14	23	60, some at 45 & 90	Bi, $Pb^{206, 207, 208}$, Au, Pt, Th Observed Structure	NaI Scint.
C10	14-19P	P	Q defined		15-180		
P3	14-19P	P	Q defined		10-100	C	
N3	23P	P				C Theoretical Interpretation	
A4	14N	P, np				Al, Fe, Ni, Cu; compound & direct separated	
T4	185P	P				Mg, Al, Si, S, A, K	
T8	185P					Li, Be, B, N, V, Cr, Fe, Co, Ni, Cu, Zn, O, CaC	

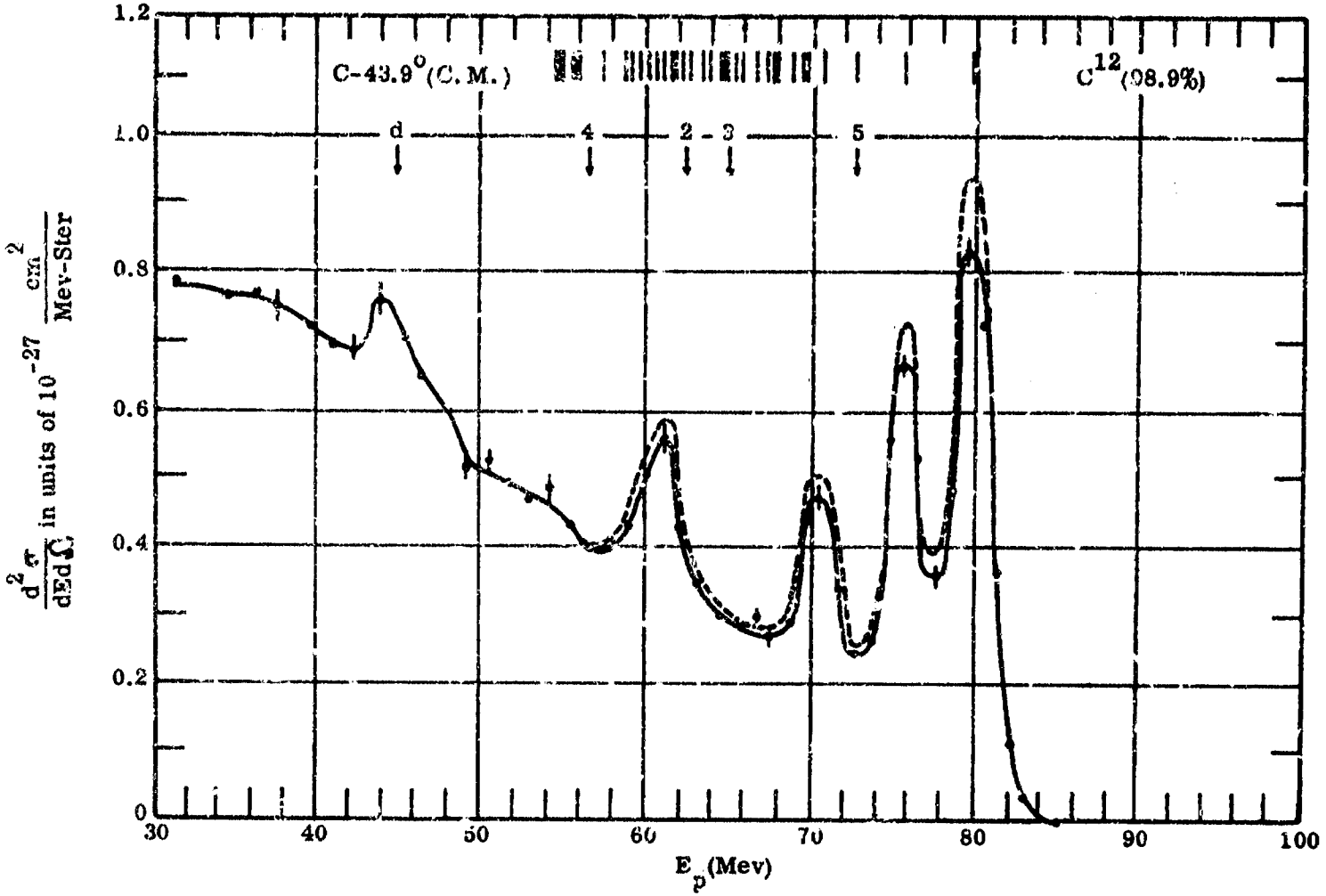

FIGURE 3-12 ENERGY SPECTRUM OF PROTONS SCATTERED FROM CARBON (C.M.)

of quasi-elastic scattering are summarized in Table 3-7. The general results indicate that only nucleons at the surface participate in quasi-elastic scattering at bombarding energies below 50 Mev, but that the entire nuclear volume participates in these reactions at bombarding energies in the neighborhood of 200 Mev. The energy level structure of the target nucleus affects the distribution but probably not enough to perturb secondary production calculations based on an energy continuum.

3.6 PIONS AND PION REACTIONS

Pions, or pi mesons, are produced in nucleon-nucleon collisions at bombarding energies above 290 Mev. For nucleons bound in a nucleus, the threshold is somewhat lower due to internal motion within the nucleus. Thus, some pion production is to be expected at bombarding energies of interest to space shielding.

Both the stopping power and the range of non-relativistic charged pions are approximately equal to those of protons of energy m_p/m_π (= 6.7) times the pion energy. Thus, for example, a one Mev charged pion has the range and stopping power of 6.7 Mev proton. The time required to stop a pion in solid materials is short compared to its mean life. Upon stopping, negative pions form "mesic atoms" with the emission of quasi-optical photon radiation of up to 5 Mev for Z = 92. Calculations of this radiation are complicated by the fact that some particle orbits lie within the nucleus. Marshak[M5] discusses the slowing down of pions and the energy levels of mesic atoms.

The mean life of the neutral pion is 2×10^{-16} seconds, and it decays into two gamma rays each with an energy equal to half the rest mass (68 Mev) augmented by the kinetic energy of the pion. High energy gamma ray phenomena have been discussed extensively by Rossi[R6]. Charged pions decay into muons and neutrinos. The muons, having the same order of magnitude of mass as the pions, will have similar ionization properties, but they do not interact strongly with nuclei. The mean lifetime for the charged pion decay process is 2.5×10^{-8} seconds in the frame of reference in which the

TABLE 3-7

QUASI ELASTIC (p, 2p) SCATTERING

Proton Energy Mev	Targets	Comments	Reference
23	Ni^{58}	Some level structure observed	C8, Cohen, 1957
40	Ni, Cu, Pb	Surface effect apparent	G9, Griffiths & Eisbert, 1959
153	C	P-state at 16 Mev	G6, Gouding & Pugh, 1960
185	Li, Be, B, C, N, O, Ca	Plots of S & P-state energies given	T5, Tyren, 1959
350	Li	Nucleon kinetic energy ~20 Mev in nucleus	C2, Chamberlain & Segre, 1952

pion is at rest. A charged pion of kinetic energy, T, will travel a distance of

$$L = \text{speed} \times \text{mean life} = 7.5 \times 10^2 \left[(1 + T/m_o c^2)^2 - 1\right]^{1/2} \text{ cm}$$

in one mean life. The Einstein time dilation has been included in the equation.

For low kinetic energies ($T << mc^2$)

$$L \simeq 2.8 \times 10^2 \, T^{1/2} \text{ (Mev) cm}$$

Thus, only very low energy charged pions will decay appreciably within the distance of two meters.

At low bombarding energies, pions interact with nucleons in the following typical reactions:

I	$\pi^+ + p \rightarrow \pi^+ + p$ $\pi^- + p \rightarrow \pi^- + p$	(elastic scattering)
II	$\pi^+ + n \rightarrow \pi^o + p$ $\pi^- + p \rightarrow \pi^o + n$	(charge exchange)
III	$\pi^+ + n \rightarrow \gamma + p$ $\pi^- + p \rightarrow \gamma + n$	(radiative capture)

At higher bombarding energies, other reactions occur which result in the production of strange particles or more than one pion. Some of these reactions proceed by the production of extremely short-lived particles ($< 10^{-20}$ sec) which decay into two or three pi mesons. These particles have been variously called rho, omega, and eta mesons, and they are of intense interest in basic physics but of little interest for applied calculations where gross meson production is properly considered.

Plots of the total pion-nucleon cross section for both positive and negative mesons are given in Figures 3-13 and 3-14. It is evident that a number of resonances occur. The first, in the neighborhood

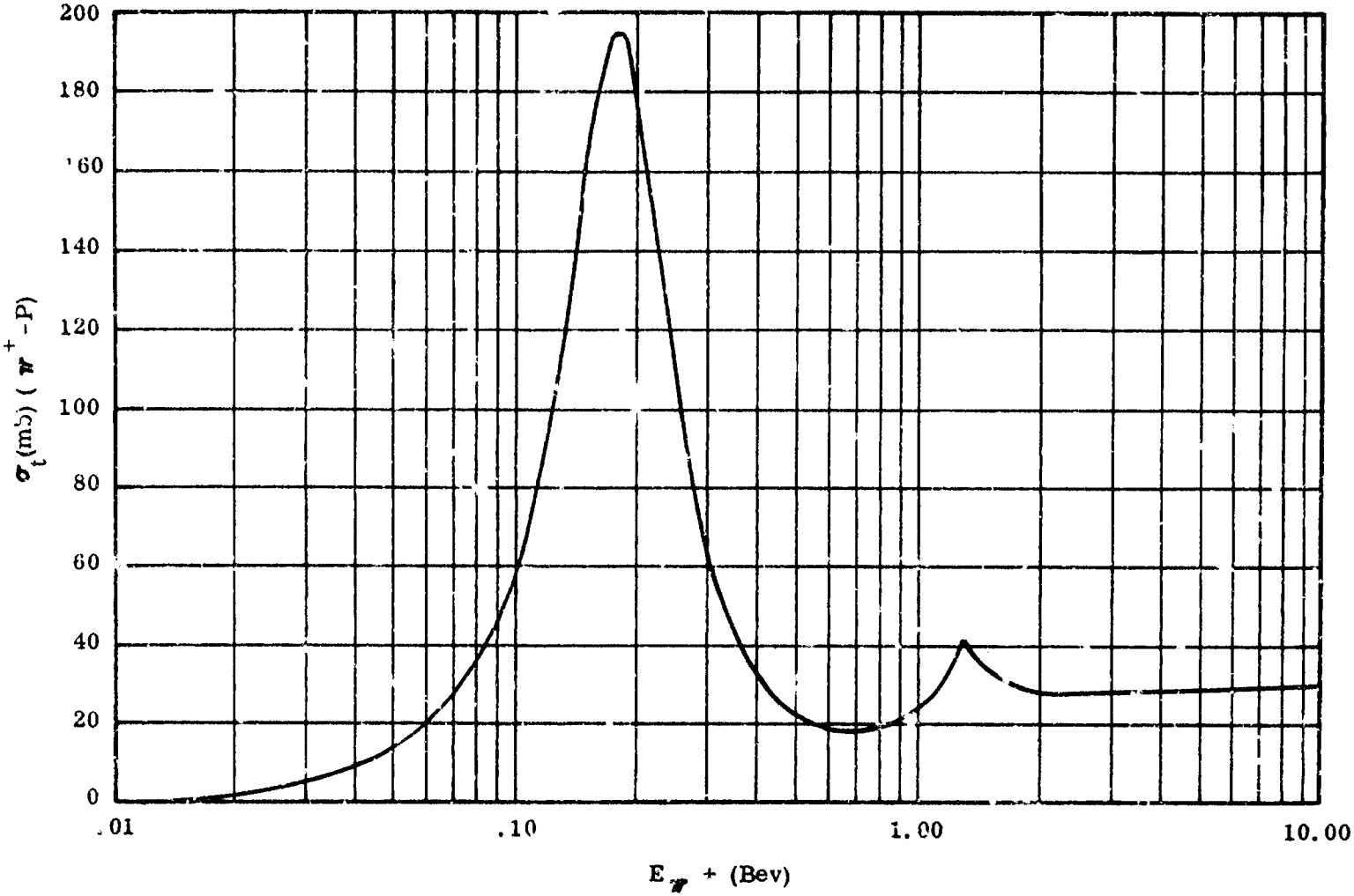

FIGURE 3-13 π^+-P TOTAL CROSS SECTIONS

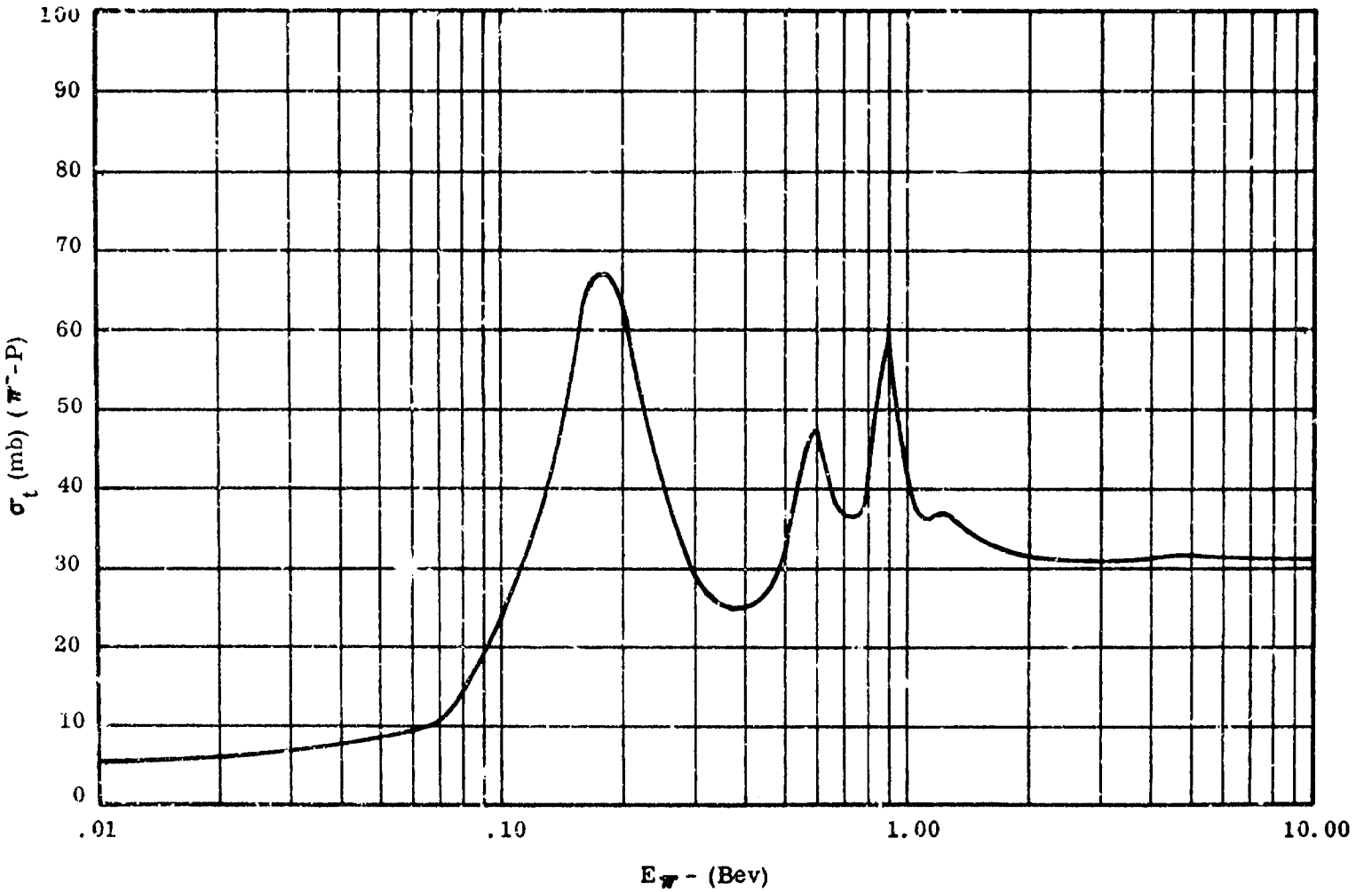

FIGURE 3-14 π^--P TOTAL CROSS SECTIONS

of 190 Mev, has been extensively discussed in the book by Bethe and de Hoffman[B9].

It will be observed that the π^--p cross section is almost exactly one third the π^+-p cross section at this resonance. For the negative pions, the ratios of elastic scattering to charge exchange scattering to radiative capture are 9:1:2. Only elastic scattering is allowed for the positive pions; the angular distribution of the elastic scattering in the center-of-mass system is of the form $1 + 3\cos^2\theta$. At other than the first resonance, the angular distribution is more complex and the interaction cross sections do not have such simple ratios. Considerations of charge symmetry and of charge independence of nuclear forces imply that the roles of positive and negative pions are reversed when neutrons are the target particles. For example, the cross sections for positive and negative pions are the same for deuteurium targets.

The measurement of pion-nucleon cross sections and of the energy and angular distribution of reaction products is an active field at present; the literature is correspondingly prolific and "transient" in the sense of improved values being generated. Earlier data are discussed in the book by Bethe and de Hoffman[B9]. A recent issue of Review of Modern Physics is devoted largely to pion data. *

When a pion interacts with a nucleus, considerations similar to those concerning nucleon-nucleus collisions result. In particular, optical model potentials have been derived and Monte Carlo calculations for high energy intra-nuclear cascades have been performed. In general, cross sections are of the same order of magnitude as those for incident nucleons, but there are differences in detail. A review article by Lindenbaum[L4] gives additional information.

---

* Review of Modern Physics 33, July 1961.

3.7 REFERENCES

Author	Key No.	Journal
Adelson, H. E.	A1	UCRL-8568, 12/58; Energy Spectra and Angular Dependences of Neutrons from the 31.5-Mev Proton Bombardment of Beryllium-9, Nitrogen-14, and Aluminum-27
Albert, R. D., et al	A2	Phys. Rev. 123, 1749, 1961, 10 Mev P^+ Reaction X-Sect.'s
Alekseeva, K. I., et al	A3	JETP (Russia) 35, 416, 1959; Inelastic Interaction between Cosmic Ray Protons of Kinetic Energy above 7 Bev. & Carbon & Hydrogen Nuclei (Exp't'l)
Allan, D. L.	A4	Proc. Phys. Soc. (London) A70, 195, 1957, N + Medium A $\rightarrow$ P^+, 14 Mev
Andrews, T. C., et al	A5	Bull. Am. Phys. Soc., Series III, 6, 342, 1961, P + P at 3.5 Bev
Ansel' M, A. A., et al	A6	JETP (Russia) 33, 377, 1957; On the Prod. of π Mesons by Protons on Nuclei of Various Elements. (Theory)
Armenteros, R., et al	A7	Phys. Rev. Let. (Abst.), Vol. 5, No. 2, 86, 1960; (P, P) X-Sect's at 1.9, 1.25, 2.0 Bev

REFERENCES (Continued)

Author	Key No.	Journal
Ashmore, A., et al	A8	Phys. Rev. Let. 5, No. 12, 577, Dec. '60, σ_t(P, P) 10-28 Gev/c
Ashmore, A., et al	A9	Proc. Phys. Soc. (London) A70, 745, '57; Nuclear σ_t for 350 Mev Neutrons
Atkinson, J. H., et al	A10	Phys. Rev. 123, 1850, 1961, 5 Bev. N X-sects in H & Other Elements
Azhgirei, L. S., et al	A11	JETP 33, 1185, 1957, & 6, 911, 1958; 675 Mev $P^+ \rightarrow$ Li, Be, C, & O
Bailey, L. E.	B1	UCRL-3334, 3/56; Angle and Energy Distributions of Charged Particles from the High-Energy Nuclear Bombardment of Various Elements
Baker, E. W., et al	B2	Phys. Rev. 123, 641, '61; 1., 2., 3. Bev P's on Ag & Br
Ball, W. P.	B3	UCRL-1938, 8/52; Nuclear Scattering of 300 Mev Neutrons (Thesis)
Barkas, W. H., et al	B4	Phys. Rev. 124, 1209, '61; Decay of Particles of Neg. Strangness

REFERENCES (Continued)

Author	Key No.	Journal
Barrett, P. H.	B5	Phys. Rev. 114, 1374; '59; Nuclear Absorption X-Sections for 3.6-Bev Neutrons
Benveniste, J., et al	B6	Phys. Rev. 101, 655, '56; σ_{ne} (P → Be) 31-Mev
Bennett, S., et al	B7	Phys. Rev. 124, 1982, '61; E Spectrum of μ's in Cosmic Air Showers
Berg, R. A., et al	B8	Phys. Rev. 101, 201, '56; Nuclear Surface Effects (Fermi Nuclear Component)
Bethe, H., et al	B9	Mesons & Fields, Row, Peterson & Co., White Plains, New York, June 1955
Beyster, J. R., et al	B10	LA 2099, 1957; Predictions of Fast Neutron Scattering Data with a Diffuse Surface Potential Well
Bjorklund, F., et al	B11	Paper - Exact Phase - Shift Calculation for Nucleon-Nuclear Scattering, 1958 New York Physical Society Meeting
Bjorklund, F., et al	B12	Paper - Exact Phase - Shift Calculation for Nucleon-Nuclear Scattering, 1958, Geneva
Bjorklund, F., et al	B13	Phys. Rev. 108, 795, '57; Analysis of Elastic Scattering and Polarization of 300 Mev Protons

REFERENCES (Continued)

Author	Key No.	Journal
Bjorklund, F., et al	B14	Phys. Rev. 109, '58; Optical Model Analysis of Scattering of 4.1-, 7-, & 14- Mev Neutrons by Complex Nuclei
Block, C.	B15	Phys. Rev. 93, 1094, '54; Theory of Nuclear Level Density
Blossei, H. G., et al	B16	Phys. Rev. 100, 1340, '55; (P, N) Reactions at 12 Mev, 20 Elements
Blue, M. H., et al	B17	Bull. Am. Phys. Soc., Series II, 6, 342, '61; P, P Collisions at 4.2 Bev
Booth, N. E., et al	B18	Proc. Phys. Soc. (London) A70, 209, '57; Nuclear X-Sect's 900 Mev P's
Bowen, P. H., et al	B19	Nuc. Phys. 22, 640, '61; Neutron Total Cross-Sections in the Energy Range 15 to 120 Mev
Bowen, T., et al	B20	Nuovo Cunento (10), 9, 908, '58; σ_a(1.5 Gev π^-) C, Fe, Pb., σ_a(2.8 Gev P) C, Fe, Pb.
Bratenahl, A., et al	B21	Phys. Rev. 77, '50; Elastic Scattering of 84-Mev Neutrons
Brenner, A. E., et al	B22	Phys. Rev. 106, 1020, '57; Cross Section Measurements Near 50 Bev

REFERENCES (Continued)

Author	Key No.	Journal
Britt, H. C., et al	B23	Phys. Rev. 124, 877, '61; α's & P's Emitted in the Bombardment of Au^{197} & Bi^{209}
Broek, H. W.	B24	Phys. Rev. 124, 233, '61; N^{o} Emission from Compound Nuclear Systems of High Ang. Momentum
Bumiller, F., et al	B25	Phys. Rev. 124, 1623, '61; Electromagnetic Form Factors of the Proton
Cence, R. J., et al	C1	Phys. Rev. 122, 1634, '61; Photo P's Produced by 245 ±15 Mev γ's on C
Chamberlain, O. et al	C2	Phys. Rev. 87, 81, '52; Proton-Proton Collisions Within Lithium Nuclei
Chen, F. F., et al	C3	Phys. Rev. 99, 857, '55; Attenuation Cross Sections for 860-Mev Protons
Ciocio, A., et al	C4	Phys. Rev. 124, 1201, '61; Absorption Mean Free Path of the Nucleonic Component of Cosmic Radiation
Clark, D. L.	C5	Phys. Rev. 87, 157, '52; Production of 40-Mev π^{+} and π^{-} Mesons by 240-Mev Protons

REFERENCES (Continued)

Author	Key No.	Journal
Cohen, B. L., et al	C6	Phys. Rev. 111, 1568, '58; Further Studies of Anomalous Inelastic Proton Scattering
Cohen, B. L., et al	C7	Phys. Rev. 113, 579, '59; σ_{ne} (P → Med. Weight Elem
Cohen, B. L.	C8	Phys. Rev. 108, 768, '57; Coincidence Studies of the Ni^{58} (P, 2P) Reaction
Cohen, B. L., et al	C9	Phys. Rev. 106, 995, '57; Inelastic Proton Scattering and (P, d) Reactions in Heavy Elements
Cohen, B. L.	C10	Phys. Rev. 105, 1549, '57; Anomalous Scattering of 23-Mev Protons by Heavy Elements
Comfett, H. E.	C11	Phys. Rev. 105, 1324, '57; σ_{ne} (12 Mev P's) on Li, C, Mg, & Si
Cook, T., et al	C12	Phys. Rev. 98, 1369, '55; Nuclear X-Sect's 1.4 Bev N^{O}
Cool., V., et al	C13	Phys. Rev. 125, 320, '61; K^{-} + P X-Sect's 1-4 Bev/c
Crandall, W. E., et al	C14	Phys. Rev. 101, 329, '56; C^{12} (x, xn) C^{11} & Al^{27} (x, x2PN)Ni^{24} X-Sect's, High E

REFERENCES (Continued)

Author	Key No.	Journal
Crandall, W. E., et al	C15	Phys. Rev. [illegible], 749, '53; P + C → π^0 + X (Characteristics)
Critchfe'd, C. L. et al	C16	Phys. Rev. 82, 243, '51; The Density of States in Light Nuclei, Q < 25 Mev
Day, R. B., et al	D1	Phys. Rev. 92, 358, '53; Neutron σ_t at 20 Mev
Deahl, J., et al	D2	Phys. Rev. 124, 1987, '61; π^- - P Interaction at 224 Mev
de Carralho, H. G.	D3	Phys. Rev. 96, 398, '54; σ_t (208 & 315 Mev P's Light Elements)
de Juren, J.	D4	Phys. Rev. 80, 27, '50; Nuclear X-Sections for 270 Mev Neutrons
de Juren, J., et al	D5	Phys. Rev. 77, 606, '50; Nuclear X-Sect's for 95 Mev Neutrons
Denisenko, G. F., et al	D6	Phys. Rev. 109, 1779, '58; Fission of Chromium, Silver, and Bromine Nuclei with High Energy Particles
Devlin, T. J.	D7	UCRL-9548, 3/61; $\sigma_t(\pi^\pm$ + P) 450 Mev - 1650 Mev

REFERENCES (Continued)

Author	Key No.	Journal
Diddens, A. N., et al	D8	Phys. Rev. Let., Vol. 9, No. 1, 32, '62; High E σ_t(N+N)
Dostrovsky, I., et al	D9	Phys. Rev. 116, 683, '59; M.C Calculations of Nuclear Evap. Processes III Application to Low Energy Reactions
Dostrovsky, I., et al	D10	Phys. Rev. 111, 1659, '58; M.C. Calculations of High E Nuclear Interactions, I. Systematics of Nuclear Evaporation
Dostrovsky, I., et al	D11	Phys. Rev. 123, 1452, '61; Formation of N^{13} in High-E Nuclear Reactions
Dzhelepov, V. P., et al	D12	Doklady Akad. Nauk, CCCP 104, 717, '55; σ_t for 380-, 500-, 590-, 630-Mev Neutrons (In Russian)
Eisberg, R. M., et al	E1	Phys. Rev. 100, 1309, '55; α's (40 Mev) + Au, Ag, & Cu → P's
Eisberg, R. M., et al	E2	Phys. Rev. 93, 1039, '54; σ_{ne}(31 Mev P's) from Heavy Elements
Eliott, T., et al	E3	Phys. Rev. Let. Vol 3, No. 6, 285, 9/59; $\sigma(\overline{P}, P)$ 534-1068 Mev.
Fernbach, S., et al	F1	Phys. Rev. 75, 1352, '49; The Scattering of High E N^0 by Nuclei

REFERENCES (Continued)

Author	Key No.	Journal
Feshbach, H., et al	F2	Phys. Rev. 96, 448, '54; Model for Nuclear Reactions with N^O's (cloudy crystal ball)
Feshbach, H.	F3	Ann. Rev. Nuc. Sci. 8, 49, '58; The Optical Model and Its Justification
Fox, R., et al	F4	Phys. Rev. 80, 23, '50; σ_t of Nuclei for 280 Mev Neutrons
Gell-Mann, M., et al	G1	Ann. Rev. Nuc. Sci. 7, '57; Hyperous and Heavy Mesons (Systematics & Decay)
Gell-Mann, M., et al	G2	Sci. Am. 7/57; Elementary Particles
Glasser, R. G., et al	G3	Phys. Rev. 123, 1014, '61: Mean Lifetime of the π^O
Goldberger, M. L.	G4	Phys. Rev. 74, 1269, 1948, The Interaction of High Energy Neutrons and Heavy Nuclei
Good, R. H., et al	G5	Phys. Rev. 124, 1223, '61; Regeneration of K^O's & Their Mass Difference
Gouding, T. J., et al	G6	I. Exp. Nuc. Phys. 18, 46, '60; Quasi-Elastic P-State Scattering of 153 Mev Protons in C^{12}
Gouding, T. J., et al	G7	Nuc. Phys. 12, 241, '59; P Total Reaction X-Section at 34 Mev

REFERENCES (Continued)

Author	Key No.	Journal
Greenberg, O. W., et al	G8	Phys. Rev. 124, 2047, '61; Limit on High E X-Section from Analyticity in Lehnian Ellipses
Griffiths, R. J., et al	G9	Nuc. Phys. 12, 225, '59; The Mechanism of the Direct Interaction Process at Intermediate Energies
Gross, E.	G10	UCRL-3330, 3/56; The Absolute Yield of Low Energy Neutrons from 190-Mev Proton Bombardment of Gold, Silver, Nickel, Aluminum, and Carbon
Gugelot, P. C.	G11	Phys. Rev. 93, 425, '54; Level Densities of Nuclei from the Inelastic Scattering of 18-Mev Protons
Haling, R. K., et al	H1	Phys. Rev. 106, 971, '57; Study of Al^{27} (N, P)Mg^{27} at 14 Mev
Halliday, D.	H2	"Introductory Nuclear Physics", John Wiley and Sons, Inc., 1955
Hausei, W., et al	H3	Phys. Rev. 87, 366, '52; Inelastic Scattering of Neutrons
Hess, W. N., et al	H4	Phys. Rev. 101, 337, '56; Prod. of H^2's in High E N Bombardment & Its Bearing on Nuclear Charge Distribution

REFERENCES (Continued)

Author	Key No.	Journal
Hess, W. N.	H5	Rev. Mod. Phys. 30, 368, '58; Summary of High E Nucleon-Nucleon X-Section Data
Hicks, D. A.	H6	MTA-28, Dec. '52, Livermore Research Laboratory, California Research & Development Co., Total Attenuation Cross-Sections for High Energy Protons
Hildebrand, R. H.	H7	UCRL-1159, 3/51; Elastic Scattering of 83 Mev Neutrons
Hildebrand, R. H., et al	H8	Phys. Rev. 80, 842, '50; σ_t for 42 Mev Neutrons
Hildebrand, R. H., et al	H9	UCRL-1305, 5/51, Summary of Neutron Cross-Section Measurements of 14 Mev to 280 Mev Neutrons
Hornyak, W. F., et al	H10	Phys. Rev. 100, 1409, '55; Inelastic Scattering of 19-Mev Protons by O^{16}
Hughes, D. J., et al	H11	BNL-400, June 1956; Neutron Cross Sections - Angular Distributions
Hughes, D. J., et al	H12	Report ENL 325, Neutron Cross Sections
Hull, M. H., Jr., et al	H13	Phys. Rev. 122, 1606, '61; Phase-Parameter Representation of Neutron-Proton Scattering, 13.7-350 Mev

REFERENCES (Continued)

Author	Key No.	Journal
Iizuka, J., et al	I1	Phys. Rev. 123, 669, '61; Theory of a Single Pion Production $P^+ - P^+$ Collisions
Jackson, J. D.	J1	The Physics of Elementary Particles, Princeton Univ. Press, '58
Jain, P. L.	J2	Phys. Rev. 122, 1890, '61; Angular Distribution of Shower Particles from 1000 Bev/Nucleon Alpha Particles on Emulsion Nuclei
Kenney, R. W., et al	K1	Phys. Rev. 122, 1631, 161; Photo Prod. of Mesons from Hydrogen & Deuterium
Kim, C. Y., et al	K2	Phys. Rev. 122, 1641, '61; Single Scattering of 2 Bev/c Muons in Nuclear Emulsions
Kiselev, V. S., et al	K3	JETP (Russia) 35, 546, '59, New Measurements of the Neutron Spectrum in the Bombardment of Be by 680 Mev Protons (Exp't'l)
Klepikov, N. P., et al	K4	Laboratory of Theoretical Phys., D-584, Doubna, Russia, '60; $\sigma_t(\pi^{\pm} - P)$ 0-50 Bev
Kopp, J. K., et al	K5	Phys. Rev. 123, 301, '61; $\pi^+ - P$ Scattering at 990 Mev

REFERENCES (Continued)

Author	Key No.	Journal
Kostanashvilli, N. I., et al	K6	JETP 9, 713, '59; Prod. of Strange Particles in the Interaction Between 9-Bev Protons and Emulsion Nuclei
Kurath, D.	K7	Phys. Rev. 101. 216, '56; Intermediate Coupling in the I-P Shell
Kurzunoglu, B.	K8	Phys. Rev. 105, 1846, '57; Proton Bremsstrahlung
Lamarsh, J. P., et al	L1	Phys. Rev. 104, 1633, '56; Direct Interaction in Neutron Inelastic Scattering
Landau, L. D., et al	L2	Statistical Physics, Addison-Wesley Pub. Co., Reading, Mass., '58
Lee, T. D., et al	L3	BNL-443 (T-91), 10/57, Elementary Particles & Weak Interactions
Lindenbaum, S. J.	L4	Ann. Rev. Nuc. Sci. 7, 317, 1957; Collisions of Particles Below 1 Bev with Nuclei
Linnor, W. I., et al	L5	Phys. Rev. 92, 835, '53; Neutron σ_t for Bi & U, 45-160 Mev
Lock, W. O.	L6	High Energy Physics, John Wiley & Sons, New York, 1960

REFERENCES (Continued)

Author	Key No.	Journal
Lohrman, E.	L7	Phys. Rev. 122, 1908, '61; Investigation of Bremsstrahlung & Pair Prod. at E > 10^{11} ev
Longo, M. J.	L8	UCRL-3497, '61; Nucleon & Nuclear X-Sections for Positive Pions & Protons Above 1.4 Bev/c
Louttit, R. I., et al	L9	Phys. Rev. 123, 1465, '61; Prod. of Strange Particles in P-P Collisions at 2.85 Bev
Lukianov, A. V., et al	L10	JETP (Russia) 35, 521, '59; Optical Model for the Interaction of Neutrons of Intermediate Energy with Nuclei (Theory)
McCarthy, I. E., et al	Mc1	Nuc. Phys. 12, 274, '59; Momentum Dist. of Nucleons in the Nuclear Surface
MacGregor, M., et al	Mc2	Phys. Rev. 108, 726, '56; Nonelastic Neutron X-Sect's at 14 Mev.
Macgregor, M. H., et al	Mc3	Proc. 2nd U. N. Int. Conf. on the Peaceful Uses of Atomic Energy, Paper P/1881, Vol. 14, p. 109, "Neutron X-Sect Measurements Pertaining to the Optical Model"

REFERENCES (Continued)

Author	Key No.	Journal
MacGregor, M. H., et al	Mc4	Phys. Rev. 111, 1155, '58; Neutron Nonelastic Cross Sections at 21.0, 25.5, & 29.2 Mev
Maglic', B. C., et al	M1	Phys. Rev. 123, 1444, '61; Ang. Dist. of P's from π^- - P Scattering (900 Mev)
Maloy, J. O., et al	M2	Phys. Rev. 122, 1338, '61; Polarization of the Recoil from π^0 Photo Production in Hydrogen
Maris, Th. A. J., et al	M3	Nuc. Phys. 7, 1, '59; Quasi Elastic Scattering & Nuclear Structure
Marquit, E.	M4	Polish Acad. of Sciences, Inst. of Nuc. Research, Rpt. No. 255/VI, 6/61; σ_e(P-P) 1.5-9.0 Bev
Marshak, R. E.	M5	Meson Physics, McGraw-Hill, 1952
Marshall, J., et al	M6	Phys Rev. 91, 767, '53; σ_t of 408 Mev Protons for Hydrogen and Light Elements
Metropolis, N. R.	M7	Phys. Rev. 110, 204, 1958; Monte Carlo Calculations on Intranuclear Cascades, II, High Energy Studies and Pion Processes.

REFERENCES (Continued)

Author	Key No.	Journal
Meyer, V., et al	M8	Phys. Rev. 117, 1334, '60; Total Reaction Cross Sections of Several Nuclei for 61-Mev Protons
Miller, O. M., et al	M9	Ann. Rev. Nuc. Sci. 9, 159, 1959, High Energy Nuclear Reactions
Nedzel, V. A.	N1	Phys. Rev. 94, 174, '54; σ_t for 410 Mev Neutrons, H, D, Be, C, O, Al, S, Cl, Fe, Cu, Cd, Pb, U
Neville, D. E	N2	Phys. Rev. 124, 2037, '61; Radiative Modes of K-Meson Leptonic Decay
Nishimura, K., et al	N3	Nuc. Phys. 7, 425, '58; Inelastic Scattering of 96 Mev Protons
Nordin, P., Jr.	N4	Phys. Rev. 123, 2168, '61; S- & P-Wave Interactions of K-Mesons in H
Okun', L.	O1	Ann. Rev. Nuc. Sci. 9, '59; Strange Particles - Decays
Ostroumov, V. I., et al	O2	JETP 9, 254, 59; Cascade α-Particles in Stars Produced by 360 & 660 Mev Protons
Pate, B. D., et al	P1	Phys. Rev. 123, 647, '61; Spaliation of U & Th. Nuclei with Bev E P's

REFERENCES (Continued)

Author	Key No.	Journal
Peck, R. A., Jr.	P2	Phys. Rev. 106, 965, '57; (n, p) Reaction for Au, Ei=14 Mev
Peele, R. W.	P3	Phys. Rev. 105, 1311, '57; Diff. X-Sect's for the Scattering of Med. Energy Protons on Carbon 14-19.4 Mev
Prokoshkin, Iu. D., et al	P4	JETP 6, 245, '58; Prod. of π^0's in Various Nuclei by 260-660 Mev P's
Richardson, R. E., et al	R1	Phys. Rev. 86, 29, '52; Nuclear Elastic Scattering of High E P's
Riley, K. F., et al	R2	Nuc. Phys. 18, 65, '60; Quasi Elastic Scattering of 153 Mev Protons by P-State Protons in C^{12}. II. Theoretical
Rosenzweig, N.	R3	Phys. Rev. 108, 817, '57; Influence of Shell Structures on the Level Density of a Highly Excited Nucleus
Rosenzweig, N., et al	R4	Proc. of the 2nd International Conf. on Peaceful Uses of Atomic Energy, Paper P/693, Vol. 14, p 58; An Effect of Shell Structure in the Level Density of Highly Excited Nuclei
Ross, A. A.	R5	Phys. Rev. 108, 720, '57; Nuclear Level Densities
Rossi, B.	R6	High-Energy Particles, Printice-Hall, Inc., 1952

REFERENCES (Continued)

Author	Key No.	Journal
Rudstam, G., et al	R7	Phys. Rev. 87, 358, '52; Nuclear Reactions of Fe with 340 Mev P's
Rudstam, G., et al	R8	Phys. Rev. 126, 1852 (1962); Spallation of Copper with 24-Gev Protons
Salmon, G. L.	S1	Nuc. Phys. 21, 15, '60; The Elastic Scattering of 96 Mev Neutrons by Nuclei
Schult, R. L., et al	S2	Phys. Rev. 122, 1659, '61; K^--D Absorption & a π - Σ Resonance
Schweber, S. S., et al	S3	Mesons & Fields, Volume II, Row, Peterson and Company, 1955
Serber, R.	S4	Phys. Rev. 72, 1114, '47; Nuclear Reactions at High Energies
Shapiro, A. M.	S5	Rev. of Mod. Phys. 28, 4/56; Table of Properties of "Elementary" Particles
Sherr, R., et al	S6	Phys. Rev. 124, 1928, '61; Spectra of (P, α) & (P, P) Reactions & the Evaporation Model
Shwe, H., et al	S7	Phys. Rev. Let. 7, #11. (Abst 16) '61; Decay of π^0's

REFEPENCES (Continued)

Author	Key No.	Journal
Sternheimer, R. M., et al	S8	Phys. Pev. 123, 333, '61; Extension of the Isobaric Nuclear Model for π Prod. in π-N, N-N, & $\bar{N}$-N Interactions
Strauch, K., et al	S9	Phys. Rev. 104, 191, '56; Inelastic Scattering of 96-Mev Protons
Sakurai, J. J.	S10	Phys. Rev. Let. 1, 40, '58; Paper
Summers-Gill, R. G.	S11	Phys. Rev. 109, 1591, '58; Scattering of 12 Mev P's, 24 Mev D's, 48 Mev α's by Be
Taylor, A. E., et al	T1	Nuc. Phys. 25, 642, '61; Proton Scattering from Light Elements at 142 Mev
Terrell, J.	T2	Phys. Rev. 113, 527, '59; Fission Neutron Spectra & Nuclear Temperatures
Tsao, C. H., et al	T3	Bull. Am. Phys. Soc., Series II, 6, 343, 61; Scattering of 5.1 Bev Protons in Nuclear Emulsion
Tyren, H., et al	T4	Nuc. Phys. 6, 446, '58; Inelastic Scattering of 185 Mev Protons on Nuclei with Masses from Fluorine to Potassium
Tyren, H., et al	T5	Nuc. Phys. 7, 10, '58 High E (P,2P) Reactions & P Binding E's

REFERENCES (Continued)

Author	Key No.	Journal
Tyren, H., et al	T6	Nuc. Phys. 4, 637, '57, Inelastic Scattering of 185 Mev Protons on Oxygen, Calcium, & Carbon
Tyren, H., et al	T7	Nuc. Phys. 7, 24, '58; Inelastic Scattering of 185 Mev Protons on Elements Between Ca and Zn
Tyren, H., et al	T8	Nuc. Phys. 6, 82, '58; Inelastic Scattering of 185 Mev Protons on Lithium, Beryllium, Boron, and Nitrogen
Unseren, E., et al	U1	Phys. Rev. 122, 1875, '61; Excitation Functions of the (P, 2P 6N) & (P, 3P 5N) Reactions for 60-, 100-. 150-, and 840 Mev Protons on Enriched Zirconium-90
Van Loef, J. J., et al	V1	Phys. Rev. 101, 103, '56; Measurements of Inelastic Scattering X-Sections for Fast Neutrons. $E_n < 10$ Mev
Ware, W. R., et al	W1	Phys. Rev. 122, 1837, '61; Excitation Functions of the (P, P N) & (P, 2P) Reactions in Ce^{142} at 60-233 Mev
Wattenberg, A., et al	W2	Phys. Rev. 104, 1710, '56, Momentum of Nucleons in Various Nuclei from the High Energy Photo Effect
Weinberg, S.	W3	Phys. Rev. 121, 2049, '61; X-Sections at High Energies

REFERENCES (Continued)

Author	Key No.	Journal
Weisskopf, V. F.	W4	Proc. of the 2nd U. N. Conf. on Peaceful Uses of Atomic Energy, Paper 2599, Vol. 14, Page 3; The Properties of Nuclear Matter
Winsberg, L., et al	W5	Phys. Rev. 122, 1623, '61; Direct Nucleon-Nucleon Collisions Inside the Nucleus According to the Impulse Approximation
Xuong, N., et al	X1	Phys. Rev. 124, 575, '61; Antiproton-Proton Inelastic Interactions at 1.61 Bev/c and Their Use for a Test of Charge-Conjugation Invariance in Strong Interactions
Zerby, C. D.	Z1	Phys. Rev. 124, 2029, '61; Electromagnetic Prod. of Pion Pairs
Zinov, V. G., et al	Z2	JETP (Russia) 33, 335, '57, The Elastic Scattering of 307 Mev π^--Mesons from Hydrogen

BLANK PAGE

4.0 RADIATION PENETRATION CODES

4.1 ELECTRON BREMSSTRAHLUNG

The trapped radiation belts girdling the earth contain electrons whose origins probably include the decay of neutrons from cosmic ray interactions and, possibly, injection along the solar magnetic lines. The belts are generally subdivided into an inner and an outer belt. The mapping of these belts is in a preliminary stage so that approximate flux contours must be relied on at present for radiation studies. The energy spectrum of electrons in both belts, as inferred from measurements at low altitudes, is given in NR-140[9]*, page 108. The spectrum of the outer belt has been revised as a result of measurements by instruments aboard Explorer XII[1].

The revised outer belt energy spectrum gives considerably more importance to higher energies than do previous estimates. The integral energy flux above 40 Kev is several orders of magnitude lower and the high energy cut-off is raised from about 1 Mev to about 5 Mev. A revised integral spectrum which is consistent with the Explorer XII data is shown in Figure 4-1.

The calculations of the electron bremsstrahlung dose produced by the revised spectrum is more difficult, for a number of reasons. The Lockheed Electron Bremsstrahlung Code (LEBC) presently in use is designed to treat electrons which are stopped in low z elements. A rather conservative model is used in that the electrons are incident perpendicularly on the slab and photons generated by the bremsstrahlung process are assumed to continue straight ahead along the normal. Electrons are stopped in one layer and gamma radiation is assumed to be generated at the next boundary and to be attenuated through the following layers of material. This model is valid for low energies because the electrons are stopped

---

* References are listed at end of section.

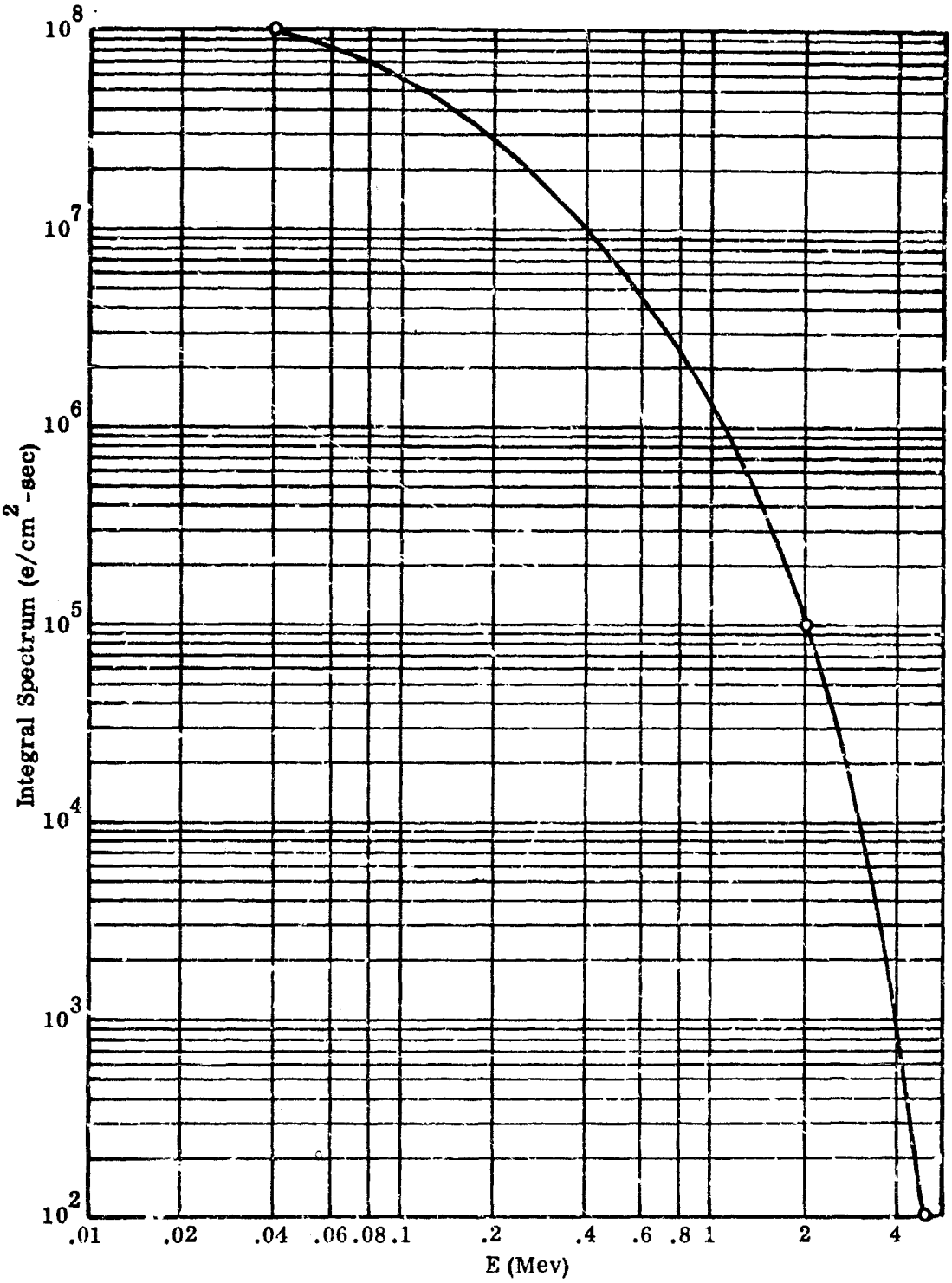

FIGURE 4-1 INTEGRAL ELECTRON SPECTRUM IN THE OUTER TRAPPED BELT

in the first few tenths of a gram per square centimeter of shield and the gamma rays are produced in this thin layer. However, some electrons in the revised spectrum may penetrate five gm/cm^2 of shield, leading to an inaccuracy because of the relatively large width of the layers.

This code treats the radiative energy losses as being negligible in the slowing down process, even though a small fraction of electrons lose a large part of their energy in a single collision. This condition is not met for high energy electrons in heavy elements. For example, 6.9 Mev electrons in lead lose half their energy in radiative collisions. This effect causes an overestimate of photon production.

The bremsstrahlung cross section used in the code is a Born approximation given by Formula 3BN in a review article by Koch and Motz[2]. This approximate formula is not designed for heavy elements and low electron energies, but it is expected to be accurate within a factor of two for the worst cases in the region of interest.

The initial spectrum of the secondary photons is given by the code. It is possible to perform a spectrum weighted dose buildup calculation with the aid of a table of gamma ray dose buildup factors[7]. This correction has been incorporated into the results given below.

Despite the approximations of the model, it is instructive to use it to make preliminary estimates of the bremsstrahlung dose penetrating a shield. The results should be accurate within a factor of five for shields ranging in thickness from 10 to 50 gm/cm^2. It is probable that the dose estimates are high due to the straight ahead nature of the calculation.

The trajectory listed in NR-140, page 120, for a typical circumlunar mission was reanalyzed with improved data. The integrated proton and electron fluxes are 1.5×10^6 p/cm^2 and 4.3×10^9 e/cm^2 respectively. The energy spectrum of Figure 4-1 is used for both inner and outer belt electrons, and the Freden-White spectrum is used for the inner belt protons. Materials

examined include water, carbon, aluminum, iron, cesium, and tungsten. Shield thicknesses range from 10 gm/cm^2 to 50 gm/cm^2. The results are shown in Figures 4-2 and 4-3. In all cases, it is found that the proton dose, including secondaries, is a factor of 10^2 to 10^4 greater than the electron bremsstrahlung dose. It appears that more elaborate calculations of dose due to electrons are needed only for shields thinner than 10 gm/cm^2 and for orbiting missions within the radiation belts.

4.2 PROTON PENETRATION CALCULATIONS

The Lockheed Proton Penetration Code (LPPC) is an IBM-7090 program which calculates primary and secondary doses behind multistrata slabs due to an incident proton flux. A number of options are available to treat special cases of interest. Since the code and input data have been described in a previous report[9], only a brief description will be given here. New features will be described in more detail.

The code treats protons incident monodirectionally along the shield normal, or an isotropic proton flux incident on the shield. The treatment of the isotropic flux, a newly added feature, is described in Section 4.5.

Four options are available to describe the energy distribution of the incident flux. Option 1 computes the differential energy spectrum from the power law given in Equation 4-1. Option 2 computes the differential energy spectrum from an exponential form given in Equation 4-2.

$$\Phi(E) = A \cdot E^{-B} \qquad 4\text{-}1$$

$$\Phi(E) = A \cdot \mathrm{Exp}(-B \cdot E) \qquad 4\text{-}2$$

A and B are input constants and E is energy. Low energy and high energy cutoffs may be applied to spectrum Options 1 and 2.

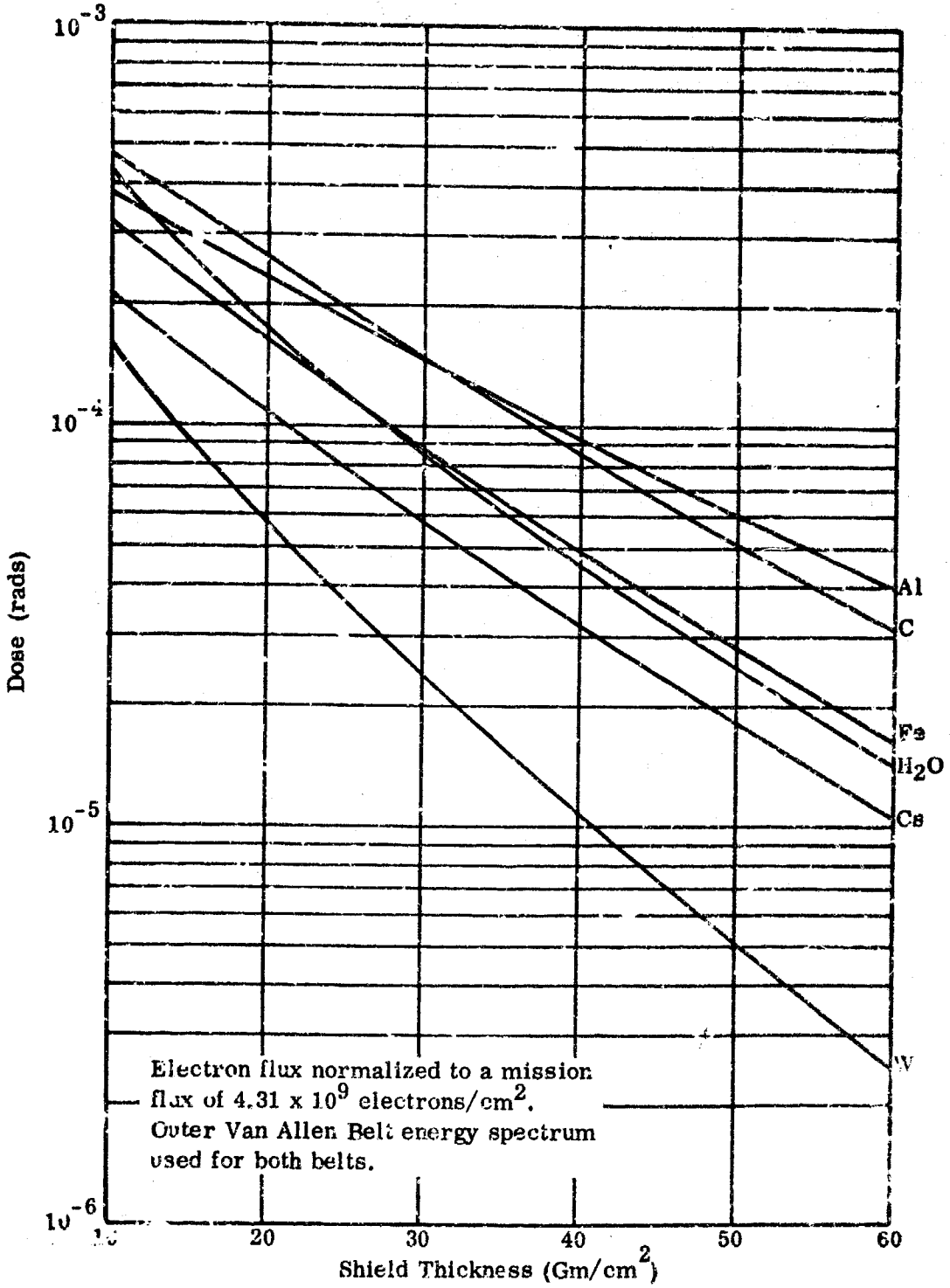

FIGURE 4-2 ELECTRON BREMSSTRAHLUNG DOSE VS THICKNESS FOR A TYPICAL TRAJECTORY THROUGH THE VAN ALLEN RADIATION BELTS

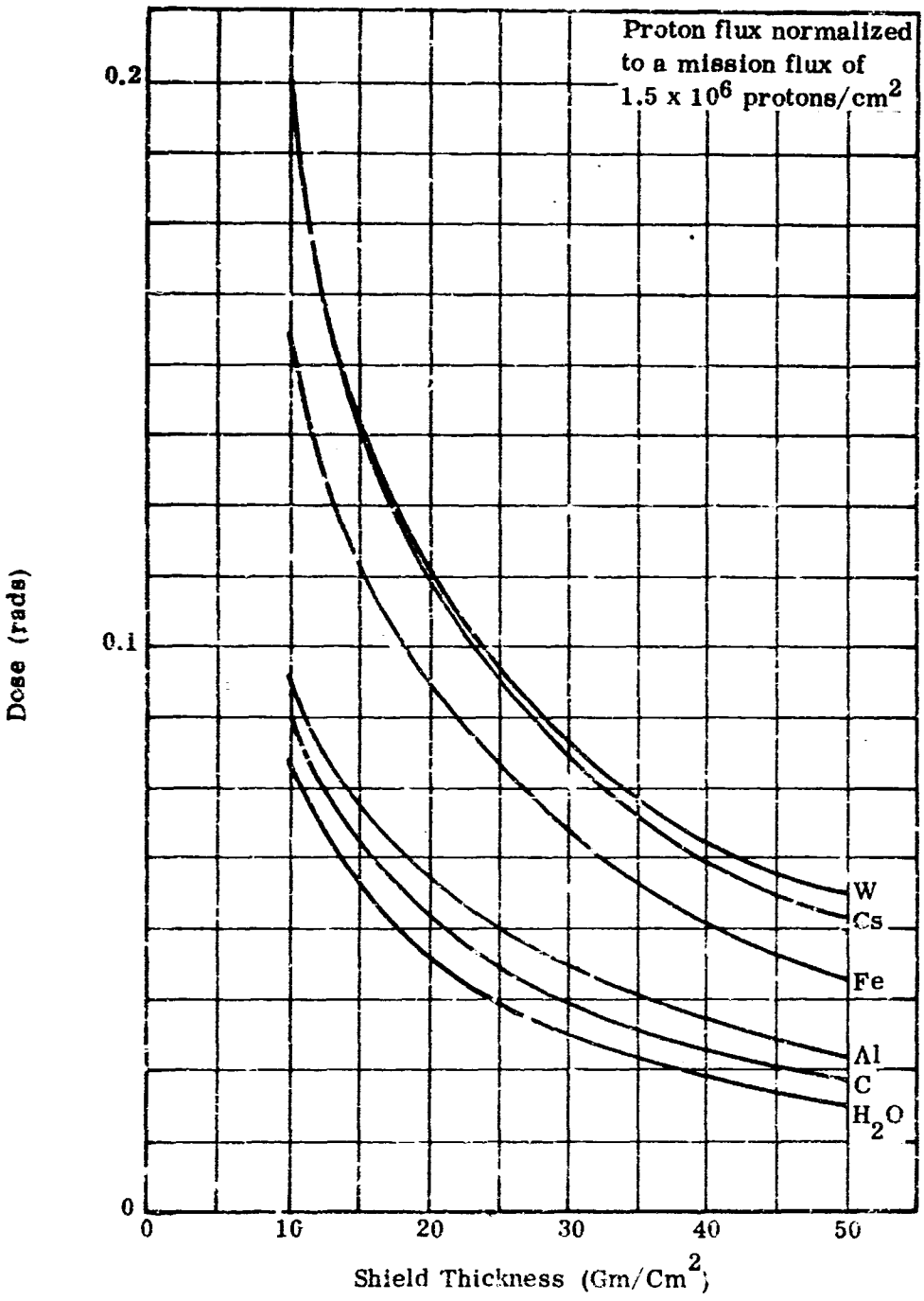

FIGURE 4-3 PROTON DOSE VS THICKNESS FOR A TYPICAL TRAJECTORY THRU THE INNER VAN ALLEN RADIATION BELT

Option 3 reads a table of the differential energy flux versus energy. A linear interpolation routine automatically computes the flux at the energy mesh points used in the calculation. Spectrum options 1, 2, and 3 treat a continuous differential energy spectrum.

Option 4 treats a monoenergetic spectrum. The monoenergetic option, a new feature, is discussed in Section 4.4.

The code treats a slab shield composed of one to ten homogeneous strata. Each stratum may contain a single element or compound, or may be built from five or fewer materials for which data are available in the library. The library at present contains data for nine elements (H, Be, C, N, O, Al, Fe, Cs, W) and several hydrogenous compounds. Each stratum may be further subdivided into a number of layers. The total number of layers in a shield may be as great as one hundred.

Each dose component and the total dose are computed at zero thickness and after each layer. This computation, when used in conjunction with the multistrata capability of the code, permits an estimation of dose versus depth in the receiver material simply by treating the receiver material as an additional stratum. The calculation is slightly inaccurate since the evaporation neutrons generated at a given layer in the receiver do not contribute to the evaporation neutron dose at layers closer to the incident face. This error is negligible in nearly all cases.

The input proton spectrum may be printed out, if desired. For the case of protons incident along the shield normal, the primary and cascade nucleon spectra may be output after each layer. The spectrum printout option is not made available for the isotropic case due to the large volume of data involved.

The code calculates the spectrum of primary and cascade nucleons after each layer by employing a solution to a pair of coupled, integro-differential equations, represented by Equations 4-3 and 4-4.

$$\frac{\partial \Phi_P(E,X)}{\partial X} + \Sigma_P(E) \cdot \Phi_P(E,X) = \frac{\partial \left[\Phi_P(E,X) \cdot S(E) \right]}{\partial E} + \Phi_{PP}(E,X) + \Phi_{NP}(E,X) \quad 4\text{-}3$$

$$\frac{\partial \Phi_N(E,X)}{\partial X} + \Sigma_N(E) \cdot \Phi_N(E,X) = \Phi_{PN}(E,X) + \Phi_{NN}(E,X) \quad 4\text{-}4$$

$\Phi_P(E,X)$ = primary plus secondary proton differential energy flux. The code actually treats each component separately.

$\Phi_N(E,X)$ = cascade neutron flux.

E = energy.

X = position in shield.

$\Sigma_P(E)$, $\Sigma_N(E)$ = inelastic cross section for protons (neutrons).

$S(E) = \frac{dE}{dX}$, proton stopping power.

$\Phi_{AB}(E,X)$ = cascade production term, or particles of type B produced by particles of type A in the shield layer.

Solutions to Equations 4-3 and 4-4 are given by Equations 4-5 and 4-6.

$$\Phi_P(E, X + \Delta X) = \Phi_P(E', X) \frac{S(E')}{S(E)} \mathrm{Exp}\left[-y(E') + y(E)\right] + \Phi_{PP}(E,X) + \Phi_{NP}(E,X) \quad 4\text{-}5$$

$$\Phi_N(E, X + \Delta X) = \Phi_N(E,X) \mathrm{Exp}\left[-\Sigma_N(E) \cdot \Delta X\right] + \Phi_{PN}(E,X) + \Phi_{NN}(E,X) \quad 4\text{-}6$$

where ΔX = layer thickness, and E' is defined in terms of the range, $R(E)$.

$$R(E') = R(E) + \Delta X \tag{4-7}$$

The terms in the exponent of Equation 4-5 are defined in Equation 4-8.

$$y(E) = \int_0^E \frac{\Sigma_P(E'')}{S(E'')}\, dE'' \tag{4-8}$$

The production terms, $\Phi_{AB}(E, X)$, are given in Equations 4-9 through 4-12.

$$\Phi_{PP}(E, X + \Delta X) =$$

$$\int_X^{X+\Delta X} \left[\int_{E'}^{\infty} \Phi_P(E_I, x) \cdot \Sigma_P(E_I) \cdot \tau_{PP}(E_I, E_S) dE_I \right] \frac{S(E_S)}{S(E_I)}\, dx \tag{4-9}$$

$$\Phi_{NP}(E, X + \Delta X) =$$

$$\int_X^{X+\Delta X} \left[\int_{E_S}^{\infty} \Phi_N(E_I, x) \cdot \Sigma_N(E_I) \cdot \tau_{NP}(E_I, E_S) dE_I \right] \frac{S(E_S)}{S(E_I)}\, dx \tag{4-10}$$

$$\Phi_{PN}(E, X + \Delta X) =$$

$$\int_X^{X+\Delta X} \left[\int_{E}^{\infty} \Phi_P(E_I, x) \cdot \Sigma_P(E_I) \cdot \tau_{PN}(E_I, E_S) dE_I \right] dx \tag{4-11}$$

$$\Phi_{NN}(E, X + \Delta X) =$$

$$\int_X^{X+\Delta X} \left[\int_{E}^{\infty} \Phi_N(E_I, x) \cdot \Sigma_N(E_I) \cdot \tau_{NN}(E_I, E_S) dE_I \right] dx \tag{4-12}$$

Where E_I = energy of incident particle suffering an inelastic collision at x, $X \leq x \leq X + \Delta X$

E_S = energy of secondary particle emerging from inelastic collision

$\tau_{AB}(E_I, E_S)$ = number of secondary particles of type B per unit energy at E_S resulting from the inelastic collision of a particle of type A with energy E_I.

The reduction of the above equations to tractable form is given in NR-140[9], pages 58-65. The cascade nucleon sources are distributed realistically through the layer. The flux of particles available for producing inelastic collisions is assumed to be unaffected by nuclear collisions within the layer. The flux of cascade particles generated throughout a layer is also assumed to be unaffected by nuclear collisions within the layer. These approximations are valid as the layer thickness is usually only a few percent of an inelastic mean free path. The effect of energy losses due to ionization inside the layer is taken into account, both for proton initiated reactions and for cascade protons produced in the layer. Both nuclear attenuation and ionization losses of particles incident on the layer are considered in calculating attenuation within the layer.

It is assumed that the yield of secondary nucleons is nearly constant over a range of energies corresponding to slowing down within the layer. The cascade nucleons are assumed to be emitted in the same direction as the incident particles producing the reaction. Further, it is assumed that the τ-function can be represented as the product.

$$\tau(E_I, E_S) = F(E_I) \cdot G(E_S) \qquad 4\text{-}13$$

Equations 4-5 through 4-13 are reduced to a more tractable form (see NR-140[9], pages 64-65) before being incorporated into the code for the normal incidence, continuous energy spectrum case. Modifications of these equations used in the monoenergetic and isotropic options are given in Sections 4.4 and 4.5 respectively.

The code proceeds step by step through the shield, calculating the energy spectrum of the primary and cascade nucleons after each layer. The energy mesh may contain 250 points divided into four ranges with constant energy spacing within each range. This arrangement permits the use of a relatively fine energy mesh at low energies, where the flux and stopping power vary rapidly.

One of the products of an inelastic nuclear collisions is a highly excited nucleus. Nucleons and, infrequently, heavier particles are evaporated as a result of this process. The heavy particles are ignored due to their rarity and short range. The protons are ignored due to their short range and due to the fact that the dominant source is frequently close to the entrance face of the shield. However, the evaporation neutrons are often quite significant. The computation of the evaporation neutron source is explained in Section 4.3.

Since the code yields the energy distribution of primary and cascade particles following each layer, it is possible to calculate physical dose (rad) or dose rate (rad/hr) in receiver material provided that suitable flux-to-dose conversion factors are available. Although some work is proceeding in this area, information is not completely adequate at present. For this reason, the code calculates an approximate lower limit and an upper limit on the physical dose due to primary and cascade nucleons. The lower limit on proton dose is obtained by considering ionization and atomic excitation energy losses in the receiver, ignoring nuclear interactions. The approximate lower limit on cascade neutron dose is obtained by use of an energy independent flux-to-dose conversion factor of 2.5×10^{-5} rad/hr per n/cm^2-sec. The upper limit for these doses is obtained from data[2] on the total energy removed from beams of high energy protons and neutrons due to interactions in tissue. These data are thought to form an upper limit on the volume dose at the surface of the receiver due to the fact that it is assumed the energy removed is deposited locally, whereas some of this energy actually goes into cascade particles which may penetrate some distance. These lower and upper limits are illustrated in Figure 4-4 for a typical case. Otherwise, all data presented in this report represent the lower limit case.

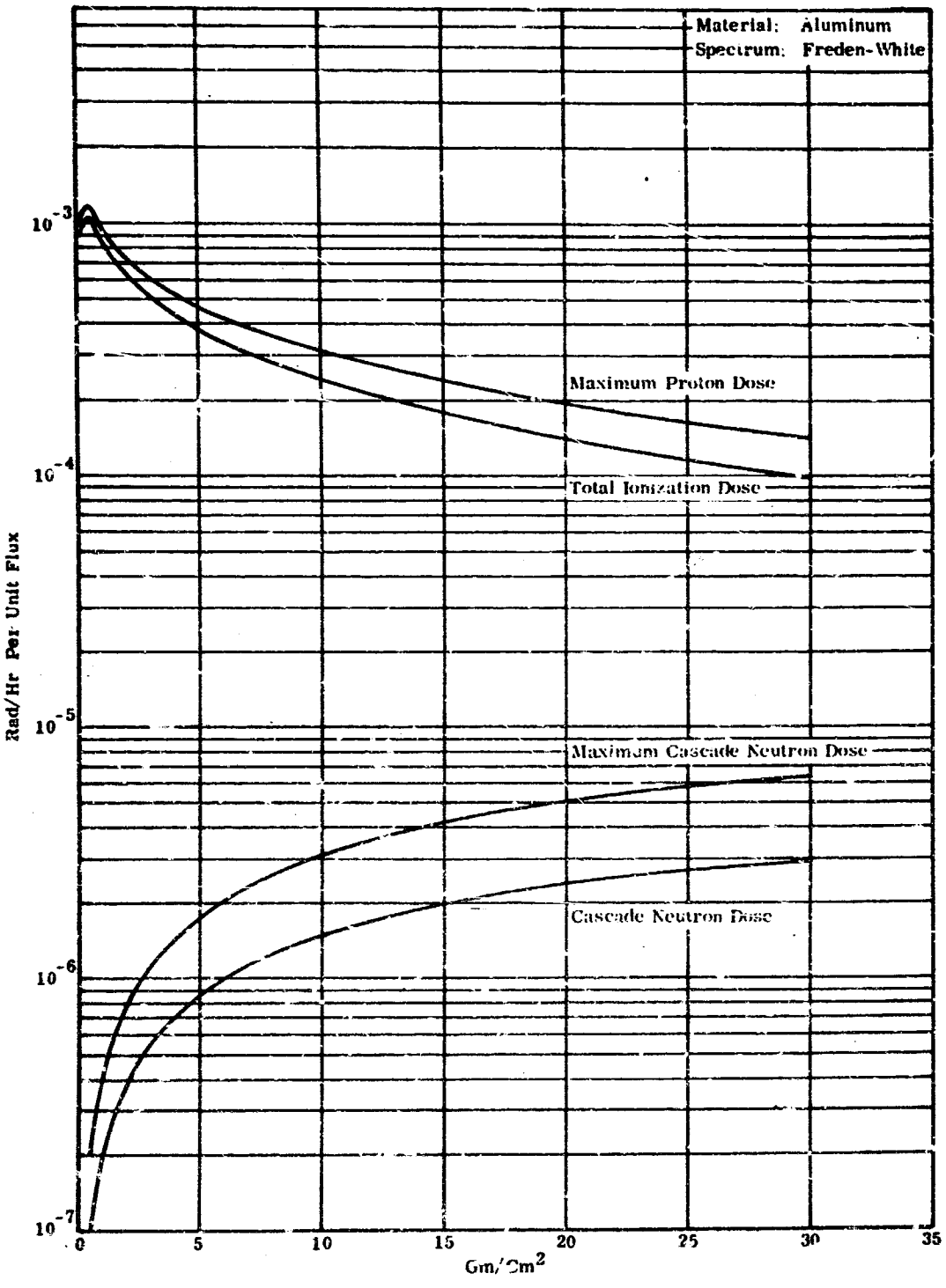

FIGURE 4-4 UPPER BOUND AND BEST ESTIMATE OF FAST NUCLEON DOSES

4.3 EVAPORATION NEUTRON DOSE

Protons incident on a material may suffer inelastic collisions with the nuclei. Cascade particles - predominately protons and neutrons - are immediately knocked out of the nucleus as a result of direct interactions. The residual nucleus is left in a highly excited state, and more particles may be ejected in the deexcitation process. Since these evaporation particles possess relatively little energy, the charged particles are stopped quickly. However, the evaporation neutrons may penetrate and increase the transmitted dose substantially.

The energy spectrum of the evaporation neutrons is continuous, with an upper bound of 10 to 20 Mev. The data available indicate that the spectrum peaks below one Mev and resembles the fission spectrum within experimental error.

The number of evaporation neutrons as a function of shield thickness is given by Equation 4-14 for protons incident normally on the shield.

$$S_{evap}(X)dX = dX \int_0^\infty \Phi_P(E,X)\ \Sigma_P(E)Y_P(E)dE + dX \int_0^\infty \Phi_N(E,X)\ \Sigma_N(E)Y_N(E)dE \qquad 4\text{-}14$$

where $S_{evap}(X)$ = neutron source density at X (n/gm-sec)

$\Phi_P(E,X), \Phi_N(E,X)$ = total proton (neutron) differential energy flux at X (particles/cm^2-sec-Mev)

$\Sigma_P(E), \Sigma_N(E)$ = inelastic cross section for protons (neutrons) (cm^2/gm)

$Y_P(E), Y_N(E)$ = evaporation neutron yield per inelastic collision.

For isotropic incidence, an integration over solid angle is necessary in order to compute the evaporation neutron source term. This is illustrated in Equations 4-37 and 4-38 (Section 4.5). The monoenergetic option of the code replaces the total proton flux with cascade proton flux and adds a term to account for evaporation neutrons generated by the primary proton beam. The equations for the continuous spectrum may be used if the total proton flux is understood to contain a continuous cascade proton flux plus a Dirac delta function term which, when integrated over energy, yields the monoenergetic primary flux.

The evaporation neutron dose at X is given by Equation 4-15:

$$D_{evap}(X) = \int_0^X T(X-X')S_{evap}(X')dX' \qquad 4\text{-}15$$

where $T(X-X')$ is the dose transmission function for neutrons from a plane isotropic source at X' to the exit surface at X. The source term, $S_{evap}(X')$ is calculated at $X' = 0$ and for each layer. (Formerly, $S_{evap}(0) = 2S_{evap}(X_1) - S_{evap}(X_2)$ which led to an erroneous starting value). Both the transmission function and the source term are assumed to vary exponentially inside a layer. Equation 4-15 is then approximated by Equation 4-16. The derivation is sketched in NR-140[9], page 86.

$$D_{evap}(X = \sum_{i=1}^{m} \Delta X_i) = \qquad 4\text{-}16$$

$$\sum_{i=1}^{m} \Delta X_i \frac{\left[T(X_m - X_i)S_{evap}(X_i) - T(X_m - X_{i-1})S_{evap}(X_{i-1})\right]}{\ln\left[T(X_m - X_i)S_{evap}(X_i)/T(X_m - X_{i-1})S_{evap}(X_{i-1})\right]}$$

The quantity still to be determined is the dose transmission function, $T(X - X')$. Even with the assumption that the neutrons are emitted isotropically with a fission spectrum, the dose transmission function is not easy to evaluate. Moments method data are available for a few elements and compounds. However, these data apply to an infinite homogeneous medium so that material changes and boundaries are not taken into account properly.

Boundary effects are important near the entrance face, where the source terms are largest for flare spectra and near the exit face, where the dose is evaluated.

Monte Carlo data are available for a few elements and compounds but the present data treat neutrons incident on a finite slab or on a semi-infinite slab which possesses an exit face but no entrance boundary. These two cases form lower and upper bounds respectively on the desired transmission function. It should be noted that the dose transmission function is represented by $T(X - X')$. This function will vary with X and X' even for constant differences, $X - X'$.

In addition, the proton penetration code produces a distributed neutron source in a shield composed of one to ten slabs of arbitrary composition. The moments method is not directly applicable to this situation. It appears that the Monte Carlo method is the preferred choice. It may be desirable to utilize a Monte Carlo code to treat this problem more exactly. Present Lockheed neutron Monte Carlo codes treat up to five layers with sources inside the shield.

It is not feasible to incorporate a Monte Carlo subroutine into the proton penetration code, since the cost in computer time would be exorbitant. It would be far better to use a Monte Carlo code to generate basic data, and to use this data for neutron transmission calculations. This method is described in NR-140[9], pages 84-90, for a one material slab. In addition to being limited to the one slab case, this method requires the user to set up his own dose transmission function table for each material - a laborious process for homogeneous shields composed of several materials. For these reasons, the calculation of evaporation neutron dose transmission factors has been generalized in the present code.

The method now incorporated is a point kernel approach based upon experimental removal cross sections for non-hydrogenous elements and upon a modification of a theoretical method for hydrogen, plus other materials, proposed by Albert and Welton[4]. However, this method breaks down for certain shield configurations;

empirical inferences based on limited experimental data and on heuristic arguments are included so that the general trend of the transmission function will be qualitatively correct.

The evaporation neutron dose transmission function is given by Equation 4-17.

$$T(X - X') = \frac{1}{2} \int_0^1 \frac{G(X - X', \theta)}{\cos \theta} d(\cos \theta) \qquad 4\text{-}17$$

$G(X - X', \theta)$ represents the material attenuation kernel. The form of G for shields without hydrogen is given in Equation 4-18. The factor of 1/2 in the exponent is an empirical correction to the removal cross section which is fairly consistent with experimental and Monte Carlo results.

$$G(X - X', \theta) = C_1 \text{ Exp } (-\frac{1}{2} \sum_i S_i r_i) \qquad 4\text{-}18$$

where C_1 = normalizing factor, $8.86\ 10^{-5}$ rad/hr per n/cm^2-sec and is obtained from normalizing to moments method data and Lid Tank Shielding Facility data.

S_i = removal cross section for the i^{th} layer (cm^2/gm).

r_i = slant penetration distance in the i^{th} layer (gm/cm^2)

i = layer number describing layers between X and X'.

The form of G for shields with hydrogen distribution throughout is given in Equation 4-19.

$$G(X - X', \theta) =$$

$$C_1 \left(\sum_i H_i \frac{r_i}{P_i} \right)^{C_2} \text{Exp} \left[- C_3 \left(\sum_i H_i \frac{r_i}{P_i} \right)^{C_4} \right] \cdot \text{Exp}(- \sum_i S_i r_i) \qquad 4\text{-}19$$

where the new terms are:

$C_2 = .29$

$C_3 = .83$

$C_4 = .58$

H_i = hydrogen density in layer i relative to the hydrogen density in water.

P_i = density of the material in layer i (gm/cm^3).

The intermediate case, where some slabs contain hydrogen and some do not, creates a special problem. For example, the energy spectrum of neutrons emerging from an iron slab immersed in water is quite different from the spectrum of neutrons in water alone as is evidenced by the data of Blizzard, Clifford, et al[8]. These data shown an initial rise of the thermal neutron flux behind an iron slab in the Lid Tank Facility, followed by a rapid drop. The slope gradually approaches the value it would have in water alone. The initial rise is due to two factors. First, inelastic scattering in iron reduces the energy of a large fraction of neutrons below one Mev. This low energy component is thermalized by four to ten inches of water behind the slab. Second, the capture cross section of iron is higher than that of water, which leads to a depression of the thermal flux in the neighborhood of the iron slab. The latter factor is not important to fast neutron dose calculations.

The departure from a water equilibrium spectrum is most severe directly behind the iron slab. The slope of the thermal flux curve indicates that equilibrium is reestablished some four to ten inches behind the iron slab, depending upon slab thickness. The pile-up of degraded neutrons arising from inelastically scattered but non-thermalized neutrons leads to an increased dose directly behind the slab which is approximated by applying a correction factor of one-half to the removal cross section as was explained above. The code adjusts this correction factor linearly from one-half to one as the following hydrogenous slab increases from zero to six inches in thickness.

The methods described above enable the code to treat attenuation of evaporation neutrons in non-hydrogenous and hydrogenous shields or in multistrata shields of arbitrary composition. Further experimental and theoretical work is required to test the validity

of the attenuation calculation and to examine the variations in evaporation neutron spectrum as a function of atomic number and bombarding energy.

4.4 MONOENERGETIC SPECTRUM

The proton penetration code was originally designed to treat a continuous proton energy spectrum. The spectrum option has been extended to treat monoenergetic protons. This option may be used to check against accelerator experiments, to generate shielding data for an arbitrary spectrum, to pin point energy regions important for secondary production, and to simplify check-out procedures for new code options.

The monoenergetic option is exact in the sense that a true line spectrum is used for primary protons while a continuous spectrum is used for cascade secondaries. The straight-ahead approximation is assumed and the rather small energy straggling is not accounted for.

The equations used in the code are substantially the same as those derived in NAA-140[9], pages 58-65, with the addition of several new terms and a redefinition of one symbol. The derivation and physical approximations for a continuous spectrum may be found in the above report. The final equations for the monoenergetic case are presented below. Symbols are defined as follows:

$\Phi_P(E, X)$, $\Phi_N(E, X)$ = Number of cascade protons (neutrons) per cm^2-sec-Mev at position X. In the non-monoenergetic case, the proton term includes primary protons also.

$\Phi_m(E, X)$ = Number of monoenergetic primary protons per cm^2-sec at position X.

E_I, E_S, E_m = Energy of incident, secondary, and monoenergetic nucleons in Mev.

$\Sigma_P(E)$, $\Sigma_N(E)$ = Inelastic cross sections in cm^2/gm

$\Phi_{PP}(E)dE, \Phi_{NP}(E)dE$ = Number of protons per cm^2-sec-Mev produced within incremental slab thickness, ΔX, by inelastic collisions of protons (neutrons) and having energy between E and E + dE at point of emergence $X + \Delta X$. $\Phi_{PN}(E)dE$ and $\Phi_{NN}(E)dE$ are similarly defined.

$\tau_{AB}(E_I, E_S)$ = Number of secondary nucleons of type B per unit secondary energy resulting from collision of a nucleon of type A with energy E_I.

$F_{AB}(E_I) \cdot G_{AB}(E_S)$ = $\tau_{AB}(E_I, E_S)$ for assumed separability of the secondary production function.

R(E) = Range of proton in gm/cm^2

S(E) = Stopping power of slab material in Mev-cm^2/gm.

E' = Energy of a proton reduced by ionization loss to energy E in traversing slab thickness ΔX.

The equations are then:

$$R(E'_m) = R(E_m) + \Delta X \qquad 4\text{-}20$$

$$\Phi_m(E_m, X + \Delta X) = \Phi_m(E'_m, X) e^{-\Sigma_P(E_m) \cdot \Delta X} \qquad 4\text{-}21$$

$$R(E') = R(E) + \Delta X \qquad 4\text{-}22$$

$$\Phi_P(E, X + \Delta X) = \Phi_P(E', X) \frac{S(E')}{S(E)} e^{-\Sigma_P(E) \cdot \Delta X} + \Phi_{PP}(E) + \Phi_{NP}(E) \qquad 4\text{-}23$$

$$\Phi_{PP}(E) = R_{PP}(E') \frac{i}{S(E)} \int_{E}^{E'} F_{PP}(E_S)dE_S$$

$$+ \frac{G_{PP}(E'_m)}{S(E)} \Sigma_P(E'_m)\Phi_m(E'_m, X) \int_{E}^{E'} F_{PP}(E_S)dE_S \qquad 4\text{-}24$$

$$R_{PP}(E') = \int_{E'}^{\infty} G_{PP}(E_I)\ \Phi_P(E_I, X)\ \Sigma_P(E_I)dE_I \qquad 4\text{-}25$$

$$\Phi_{NP}(E) = \frac{1}{S(E)} \int_{E}^{E'} R_{NP}(E_S)F_{NP}(E_S)dE_S \qquad 4\text{-}26$$

$$R_{NP}(E_S) = \int_{E_S}^{\infty} G_{NP}(E_I)\ \Phi_N(E_I, X)\ \Sigma_N(E_I)dE_I \qquad 4\text{-}27$$

$$\Phi_N(E, X + \Delta X) = \Phi_N(E, X)e^{-\Sigma_N(E)\Delta X} + \Phi_{PN}(E) + \Phi_{NN}(E) \qquad 4\text{-}28$$

$$\Phi_{PN}(E) = F_{PN}(E) \int_{E}^{\infty} \frac{G_{PN}(E_I)\ \Sigma_P(E_I)}{S(E_I)} \left[\int_{E_I}^{E'_I} \Phi_P(E^*_I, X)dE^*_I \right] dE_I$$

$$+ F_{PN}(E)G_{PN}(E'_m)\ \Phi_m(E'_m, X)\ \Sigma_P(E'_m, X)\ \Delta X \qquad 4\text{-}29$$

$$\Phi_{NN}(E) = \Delta X\ F_{NN}(E) \int_{E}^{\infty} G_{NN}(E_I)\ \Phi_N(E_I, X)\ \Sigma_N(E_I)dE_I \qquad 4\text{-}30$$

The equations given above are those used for protons incident along the slab normal. The isotropic flux case utilizes similar equations plus an integration over angle of incidence.

The doses are computed in such a manner that a simple hand calculation may be used to fold in an arbitrary spectrum. Let:

$D_m(E, X)$ = Dose rate at position X due to a monoenergetic beam in rad/hr per proton at energy E/cm^2-sec.

$\Phi_1(E)$ = Differential energy spectrum in p/cm^2-sec-Mev.

$\Phi_2(E)$ = Time integrated differential energy spectrum in p/cm^2-Mev.

$D_1(X)$ = Total dose rate at X due to $\Phi_1(E)$ in rad/hr.

$D_2(X)$ = Total time integrated dose at X due to $\Phi_2(E)$ in rads.

Using these definitions, Equations 4-31 and 4-32 yield the dose rate and dose respectively for arbitrary proton spectra.

$$D_1(X) = \int_0^\infty D_m(E, X)\, \Phi_1(E)dE \qquad 4\text{-}31$$

$$D_2(X) = \frac{1}{3600} \int_0^\infty D_m(E, X)\, \Phi_2(E)dE \qquad 4\text{-}32$$

Two examples of monoenergetic data are shown in Figures 4-5 and 4-6. These data are for protons incident normal to a slab of aluminum. Results are presented for 10 gm/cm^2 and 20 gm/cm^2. The narrow open peaks are due to the large stopping power of primary protons which are nearly stopped. An abrupt discontinuity occurs at the energy where range is equal to shield thickness.

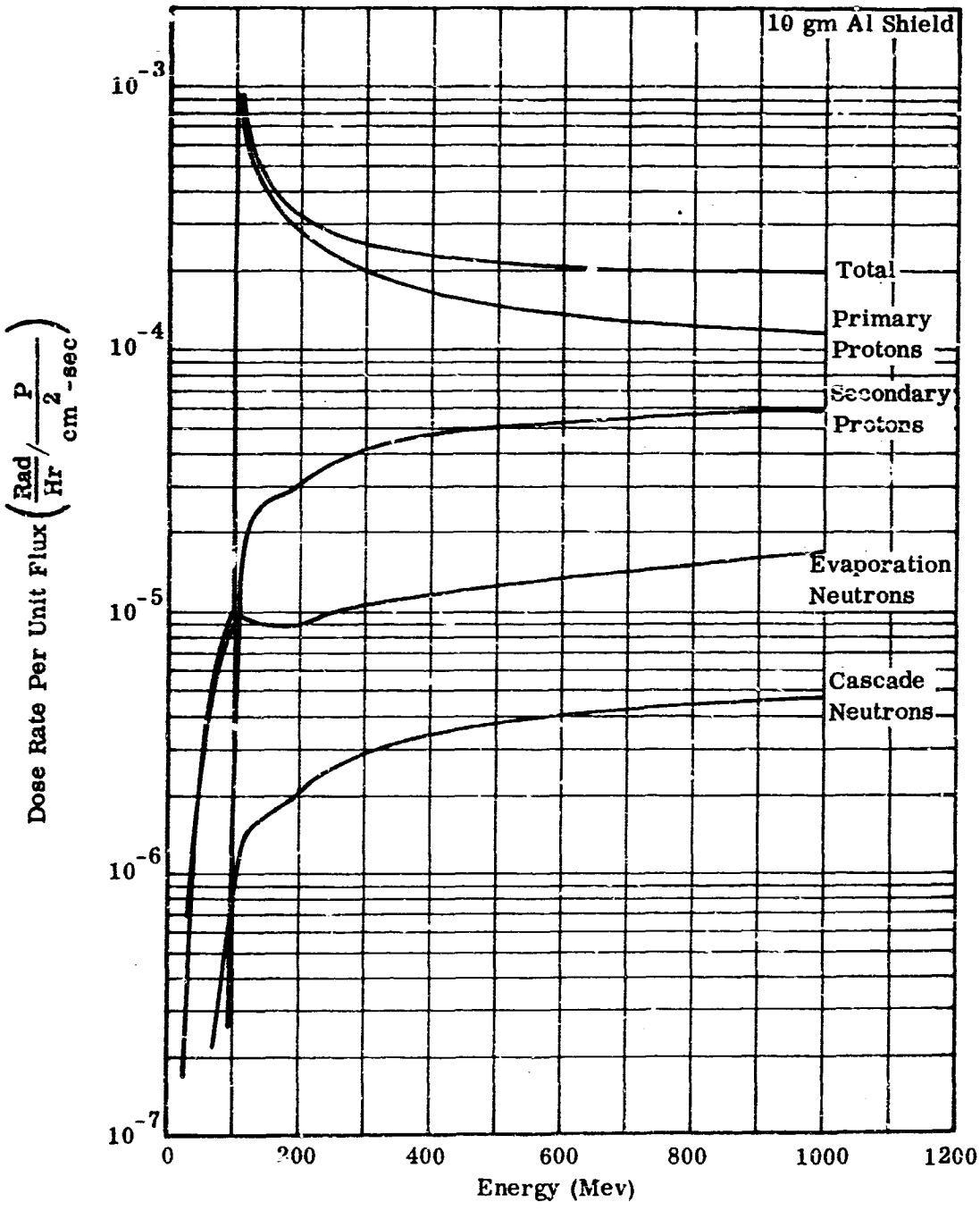

FIGURE 4-5 DOSE RATE PER UNIT FLUX VS ENERGY

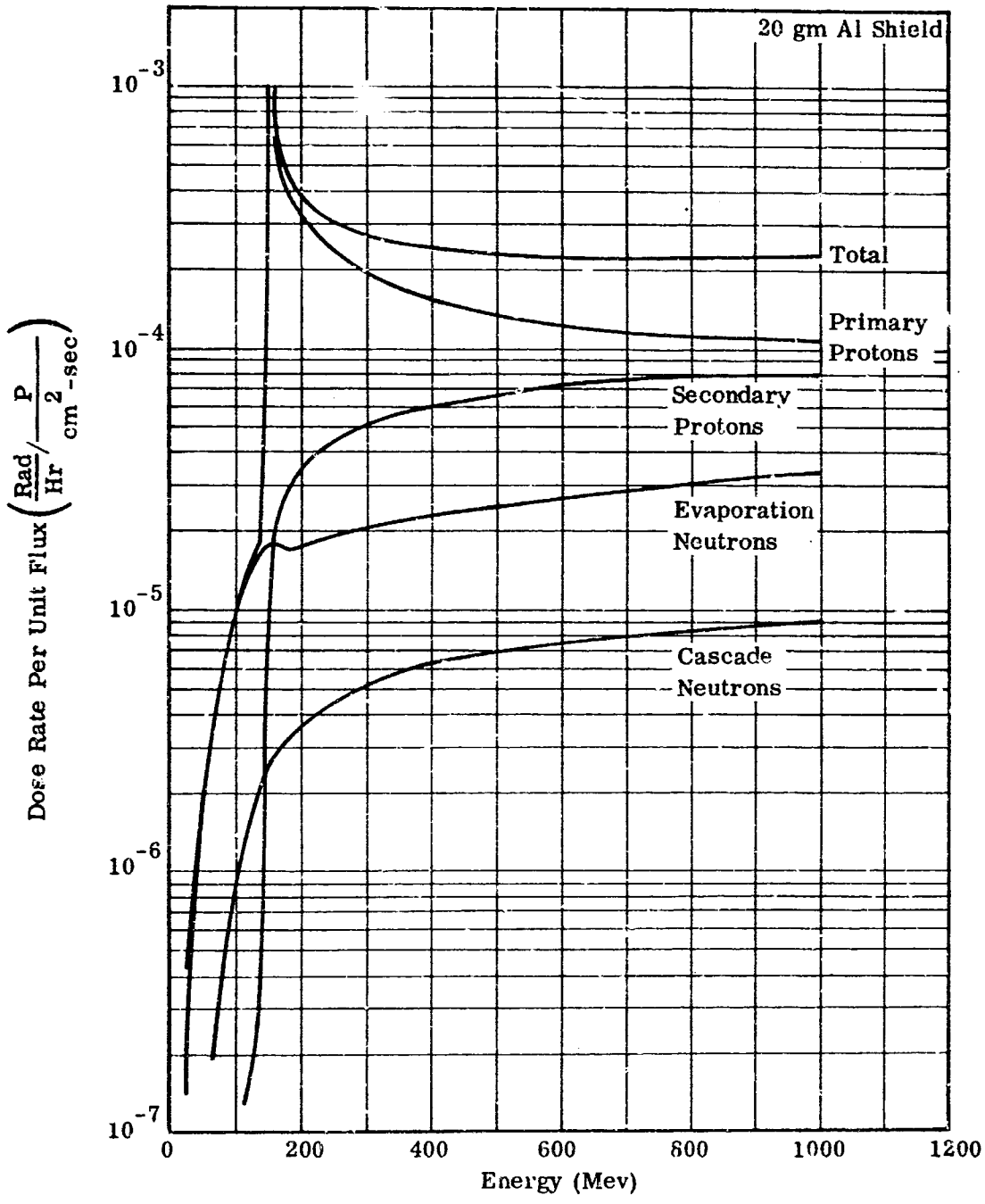

FIGURE 4-6 DOSE RATE PER UNIT FLUX VS ENERGY

Figures 4-7 and 4-8 were obtained from this data by folding in the Freden-White[5] spectrum according to Equation 4-31. Figures 4-9 and 4-10 were obtained by folding in a time-integrated flare spectrum according to Equation 4-32.

Figure 4-10 is especially interesting because it shows that a soft spectrum may generate enough evaporation neutrons to rival the primary dose for this thickness of aluminum. The dominant source is located in the first centimeter or two of aluminum. Also, the minor peak in the secondary proton spectrum near an incident energy of 50 Mev is principally a tertiary effect. A fraction of the incident protons entering with this energy are converted to neutrons through inelastic collisions. The neutrons penetrate part of the shield with no ionization loss, and a fraction are then converted back to protons by means of a second inelastic collision. It should be pointed out, however, that experimental and theoretical data are rather weak in these areas as regards production terms, angular distributions, and secondary energy spectra. Properly designed accelerator experiments could yield a great deal of interesting information on secondaries produced in shields by soft flare spectra. This point acquires added significance if a crude RBE of five to ten is assigned to evaporation neutrons. A 1 or 2 gm/cm^2 layer of a different material on the outside surface might materially reduce this component.

4.5 ISOTROPIC FLUX

The proton penetration code has been modified to include an option which calculates dose angular distributions behind a slab shield due to a plane isotropic incident flux. The isotropic option also calculates doses at the center of a spherical shield. The primary and cascade nucleons are assumed to continue straight ahead while the evaporation neutrons are assumed to be emitted isotropically. The straight ahead assumption is conservative for protons incident normally on a slab but it may cause either an overestimate or an underestimate of the dose for isotropic flux. It is easy to understand the possibility of an underestimate, as charged particles which are deviated towards the normal have a chance of escaping

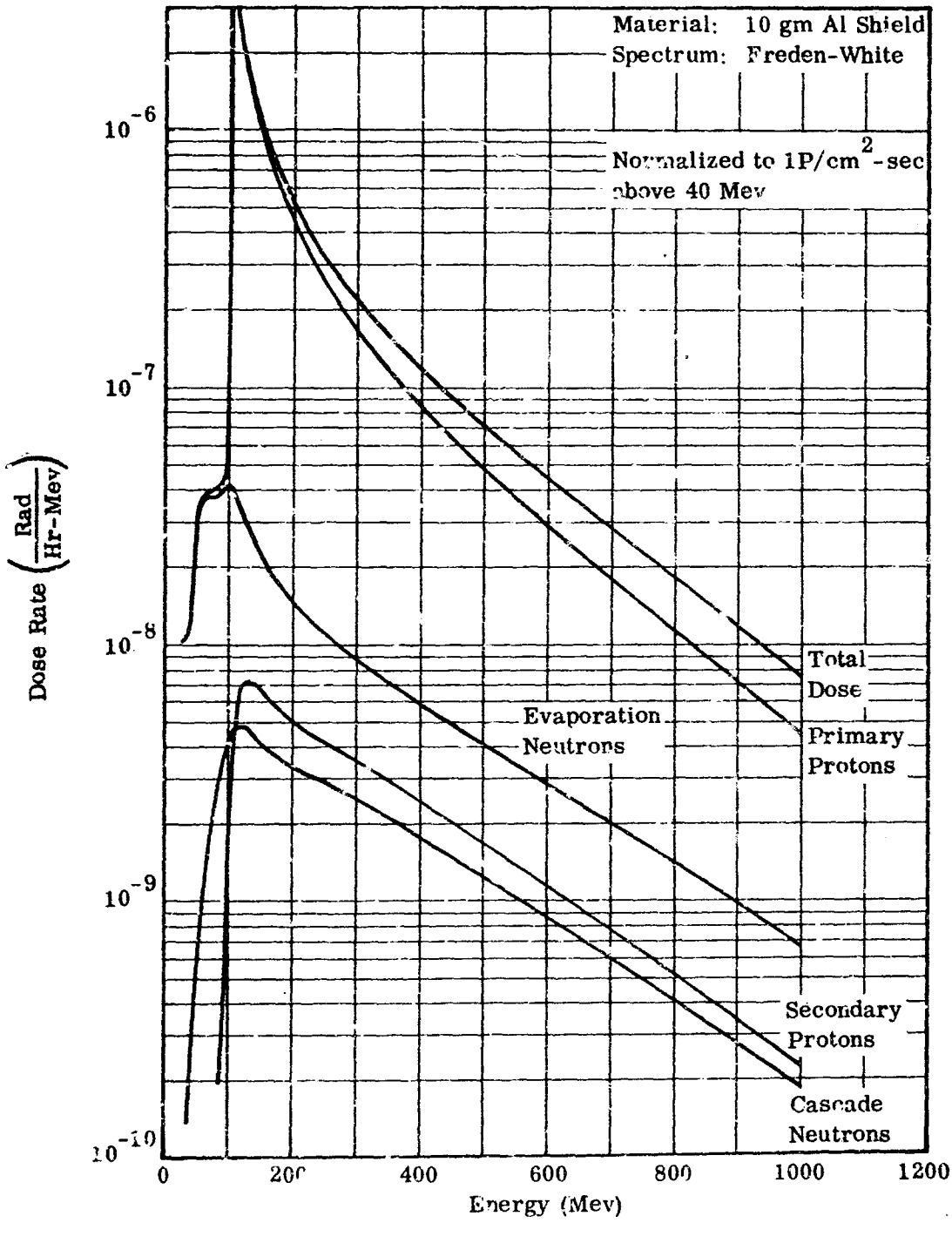

FIGURE 4-7 DIFFERENTIAL DOSE RATE FOR A FREDEN-WHITE SPECTRUM

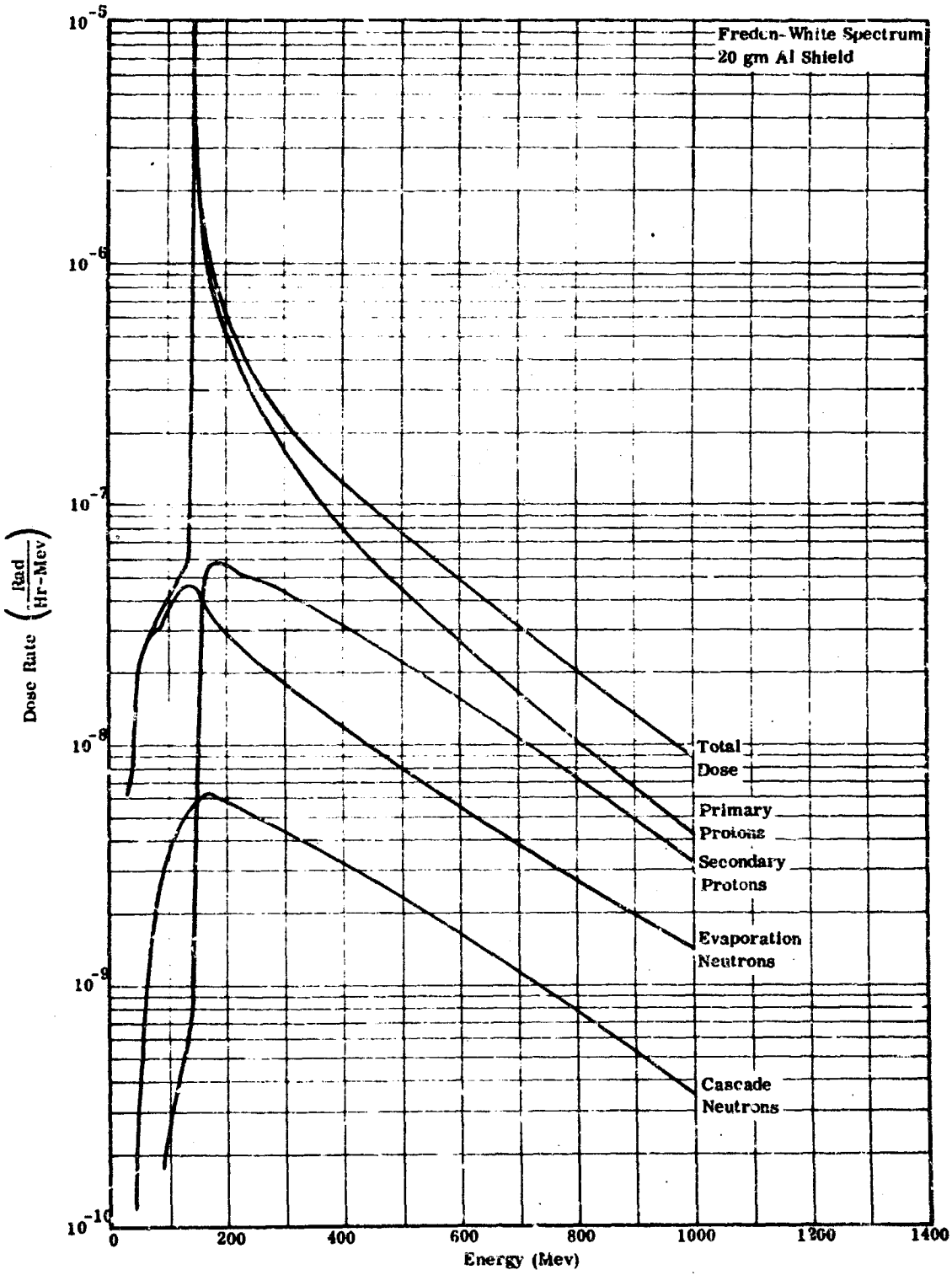

FIGURE 4-8 DIFFERENTIAL DOSE RATE FOR A FREDEN-WHITE SPECTRUM

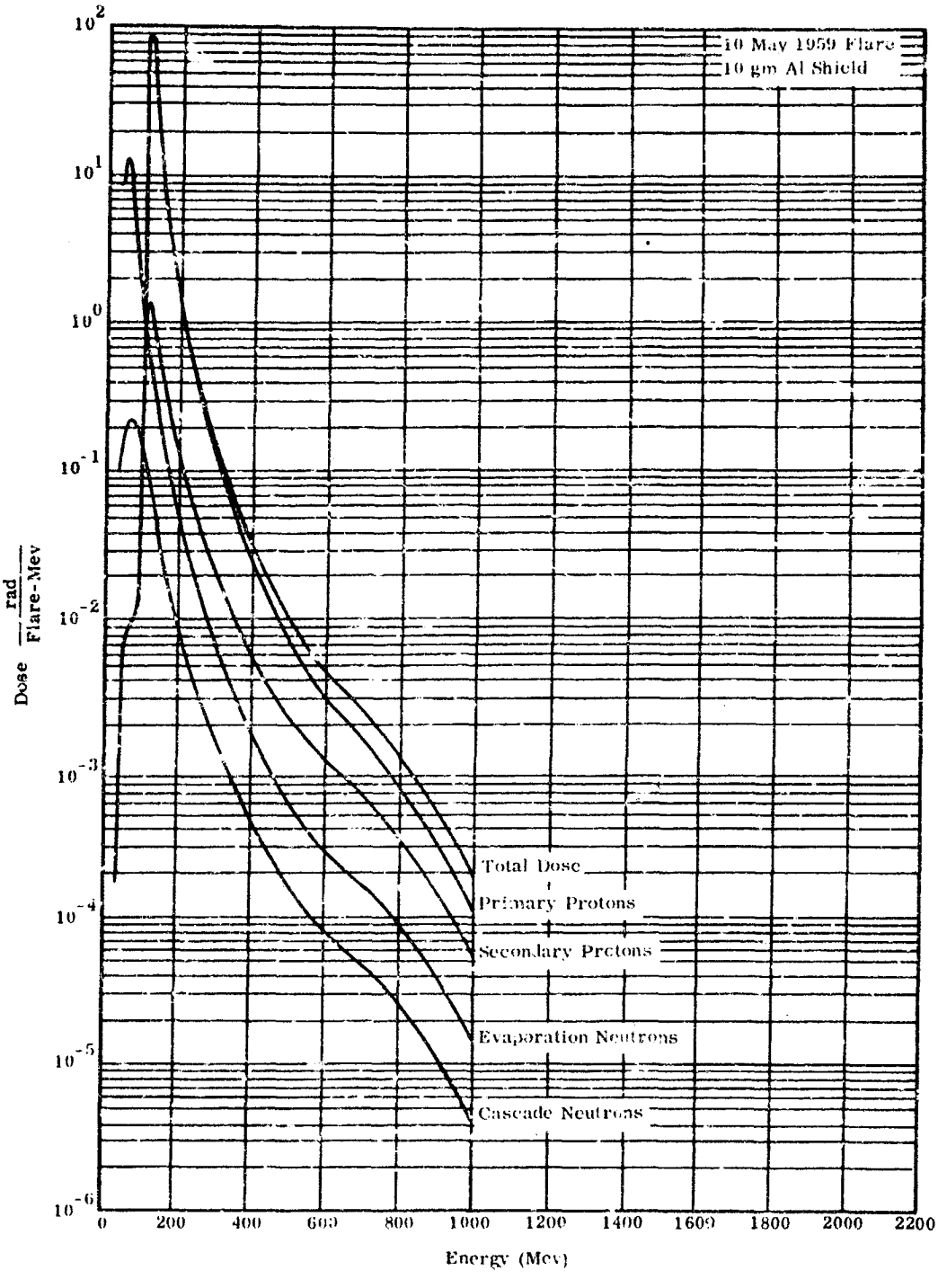

FIGURE 4-9 DIFFERENTIAL DOSE FOR A FLARE SPECTRUM

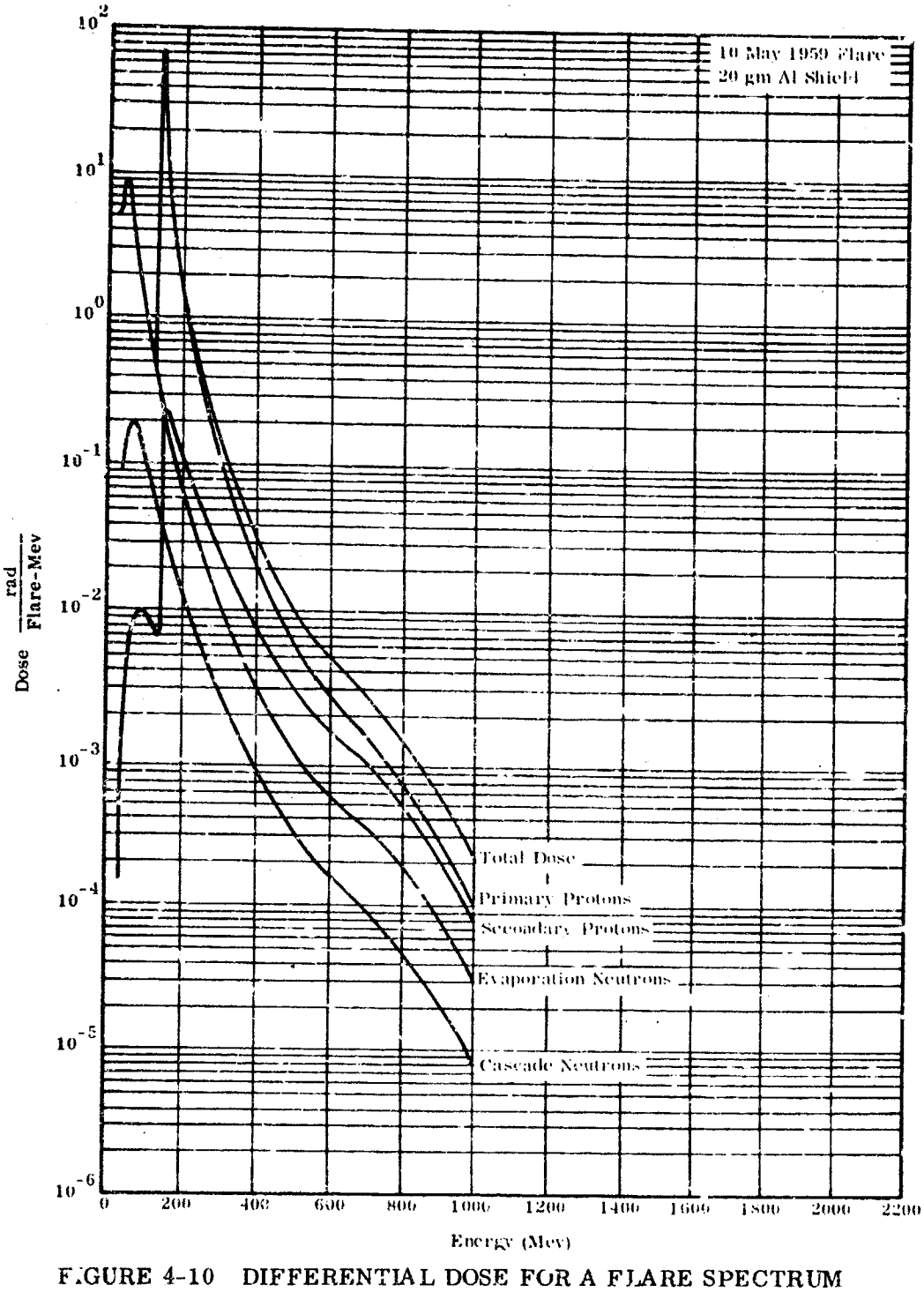

FIGURE 4-10 DIFFERENTIAL DOSE FOR A FLARE SPECTRUM

the slab in those cases where the straight ahead path would not permit particles to escape. However, an overestimate is also possible due to the variation of stopping power with energy for charged particles. A proton proceeding straight ahead might escape with relatively low energy and high stopping power while a proton deflected towards the normal would emerge with higher energy and lower stopping power. The dose at the slab surface is proportional to stopping power. A proton which deviates from the normal might emerge with a large stopping power, thus partially compensating for shorter path lengths, but it is also possible that the slant thickness may exceed the range of the proton, thus increasing the extent of the overestimate of the dose. The above discussion is somewhat academic since there are not enough data on cascade angular and energy distributions to permit proper exploration. The isotropic option has been coded in such a way that the above effects may be investigated when data become available.

The isotropic option is compatible with most of the other features of the code. For example, the input data for the energy spectrum may be in the form of a power law, or exponential law, or may be tabular, or monoenergetic. However, an instruction to print out the spectrum as a function of angle, thickness and energy is ignored since this would produce a huge quantity of data.

One aspect of the compatibility requirement is mildly inconvenient. The code is designed to treat plane shields composed of one to ten strata with arbitrary composition. Each stratum may be further subdivided into layers. Doses are calculated after each layer. If the shield is homogeneous, the dose may be taken along the normal for large thickness, and a transformation applied to obtain the dose as a function of polar angle after each layer as shown in Section 4.6. This method is not valid for multistrata shields as the stopping power and secondary production rate change abruptly when a new material is entered. The position of the break depends upon the angle of incidence. Rather than treat the two cases in a different manner, it was decided to treat them in the same manner. This choice also permits the addition of a non-straight ahead secondary production and scattering option when suitable data become available.

The isotropic flux option of the code proceeds in a rather straightforward manner to calculate particle fluxes, doses, and evaporation neutron source terms after each layer for each of ten angles of incidence. These quantities are then integrated over the hemisphere. Thus the calculation uses the same methods that are used in the normal incident flux option except for normalizing factors and an integration over solid angle. These features will be illustrated briefly.

Consider an isotropic flux $\Phi_2(E)$ p/cm^2-sec-Mev. Then the angular flux is given by Equation 4-33.

$$\Phi_1(E, \Omega) = \frac{1}{4\pi} \Phi_2(E) \text{ p/cm}^2\text{-sec-Mev-ster} \qquad 4\text{-}33$$

The number of protons entering a small plane area, dA, in $d\Omega$ at angle θ is

$$N(E) = \Phi_1(E, \Omega) \cos\theta \, dA \, d\Omega \text{ p/sec-Mev} \qquad 4\text{-}34$$

Integration over the hemisphere on one side of dA indicates that $1/4\ \Phi_2(E)$ is the scalar current entering the plane surface, as is expected. A minor change in notation will be made to simplify this illustration, that is, $\Phi_1(E, \Omega)$ will be replaced by $\Phi_1(X, E, \theta)$ where X is the perpendicular distance through the shield in gm/cm^2 and θ is the angle between the incident proton and the normal to the shield. The number of protons entering one square centimeter per second at an angle θ in $d\Omega$ is then

$$\Phi_1(0, E, \theta) \cos\theta \, d\Omega$$

This current is attenuated through a slant thickness $X/\cos\theta$ and cascade secondaries are produced in the same way as in the normally incident flux option (see NR-140). The dose due to primary protons at X is then

$$\text{Dose (X)} = 2\pi \int_0^1 \frac{D(X, \theta)}{\cos\theta} \, d(\cos\theta) \qquad 4\text{-}35$$

where

$$D(X, \theta) = K \int_0^\infty S(E)\ \Phi_1(X, E, \theta) \cos\theta\ dE \qquad 4\text{-}36$$

and K = dose conversion factor $\frac{\text{rad/hr}}{\text{Mev/cm}^2\text{-sec}}$

$$S(E) = \text{receiver stopping power } \frac{\text{Mev}}{\text{gm/cm}^2}$$

The $\cos\theta$ factors in Equations 4-35 and 4-36 cancel. Cascade proton and neutron doses are computed in a similar fashion.

The evaporation neutron source terms are calculated as follows. Consider a flux of protons or neutrons incident at an angle θ on a lamina dX gm/cm^2 thick at X as shown in Figure 4-11.

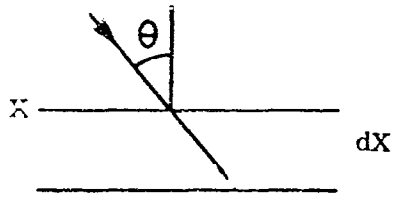

FIGURE 4-11 GEOMETRY OF EVAPORATION NEUTRON SOURCE CALCULATION

The number of particles per second penetrating one square centimeter at X is $\Phi_1(X, E, \theta) \cos\theta$ protons and $\Phi_1^N(X, E, \theta) \cos\theta$ cascade neutrons. The number of evaporation neutrons generated per unit area in dX is:

$$N_{evap}(X, \theta)\, dX = \frac{dX}{\cos\theta} \int_0^{\infty} \Phi_1 (X, E, \theta) \cos\theta \ \Sigma_p(E) Y_p(E)\, dE$$

$$+ \frac{dX}{\cos\theta} \int_0^{\infty} \Phi_1^N (X, E, \theta) \cos\theta \ \Sigma_N(E) Y_N(E) dE \qquad 4\text{-}37$$

where $N_{evap}(X, \theta)\, dX$ = number of evaporation neutrons in neutrons/gm-sec emitted isotropically from volume $1 \cdot dX$ at X due to total proton flux $\Phi_1(X, E, \theta)$ and cascade neutron flux $\Phi_1^N (X, E, \theta)$.

$\Sigma_A(E)$ = inelastic cross section cm^2/gm for particles of type A.

$Y_A(E)$ = number of neutrons produced per inelastic collision for particles of type A.

The total number of neutrons is:

$$S_{evap}(X)dX = 2\pi\, dX \int_0^1 N_{evap} (X, \theta) d(\cos\theta) \qquad 4\text{-}38$$

The evaporation neutron dose is given by:

$$D_{evap} (X) = \int_0^X T(X - X') S_{evap}(X') dX' \qquad 4\text{-}39$$

where $T(X - X')$ = dose transmission factor, i.e., dose rate at X due to a unit plane isotropic source at X' (rad/hr per n/cm^2-sec).

The computation of dose transmission factors is described in Section 4.3.

Caution should be used in running the isotropic option in combination with the monoenergetic option. If the shield thickness is less than the range of the primary protons, but some of the slant thicknesses are greater than the range, the situation depicted in Figure 4-12 will arise. The solid curve represents the true angular dose and the dotted curve delineates the curve which the code integrates.

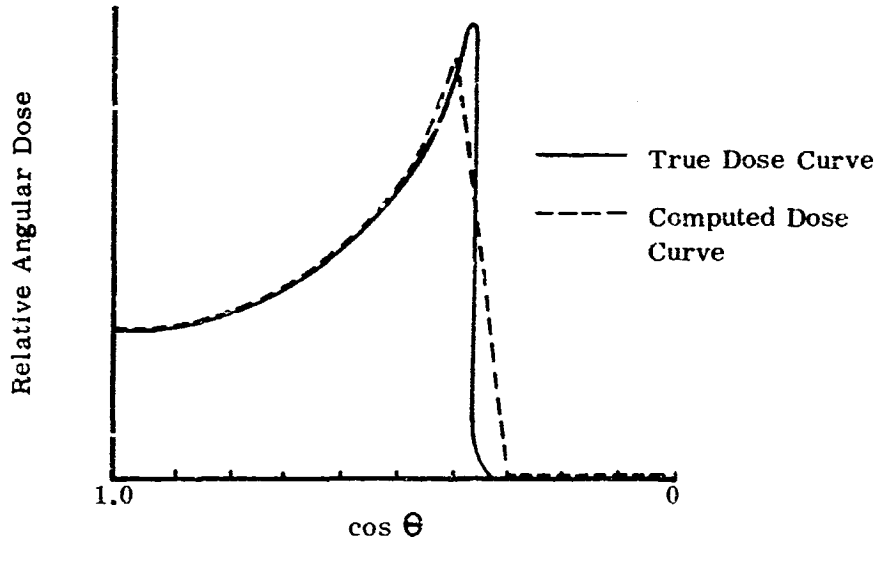

FIGURE 4-12 RELATIVE ANGULAR DOSE EMERGING FROM SHIELD THICKNESS X VERSUS COS θ FOR MONOENERGETIC ISOTROPIC FLUX

The troubles arise because the numerical integration is performed at fixed intervals over a function which peaks sharply due to the Bragg effect. This difficulty is not serious in an integration over a continuous spectrum because most of the ionization dose comes from higher energy particles and sharp peaks in the angular dose curve do not occur.

4.6 USE OF LPPC RESULTS

The proton penetration code treats the problem of protons and their associated secondaries, tertiarties, etc., which penetrate a rather simple shield geometry, i.e., a finite planar shield of infinite extent. The question arises as to how these data may be applied to a more realistic configuration. This section explains the model upon which the calculation is based for conversion from slab to spherical geometries, and appropriate ways to utilize the results.

At present, LPPC considers four radiation components; primary protons, secondary protons, cascade neutrons, and evaporation neutrons. The first three components are treated according to a straight ahead approximation so that emergent dose angular distributions may be calculated. The fourth component, evaporation neutrons, are assumed to leave the excited nucleus isotropically. The emergent angular distribution of the evaporation neutrons is a complex fuction of source distribution, slab thickness, and neutron cross sections of the shield material. For an infinite plane source, the flux angular distribution will be proportional to $1/\mu$ where μ is the cosine of the angle between the neutron path and the shield normal. Slabs of finite thickness remove the discontinuity at $\mu = 0$, and the angular distribution may approach an isotropic or cos θ form. Since sufficient data are not presently available, it is preferred that simple forms be used to represent this function; perhaps isotropic for relatively thin shields and a cosine function for thick shields. The straight ahead components and the evaporation neutrons will be discussed separately.

For the moment, consider the primary and cascade components only.

Let $\Phi_1(E_1, \Omega)$ = angular flux, p/cm^2-sec-Mev-ster in the direction

$\Phi_2(E)$ = isotropic flux, p/cm^2-sec-Mev

$D_1(\Omega, X)$ = angular dose rate at X, rad/hr-ster, due to $\Phi_1(E, \Omega)$ for all E

$D_2(X)$ = dose rate at the center of a spherical shell of thickness X and radius R due to an isotropic flux $\Phi_2(E)$ in rad/hr.

μ = cosine of the angle θ between Ω and shield normal.

Then

$$\Phi_2(E) = \int_{\Omega} \Phi_1(E, \Omega)d\Omega = 4\pi \ \Phi_1(E, \Omega) \qquad 4\text{-}40$$

Consider the proton angular flux, $\Phi_1(E, \Omega)$ in $d\Omega$, incident on a slab shield as shown in Figure 4-13. A primary and cascade dose labeled $D_1(\Omega, X)$ emerges on the other side.

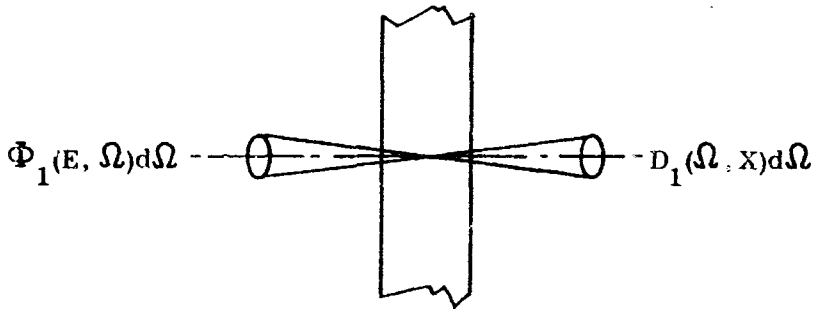

FIGURE 4-13 PLANE GEOMETRY DOSE

The code is eminently suited to treat the case shown in Figure 4-13.

Next, consider a spherical shell embedded in an isotropic flux with the receiver located at the center as shown in Figure 4-14. The thickness, X, must be much smaller than the radius, if doses are to be computed at points other than at the center. The angular flux incident normal to the surface along a radius at P delivers a dose to the receiver. If Ω does not point towards the center, as at P', no straight ahead dose reaches the receiver. Integrating,

$$D_2(X) = \int_{\Omega} D_1(\Omega = 1, X)d\Omega$$
$$= 4\pi D_1(\Omega = 1, X) \qquad 4\text{-}41$$

where $D_2(X)$ is the straight ahead dose component at the center of a spherical shell shield due to an isotropic flux $\Phi_2(E)$. The dose is not constant within the sphere unless the emergent angular distribution, $D_1(\Omega, X)$, is isotropic. Standard methods available in the literature[6] may be used to show that, in this idealized situation, the wall dose is one half the center dose if $D_1(\Omega, X)$ has a cosine distribution; and one-third of the center dose, if $D_1(\Omega, X)$ has a cosine squared distribution.

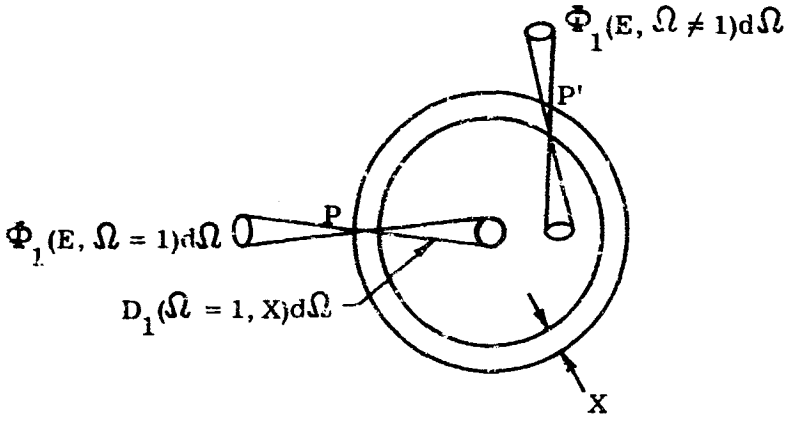

FIGURE 4-14 SPHERICAL GEOMETRY DOSE

The dose components labeled Primary Protons, Secondary Protons, and Cascade Neutrons in Appendix II are computed according to Equation 4-41. That is, they represent doses at the center of a spherical shell embedded in an isotropic proton flux $\Phi_2(E)$. The dose component labeled Evaporation Neutrons is also converted to a spherical geometry as will be explained later.

The spherical geometry doses may be used for approximate dose calculations and parametric surveys. More exact calculations in realistic geometries require the function $D_1(\Omega, X)$ versus μ, the cosine of the angle between the direction Ω and the shield normal. There are several ways of obtaining this function. The method suggested in this report is as follows. First, sum the three straight ahead components. Divide this quantity by 4π to obtain $D_1(1, X)$ where the first argument implies that value of Ω for which μ is one. The following polynomial is then used to define the dose angular distribution.

$$D_1(\mu, X) = D_1(1, X)\left[a + b\mu + c\mu^2\right] \qquad 4\text{-}42$$

or, more simply

$$D_1(\mu, X) = \frac{D_2(X)}{4\pi}\left[a + b\mu + c\mu^2\right] \qquad 4\text{-}43$$

The quantity, $D_2(X)$, is given by the sum of primary and cascade components on the graphs in Appendix II. The parameters (a, b, c) are obtained from a least squares fit to the proton penetration code results. A table of these values is given in Appendix I.

Some caution should be taken when Equations 4-42 or 4-43 are used. In certain cases, the polynomial becomes negative. This anomaly may occur for those values of μ where $D_1(\Omega, X)$ is several orders of magnitude below D(1, X). The dose may be set to zero in this instance or extrapolated to zero at $\mu = 0$ in an appropriate way.

The simple formalism developed above is convenient but is not unique. For example, Equation 4-42 might be expressed in the form of Equation 4-44.

$$D_1(\mu, X) = D_1(1, X/\mu) \qquad 4\text{-}44$$

The form of Equation 4-44 may serve multiple purposes. For a simple slab, it may be used to find the angular distribution of the straight ahead dose components for an isotropic flux using data

from a normal incidence case. Conversely, the angular distribution may be used to extend the data to greater thickness.

The evaporation neutron dose component is treated in a slightly different way. The volume distribution of sources depends upon the incident flux angular distribution in a way similar to that of cascade nucleons. However, the isotropic nature of the source complicates the situation. The additional notation necessary is defined below.

$D_1'(\Omega, X)$ = evaporation neutron angular dose rate at X in rad/hr due to isotropic flux $\Phi_2(E)$ incident on a plane slab. Note the difference in flux specification for this quantity from that of $D_1(\Omega, X)$ above.

$D_2'(X)$ = evaporation neutron dose rate in rad/hr at the center of a spherical shell shield of thickness X due to an isotropic flux $\Phi_2(E)$.

$D_3'(X)$ = evaporation neutron dose rate in rad/hr at the exit face of a slab shield due to a (half) isotropic proton flux incident on the entrance face.

Consider an isotropic flux $\Phi_2(E)$ incident on one side of a plane slab shield as in Figure 4-15. The code calculates the dose emerging from the other side $D_3'(X)$. Assume this dose is emitted with a cosine distribution.

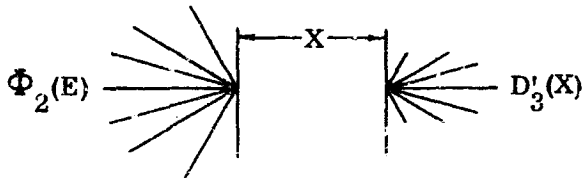

FIGURE 4-15 PLANE GEOMETRY EVAPORATION NEUTRON DOSE

Then:

$$D'_3(X) = \int_{\Omega/2} D'_1(\Omega, X)d\Omega \qquad 4\text{-}45$$

where

$$D'_1(\Omega, X) = \frac{N}{\pi}\mu \qquad 4\text{-}46$$

$$D'_3(X) = \frac{N}{\pi}\int_{\Omega/2} \mu d\Omega = N$$

or

$$D'_1(\Omega, X) = \frac{D'_3(X)}{\pi}\mu \qquad 4\text{-}47$$

The dose $D'_2(X)$ at the center of a spherical shell shield is:

$$D'_2(X) = \int_{\Omega} D'_1(1, X)d\Omega$$

$$D'_2(X) = \frac{2\pi}{\pi} D'_3(X)\int_{-1}^{1} d\mu$$

$$D'_2(X) = 4D'_3(X) \qquad 4\text{-}48$$

$D'_2(X)$, the evaporation neutron dose at the center of a spherical shell shield due to an isotropic incident flux of protons, is the quantity presented in Appendix II.

The data presented may be converted to the dose emerging from a plane slab due to an isotropic flux incident on the other side by means of Equation 4-49.

$$D'_1(\Omega, X) = \frac{D'_2(X)}{4\pi}\mu \qquad 4\text{-}49$$

A distinction exists between the D_1 function of the straight ahead component and the D_1' function of the evaporation neutron component. $D_1(\Omega, X)d\Omega$ is due to the angular flux $\Phi_1(E, \Omega)d\Omega$ while $D_1'(\Omega, X)d\Omega$ is due to an isotropic flux incident on one side of a plane shield.

A complex geometry shield may be treated by representing the configuration with a polyhedron made up of small plane slabs. The dose at an inside point may then be computed by incorporating the results of Equations 4-43 and 4-49 plus data in Appendix I into an appropriate integration over the surface.

A major uncertainty in the estimation of space radiation doses is due to lack of knowledge concerning space radiation sources. The results presented in Appendix II for solar flares should be regarded as tentative, but conservative values. In the case of the 10 May 1959 flare, the spectrum measured at 33 hours after onset was extrapolated back to one hour according to a t^{-2} law. The actual spectrum and intensity variations during the early part of the flare are unknown. It is probable that flare particles arrived in the vicinity of the earth five hours after onset and reached a maximum approximately seven hours later. In the case of the 23 February 1956 flare, the prompt spectrum at one hour after onset was assumed to decay according to a t^{-2} law also. The spectrum measured eighteen hours later was much softer. Both spectra, when extrapolated according to t^{-2}, yield approximately the same dose behind five to ten gm/cm^2 of shielding. The prompt spectrum was used for data presented in Appendix II.

4.7 REFERENCES

(1) O'Brien, B. J.; Van Allen, J. A.; Laughlin, C. D.; Frank, L. A.: Absolute Electron Intensities in the Heart of the Earth's Outer Radiation Zone, J. Geo. Res., Vol. 67, No. 1, January, 1962, p. 391.

(2) Koch, H. W.; Motz, J. W.: Bremsstrahlung Cross-Section Formulas and Related Data, Rev. Mod. Phys., Vol. 31, No. 4, pp. 920-955, October 1959.

(3) Gibson, W. A.: Oak Ridge National Laboratory, private communication.

(4) Albert, R. D.; Welton, T. A.: WAPD-15, November 30, 1950 (declassified).

(5) Freden, S. G.; White, R. S.: Particle Fluxes in the Inner Radiation Belt, J. Geophys. Res. 65, 1377, 1960.

(6) Case, K. M.; de Hoffmann, F.; Placzek, G.: Introduction to the Theory of Neutron Diffusion, Volume I, p. 1-6.

(7) Goldstein, H.; Wilkins, J. E.: Calculations of the Penetration of Gamma Rays, NYO-3075, 1954.

(8) Rockwell, T.: Editor, Reactor Shielding Design Manual, TID 7004, 1956, p. 61.

(9) Allen, R. I.; Bly, F. T.; Dessler, A. J.; Douglass, C. C.; Perkings, J. F.; Price, H. C.; Schofield, W. M.; Smith, E. C.: Shielding Problems in Manned Space Vehicles, NR-140, 1961.

BLANK PAGE

5.0 SUMMARY AND CONCLUSION

5.1 RADIATION SOURCES

Data on radiation sources in the trapped natural radiation zones are being supplemented by continuing satellite and rocket probes. Flux maps are available which are probably accurate within a factor of three for high thrust escape trajectories. Improved mapping supplemented by analysis of particle motion within the earth's magnetic field, should yield results sufficiently accurate for most shielding calculations. However, information on spectral and temporal variations is rather sparse. Very little data have been published as yet on the new electron belt produced by high altitude nuclear weapon bursts.

Solar flares appear to offer the major space radiation hazard for missions outside the geomagnetic field. At present it appears that the hazard from frequent small flares is less than from cosmic rays (about 20 rem/yr). Gigantic flares, however, may produce doses of thousands of rem behind thin shields. A recent estimate of the time and spectral history of gigantic flares yields doses of 4000 rads, 700 rads, and 300 rads behind aluminum shields of 1 gm/cm^2, 3 gm/cm^2, and 5 gm/cm^2 respectively. While this estimate yields doses generally lower than the t^{-2} model (see Appendix II), the doses are still seriously large.

The incidence of gigantic flares has not been observed long enough to obtain good statistics. Sparse data indicate that these flares are likely to occur on the rising and falling portion of the sunspot cycle. It would be helpful in prediction studies if flares could be correlated with some feature of the Babcock model.

5.2 RADIATION TRANSPORT

The proton shielding code developed during previous studies has been extended to treat isotropic fluxes as well as monodirectional

fluxes and monoenergetic spectra as well as continuous spectra. Shield geometries include plane slab shields and spherical shell shields. Angular distributions of the primary and cascade secondary doses are calculated using the straight ahead approximation for cascade nucleon production. Multistrata shields may also be analyzed.

Secondary radiations include cascade neutrons, cascade protons, and evaporation neutrons. The code will probably be extended to estimate gamma ray production in certain elements in the near future. Pion and muon production appears to be small for shields less than 100 gm/cm^2 thick.

The cascade nucleon production and spectral data are taken from the work of Metropolis, et al. This Monte Carlo calculation was performed for aluminum and heavier elements in the energy range 82 to 1840 Mev. Extrapolations to lower energies and lighter elements may be somewhat risky. It would be desirable to check the calculation against experimental data. Unfortunately, the field of nucleon-nucleus cross section measurements has been rather quiet for the past seven years and few systematic studies are available.

Analysis of electron bremsstrahlung produced by electrons in the natural radiation belts show that this component is small compared to the proton dose for escape missions. However, the electrons resulting from nuclear weapon bursts may possess energies of seven Mev or higher. Thus, penetrating electrons may be important for thinly shielded vehicles. It would be desirable to develop transport methods for electrons in this energy range.

APPENDIX I

DOSE ANGULAR DISTRIBUTIONS

The following tables present least squares fits to the sum of primary proton dose, secondary proton dose, and cascade neutron dose as a function of emergent angle for isotropic flux incident on a plane slab shield. The functional form is a second degree polynomial in μ, the cosine of the angle between the emergent dose and the slab normal. Normalizing factors are given in Section 4.6, Equation 4-43.

TABLE I-1

DOSE ANGULAR DISTRIBUTIONS - WATER

Thickness gm/cm^2	Freden-White Spectrum			10 May 1959 Flare Spectrum			23 February 1956 Flare Spectrum		
	a	b	c	a	b	c	a	b	c
0.5	0.2183	1.3817	-0.6171	-0.1338	1.3746	-0.2334	0.2437	1.1551	-0.4007
1.0	0.1418	1.4786	-0.6357	-0.1015	0.7127	0.4110	0.2429	1.1855	-0.4392
2.0	0.0904	1.4281	-0.5277	-0.0084	-0.0916	1.1128	0.2496	1.1359	-0.3922
3.0	0.0624	1.4139	-0.4856	0.0285	-0.3714	1.3468	0.2570	1.1108	-0.3765
4.0	0.0435	1.4086	-0.4597	0.0517	-0.5293	1.4706	0.2615	1.1145	-0.3859
5.0	0.0283	1.3991	-0.4350	0.0616	-0.5949	1.5228	0.2584	1.1421	-0.4109
6.0	0.0141	1.4003	-0.4222	0.0708	-0.6510	1.5709	0.2528	1.1695	-0.4334
7.0	0.0023	1.4008	-0.4103	0.0867	-0.7413	1.6477	0.2456	1.1949	-0.452
8.0	-0.0076	1.3945	-0.3937	0.1066	-0.8426	1.7182	0.2364	1.2221	-0.4718
9.0	-0.0167	1.3903	-0.3800	0.1192	-0.8900	1.7405	0.2264	1.2551	-0.4962
10.0	-0.0244	1.3845	-0.3658	0.1255	-0.8935	1.7323	0.2158	1.2909	-0.5223
12.0	-0.0362	1.3696	-0.3373	0.1316	-0.8449	1.6742	0.1983	1.3455	-0.5605
14.0	-0.0446	1.3447	-0.3022	0.1377	-0.7719	1.5985	0.1790	1.3991	-0.5963
16.0	-0.0497	1.3112	-0.2619	0.1480	-0.6996	1.5198	0.1594	1.4524	-0.6316
18.0	-0.0528	1.2754	-0.2219	0.1618	-0.6246	1.4332	0.1408	1.5022	-0.6643
20.0	-0.0546	1.2418	-0.1854	0.1784	-0.5464	1.3391	0.1223	1.5517	-0.6961
22.0	-0.0548	1.2067	-0.1488	0.1974	-0.4627	1.2401	0.1064	1.5895	-0.7178
24.0	-0.0538	1.1706	-0.1119	0.2190	-0.3833	1.1424	0.0922	1.6195	-0.7319
26.0	-0.0516	1.1316	-0.0728	0.2430	-0.3102	1.0498	0.0802	1.6371	-0.7353
28.0	-0.0480	1.0888	-0.0311	0.2691	-0.2503	0.9681	0.0707	1.6419	-0.7282
30.0	-0.0429	1.0405	0.0144	0.2967	-0.2053	0.8988	0.0633	1.6345	-0.7111

TABLE I-2

DOSE ANGULAR DISTRIBUTIONS - CARBON

Thickness gm/cm^2	Freden-White Spectrum			10 May 1959 Flare Spectrum			23 February 1956 Flare Spectrum		
	a	b	c	a	b	c	a	b	c
0.5	0.2259	1.3701	-0.6121	-0.1327	1.4435	-0.3050	0.2417	1.1808	-0.4284
1.0	0.1529	1.4786	-0.6463	-0.1111	0.8273	0.3046	0.2481	1.1686	-0.4281
2.0	0.0964	1.4427	-0.5492	-0.0188	-0.0065	1.0407	0.2525	1.1446	-0.4042
3.0	0.0689	1.4230	-0.5022	0.0205	-0.3063	1.2895	0.2605	1.1092	-0.3787
4.0	0.0479	1.4278	-0.4848	0.0442	-0.4704	1.4221	0.2655	1.1118	-0.3873
5.0	0.0314	1.4243	-0.4639	0.0545	-0.5387	1.4736	0.2636	1.1361	-0.4108
6.0	0.0174	1.4217	-0.4469	0.0602	-0.5751	1.5044	0.2577	1.1674	-0.4362
7.0	0.0051	1.4203	-0.4321	0.0687	-0.6276	1.5543	0.2504	1.1950	-0.4567
8.0	-0.0051	1.4133	-0.4137	0.0854	-0.7214	1.6355	0.2414	1.2218	-0.4751
9.0	-0.0133	1.3999	-0.3916	0.1058	-0.8243	1.7079	0.2315	1.2478	-0.4930
10.0	-0.0207	1.3875	-0.3725	0.1205	-0.8832	1.7397	0.2203	1.2814	-0.5171
12.0	-0.0332	1.3733	-0.3458	0.1346	-0.8881	1.7148	0.2011	1.3428	-0.5617
14.0	-0.0450	1.3687	-0.3282	0.1380	-0.8053	1.6244	0.1792	1.4126	-0.6112
16.0	-0.0541	1.3561	-0.3043	0.1397	-0.6906	1.5119	0.1562	1.4810	-0.6580
18.0	-0.0601	1.3311	-0.2716	0.1446	-0.5757	1.3977	0.1337	1.5412	-0.6973
20.0	-0.0644	1.3037	-0.2382	0.1524	-0.4613	1.2819	0.1123	1.5966	-0.7322
22.0	-0.0688	1.2702	-0.2010	0.1642	-0.3653	1.1774	0.0917	1.6470	-0.7623
24.0	-0.0677	1.2346	-0.1632	0.1787	-0.2808	1.0808	0.0731	1.6870	-0.7837
26.0	-0.0677	1.1983	-0.1255	0.1951	-0.2049	0.9908	0.0563	1.7206	-0.7993
28.0	-0.0667	1.1611	-0.0878	0.2131	-0.1380	0.9089	0.0415	1.7431	-0.8055
30.0	-0.0649	1.1221	-0.0489	0.2324	-0.0823	0.8371	0.0288	1.7560	-0.8036

TABLE I-3

DOSE ANGULAR DISTRIBUTIONS - ALUMINUM

Thickness gm/cm^2	Freden-White Spectrum			10 May 1959 Flare Spectrum			23 February 1956 Flare Spectrum		
	a	b	c	a	b	c	a	b	c
0.5	0.2235	1.6035	-0.8185	-0.1817	1.9759	-0.7468	0.2204	1.4979	-0.6978
1.0	0.1562	1.4834	-0.6562	-0.1224	0.9778	0.1628	0.2356	1.1549	-0.4027
2.0	0.0958	1.4638	-0.5698	-0.0423	0.1615	0.9057	0.2363	1.1725	-0.4173
3.0	0.0719	1.4160	-0.4969	0.0098	-0.2358	1.2338	0.2457	1.1193	-0.3727
4.0	0.0523	1.4123	-0.4733	0.0342	-0.4174	1.3856	0.2505	1.1166	-0.3761
5.0	0.0365	1.4158	-0.4598	0.0520	-0.5385	1.4801	0.2505	1.1346	-0.3955
6.0	0.0235	1.4090	-0.4403	0.0616	-0.6035	1.5299	0.2451	1.1677	-0.4247
7.0	0.0104	1.4125	-0.4311	0.0689	-0.6566	1.5877	0.2362	1.2085	-0.4574
8.0	-0.0020	1.4227	-0.4288	0.0746	-0.6935	1.6091	0.2258	1.2477	-0.4874
9.0	-0.0140	1.4328	-0.4270	0.0844	-0.7533	1.6609	0.2138	1.2881	-0.5170
10.0	-0.0249	1.4416	-0.4243	0.0957	-0.8153	1.7061	0.2005	1.3311	-0.5481
12.0	-0.0440	1.4506	-0.4138	0.1083	-0.8691	1.7318	0.1758	1.4071	-0.6016
14.0	-0.0600	1.4536	-0.4001	0.1087	-0.8461	1.7017	0.1492	1.4865	-0.6561
16.0	-0.0737	1.4510	-0.3821	0.1039	-0.7898	1.6487	0.1224	1.5603	-0.7046
18.0	-0.0845	1.4376	-0.3561	0.0969	-0.7192	1.5863	0.0959	1.6288	-0.7480
20.0	-0.0931	1.4193	-0.3275	0.0888	-0.6409	1.5179	0.0703	1.6901	-0.7852
22.0	-0.0998	1.3940	-0.2940	0.0798	-0.5574	1.4475	0.0462	1.7462	-0.8180
24.0	-0.1052	1.3662	-0.2593	0.0721	-0.4823	1.3823	0.0226	1.7997	-0.8486
26.0	-0.1092	1.3351	-0.2229	0.0649	-0.4118	1 3207	0.0011	1.8435	-0.8710
28.0	-0.1122	1.3023	-0.1859	0.0584	-0.3468	1.2636	-0.0190	1.8823	-0.8890
30.0	-0.1143	1.2683	-0.1486	0.0522	-0.2857	1.2107	-0.0373	1.9115	-0.8990

TABLE I-4

DOSE ANGULAR DISTRIBUTIONS - IRON

Thickness gm/cm^2	Freden-White Spectrum			10 May 1959 Flare Spectrum			23 February 1956 Flare Spectrum		
	a	b	c	a	b	c	a	b	c
0.5	0.2246	2.3728	-1.5928	-0.3529	3.7842	-2.3877	0.1776	2.4498	-1.6134
1.0	0.1717	1.4265	-0.6167	-0.1280	1.1197	0.0206	0.2063	1.1602	-0.3771
2.0	0.1025	1.4839	-0.5988	-0.0697	0.3861	0.7079	0.1934	1.2461	-0.4505
3.0	0.0733	1.4462	-0.5292	-0.0068	-0.1104	1.1284	0.1870	1.2367	-0.4318
4.0	0.0535	1.4270	-0.4900	0.0202	-0.3172	1.3012	0.1816	1.2288	-0.4203
5.0	0.0371	1.4260	-0.4718	0.0397	-0.4586	1.4186	0.1763	1.2422	-0.4290
6.0	0.0238	1.4247	-0.4557	0.0543	-0.5580	1.4960	0.1686	1.2664	-0.4465
7.0	0.0127	1.4157	-0.4355	0.0622	-0.6135	1.5392	0.1581	1.2985	-0.4691
8.0	0.0020	1.4137	-0.4224	0.0665	-0.6469	1.5680	0.1464	1.3338	-0.4930
9.0	-0.0083	1.4139	-0.4126	0.0708	-0.6785	1.5959	0.1346	1.3664	-0.5143
10.0	-0.0178	1.4176	-0.4067	0.0762	-0.7156	1.6303	0.1227	1.3961	-0.5326
12.0	-0.0337	1.4215	-0.3935	0.0934	-0.8169	1.7105	0.1008	1.4486	-0.5643
14.0	-0.0474	1.4170	-0.3748	0.1062	-0.8808	1.7489	0.0780	1.5006	-0.5947
16.0	-0.0590	1.4087	-0.3543	0.1113	-0.8946	1.7503	0.0557	1.5507	-0.6235
18.0	-0.0691	1.3978	-0.3326	0.1120	-0.8806	1.7311	0.0343	1.5955	-0.6474
20.0	-0.0779	1.3870	-0.3120	0.1101	-0.8487	1.6984	0.0139	1.6363	-0.6686
22.0	-0.0851	1.3719	-0.2886	0.1058	-0.8000	1.6520	-0.0054	1.6720	-0.6858
24.0	-0.0912	1.3541	-0.2638	0.0993	-0.7387	1.5993	-0.0235	1.7051	-0.7013
26.0	-0.0966	1.3360	-0.2388	0.0933	-0.6809	1.5496	-0.0406	1.7347	-0.7142
28.0	-0.1007	1.3121	-0.2099	0.0876	-0.6255	1.5019	-0.0568	1.7611	-0.7243
30.0	-0.1041	1.2881	-0.1815	0.0821	-0.5721	1.4555	-0.0716	1.7827	-0.7308

TABLE I-5

DOSE ANGULAR DISTRIBUTIONS - TUNGSTEN

Thickness gm/cm^2	Freden-White Spectrum			10 May 1959 Flare Spectrum			23 February 1956 Flare Spectrum		
	a	b	c	a	b	c	a	b	c
0.5	0.5020	2.2794	-1.8824	-0.1135	4.5690	-3.6359	0.4318	2.5186	-2.0580
1.0	0.1941	1.5670	-0.7626	-0.1736	1.7571	-0.5511	0.1795	1.4599	-0.6284
2.0	0.1189	1.5275	-0.6614	-0.2139	0.8212	0.3149	0.1804	1.2358	-0.4288
3.0	0.0791	1.5138	-0.6041	-0.0648	0.3252	0.7659	0.1663	1.2835	-0.4600
4.0	0.0574	1.4720	-0.5380	-0.0136	-0.0714	1.1030	0.1691	1.2733	-0.4400
5.0	0.0434	1.4375	-0.4886	0.0147	-0.2822	1.2756	0.1550	1.2513	-0.4139
6.0	0.0308	1.4226	-0.4616	0.0322	-0.4102	1.3799	0.1509	1.2479	-0.4082
7.0	0.0198	1.4189	-0.4463	0.0453	-0.5042	1.4577	0.1466	1.2586	-0.4150
8.0	0.0104	1.4148	-0.4321	0.0566	-0.5812	1.5173	0.1415	1.2722	-0.4243
9.0	0.0021	1.4110	-0.4187	0.0637	-0.6294	1.5540	0.1349	1.2926	-0.4387
10.0	-0.0049	1.4011	-0.4018	0.0679	-0.6594	1.5767	0.1274	1.3156	-0.4546
12.0	-0.0157	1.3862	-0.3760	0.0722	-0.6923	1.6043	0.1156	1.3503	-0.4780
14.0	-0.0282	1.3874	-0.3645	0.0766	-0.7262	1.6379	0.1013	1.3876	-0.5002
16.0	-0.0375	1.3769	-0.3436	0.0882	-0.7988	1.7006	0.0876	1.4128	-0.5124
18.0	-0.0456	1.3658	-0.3233	0.1019	-0.8755	1.7547	0.0746	1.4357	-0.5231
20.0	-0.0516	1.3477	-0.2985	0.1119	-0.9264	1.7877	0.0625	1.4566	-0.5320
22.0	-0.0567	1.3288	-0.2738	0.1191	-0.9588	1.8069	0.0511	1.4744	-0.5386
24.0	-0.0607	1.3092	-0.2496	0.1243	-0.9759	1.8139	0.0402	1.4912	-0.5449
26.0	-0.0642	1.2903	-0.2263	0.1272	-0.9769	1.8073	0.0303	1.5058	-0.5497
28.0	-0.0666	1.2685	-0.2013	0.1275	-0.9605	1.7890	0.0212	1.5166	-0.5515
30.0	-0.0686	1.2488	-0.1765	0.1269	-0.9376	1.7671	0.0126	1.5277	-0.5537

APPENDIX II

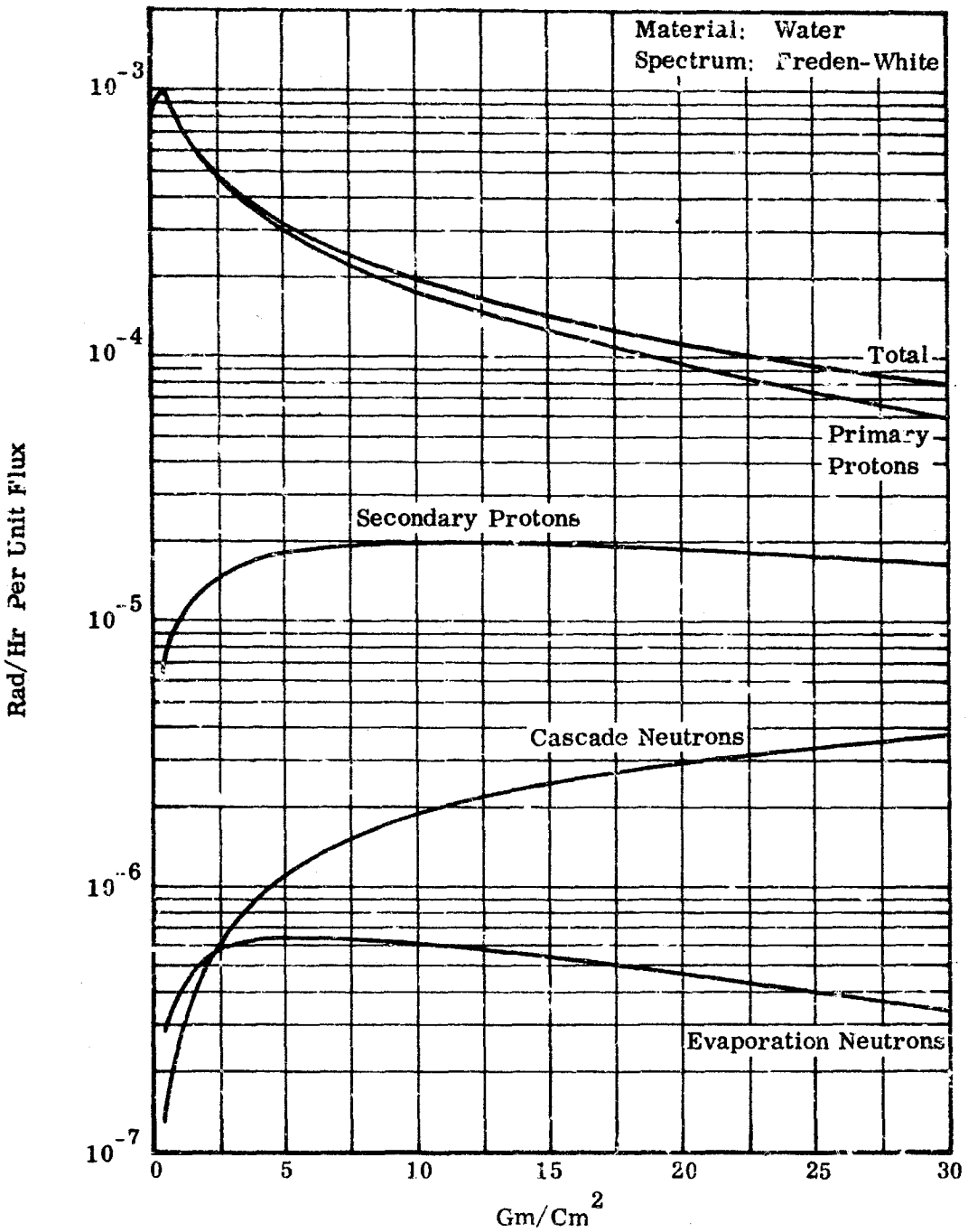

FIGURE II-1 DOSAGE AS A FUNCTION OF THICKNESS

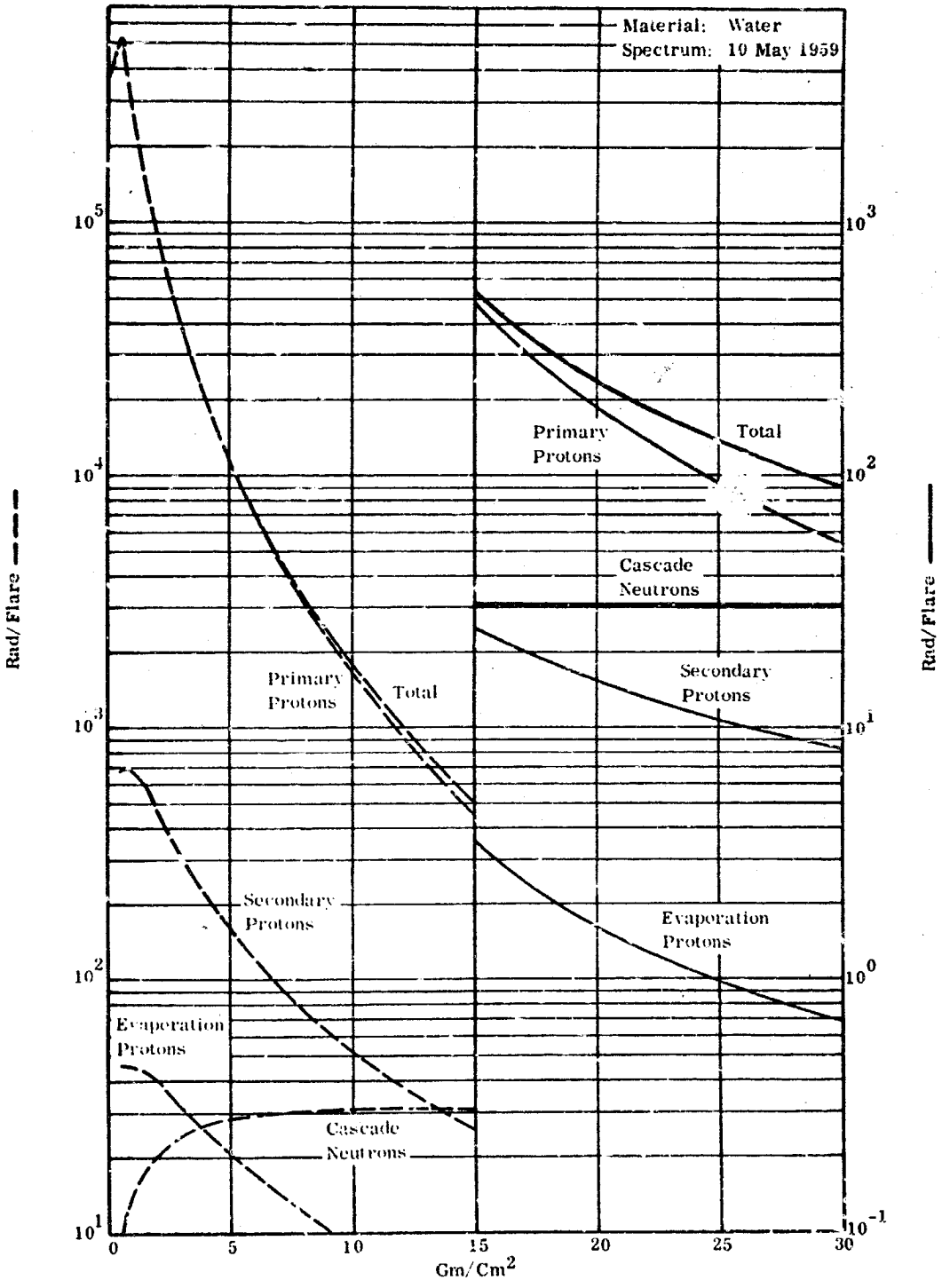

FIGURE II-2 DOSAGE AS A FUNCTION OF THICKNESS

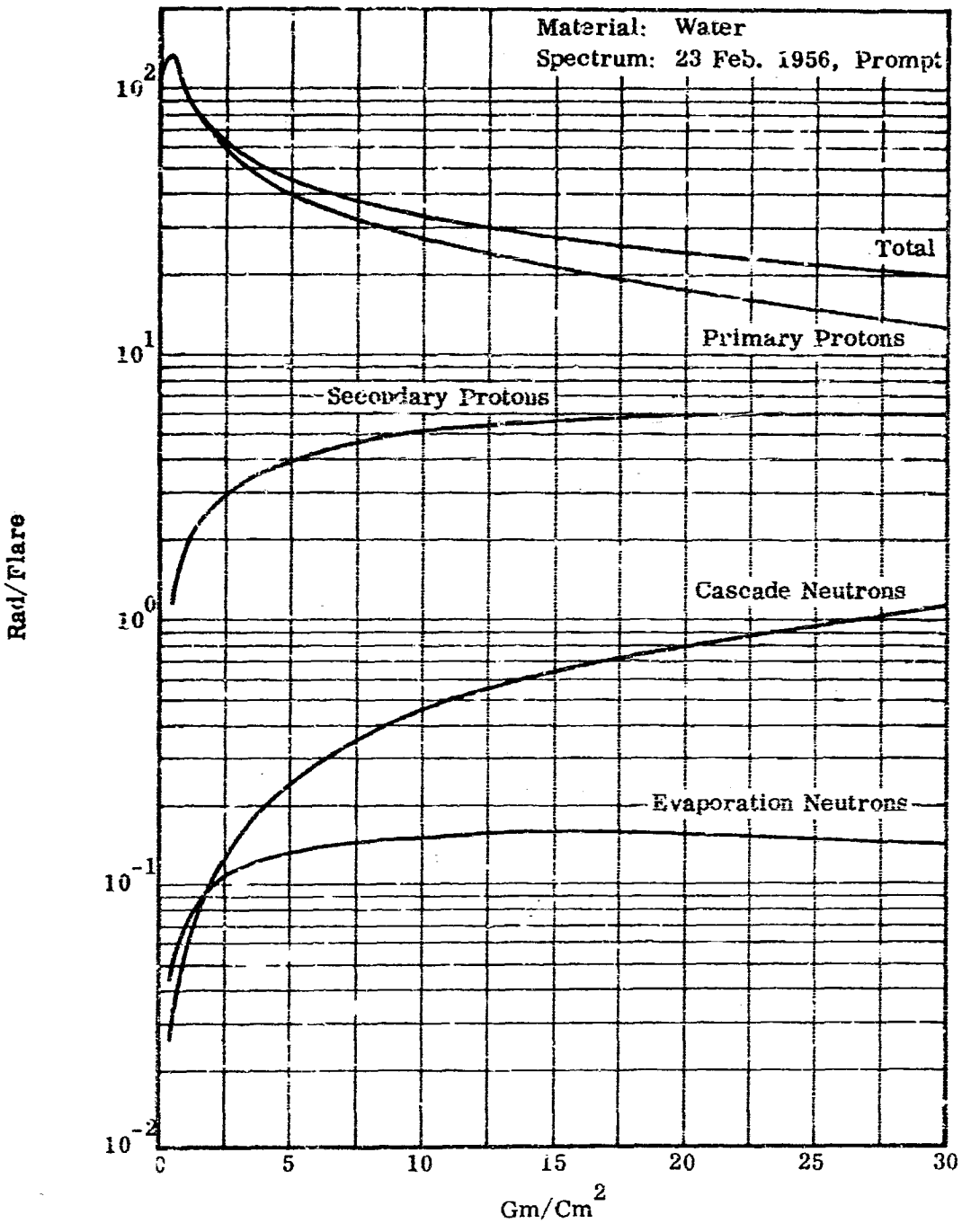

FIGURE II-3 DOSAGE AS A FUNCTION OF THICKNESS

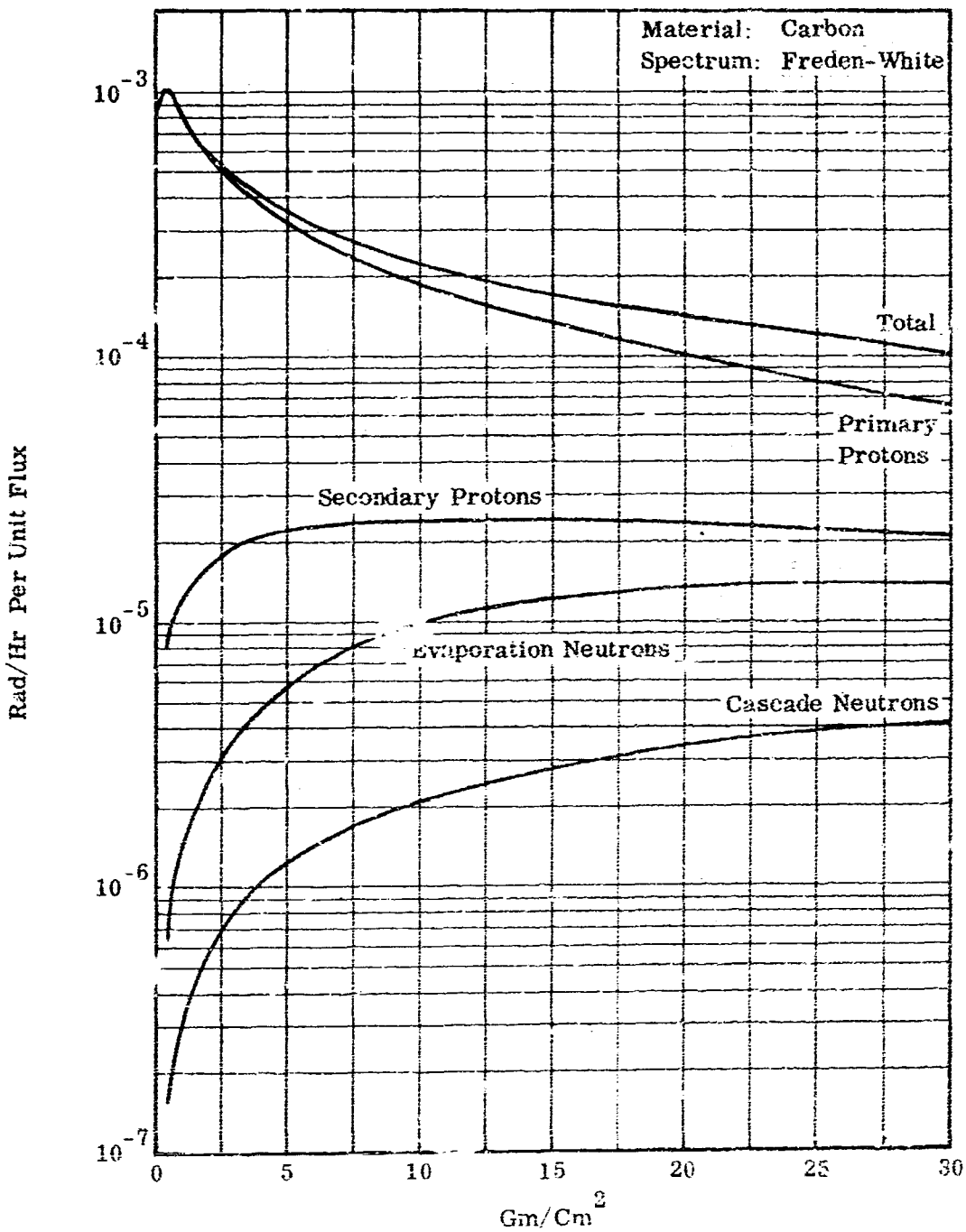

FIGURE II-4 DOSAGE AS A FUNCTION OF THICKNESS

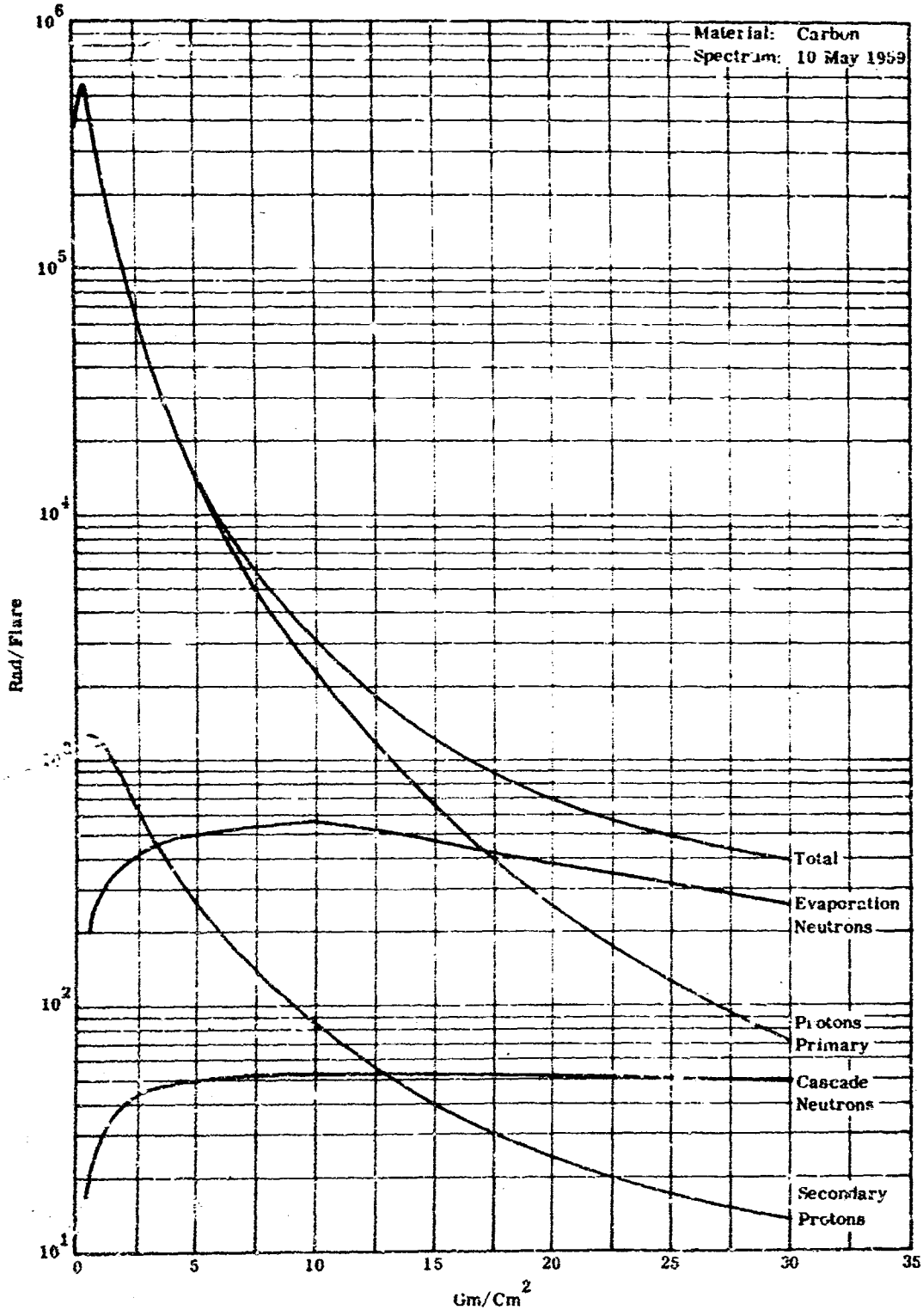

FIGURE II-5 DOSAGE AS A FUNCTION OF THICKNESS

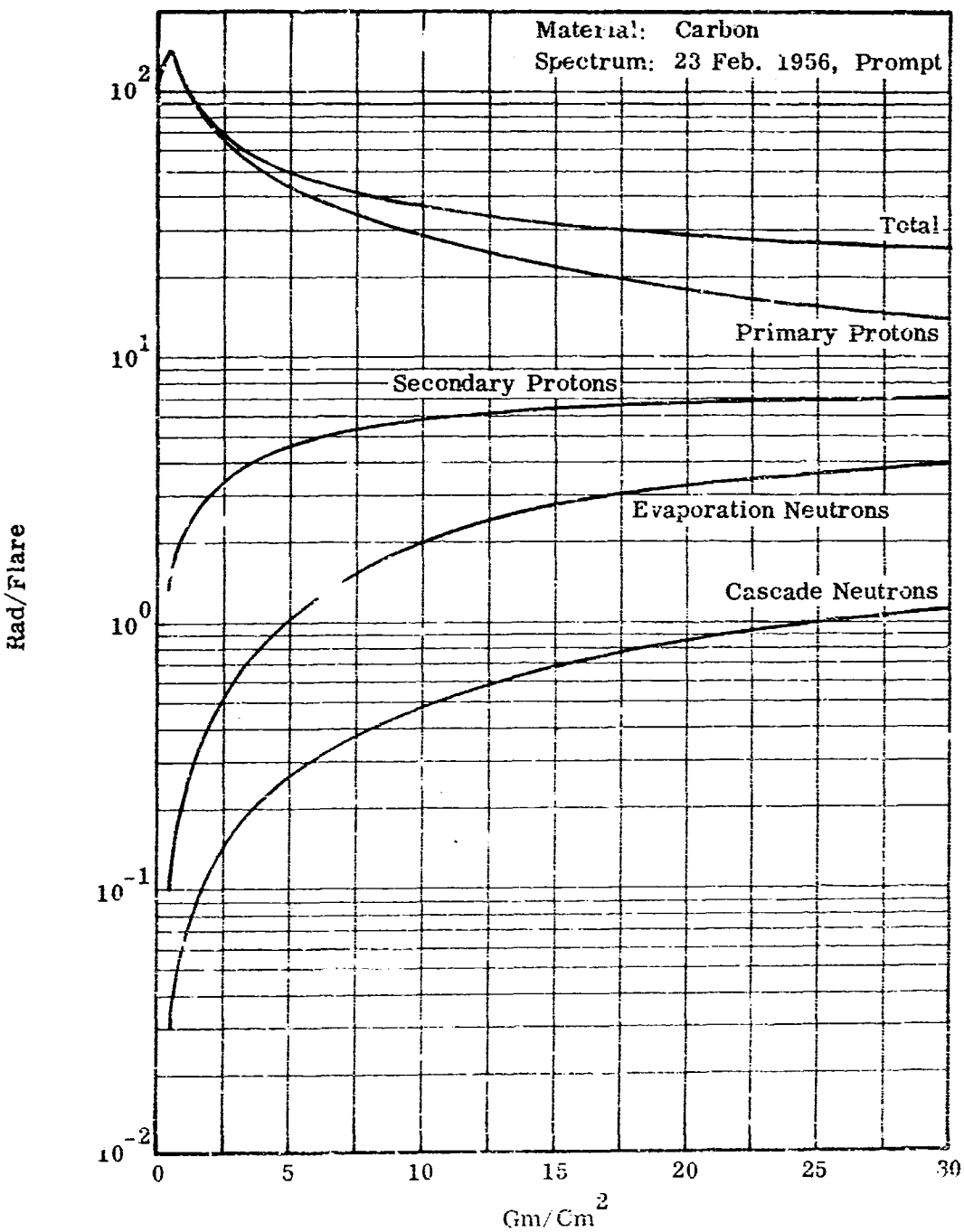

FIGURE II-6 DOSAGE AS A FUNCTION OF THICKNESS

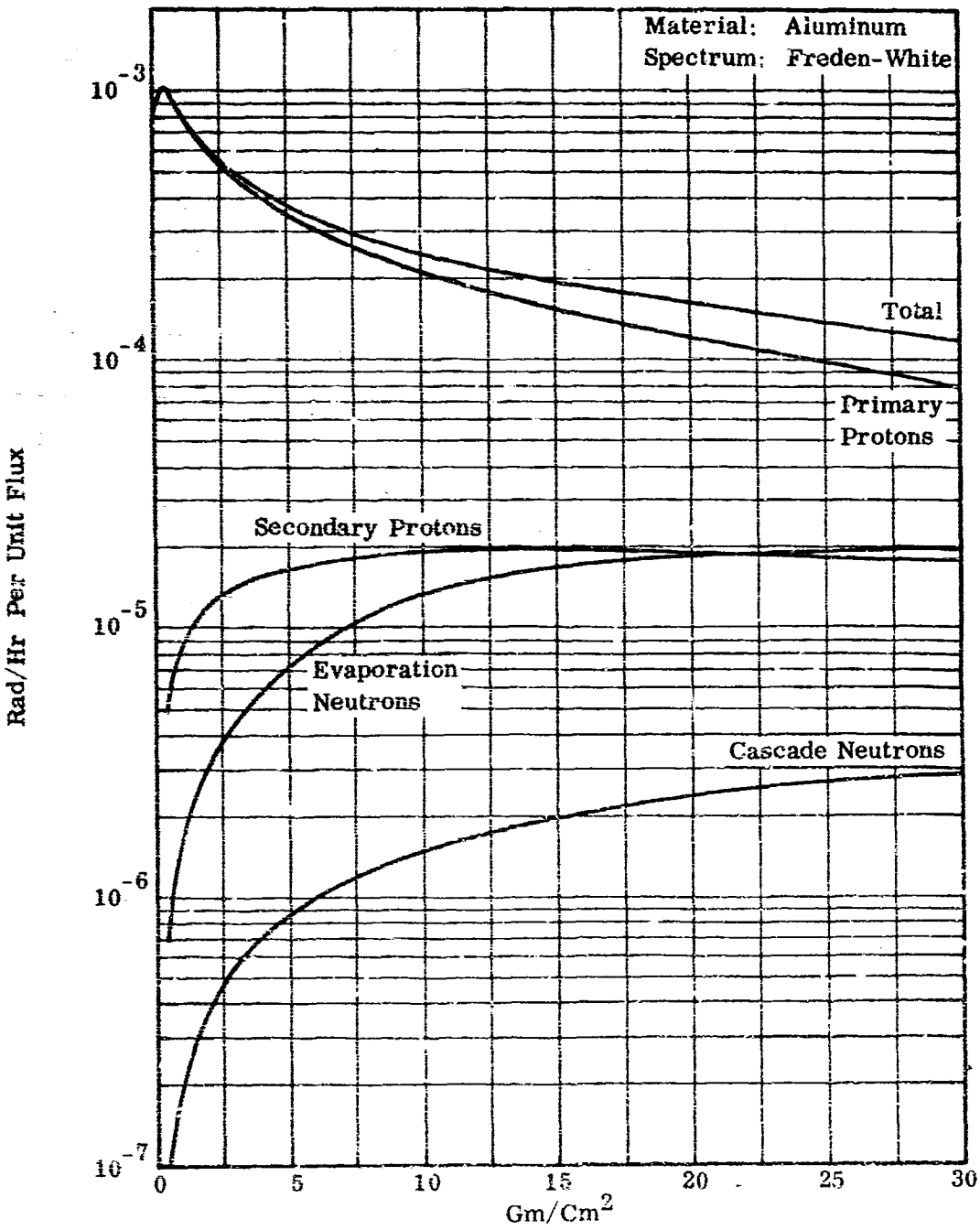

FIGURE II-7 DOSAGE AS A FUNCTION OF THICKNESS

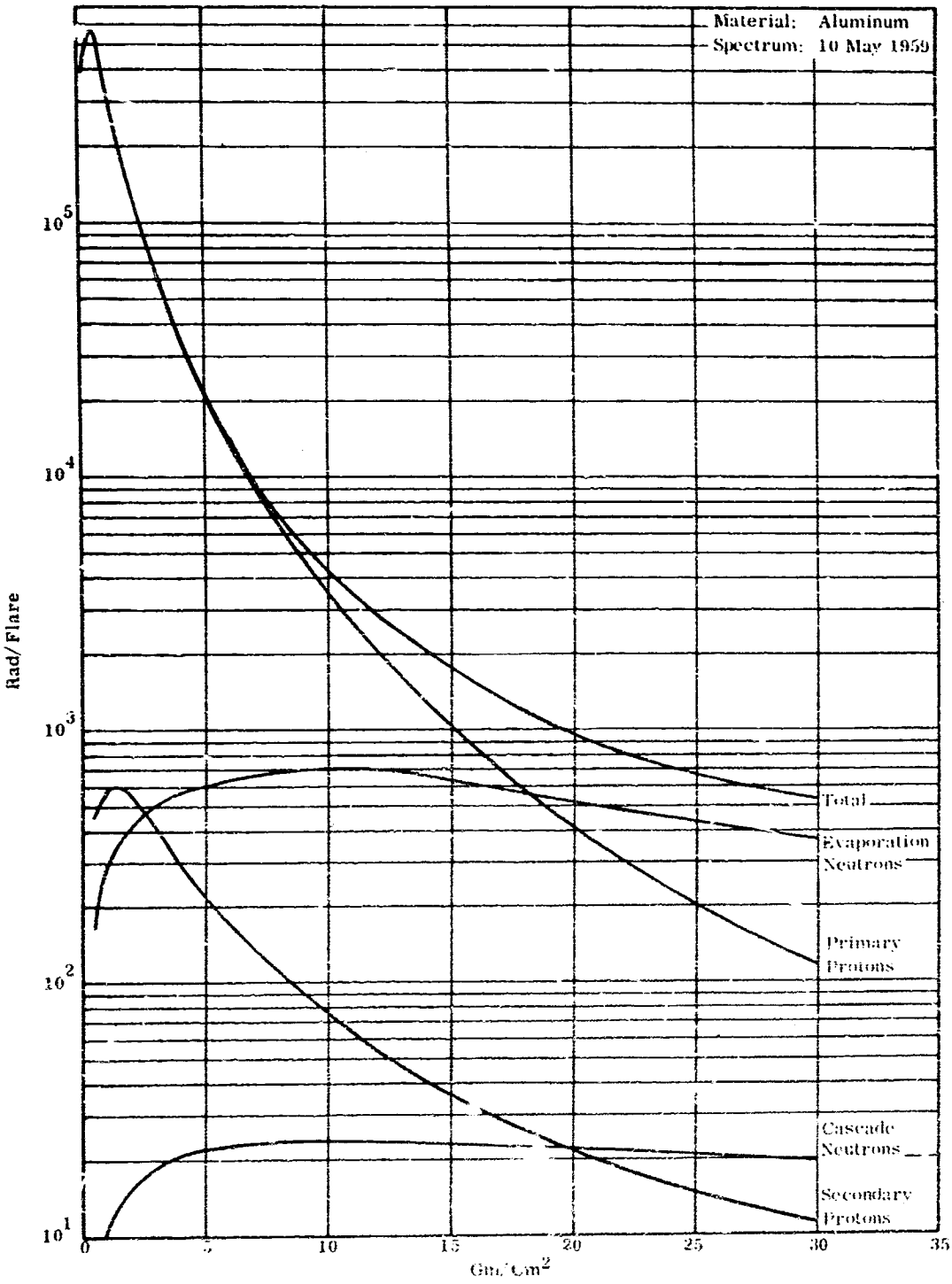

FIGURE II-8 DOSAGE AS A FUNCTION OF THICKNESS

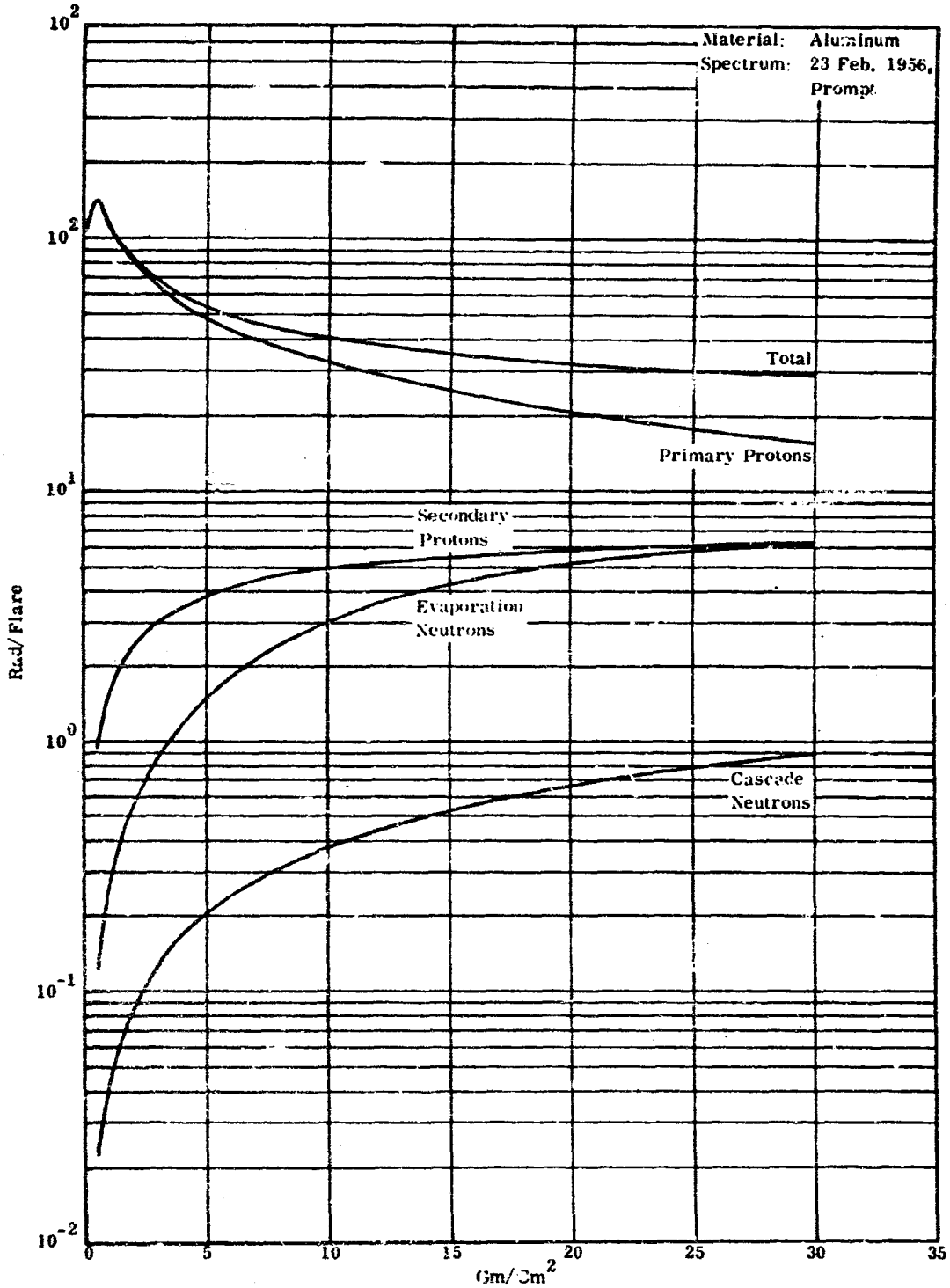

FIGURE II-9 DOSAGE AS A FUNCTION OF THICKNESS

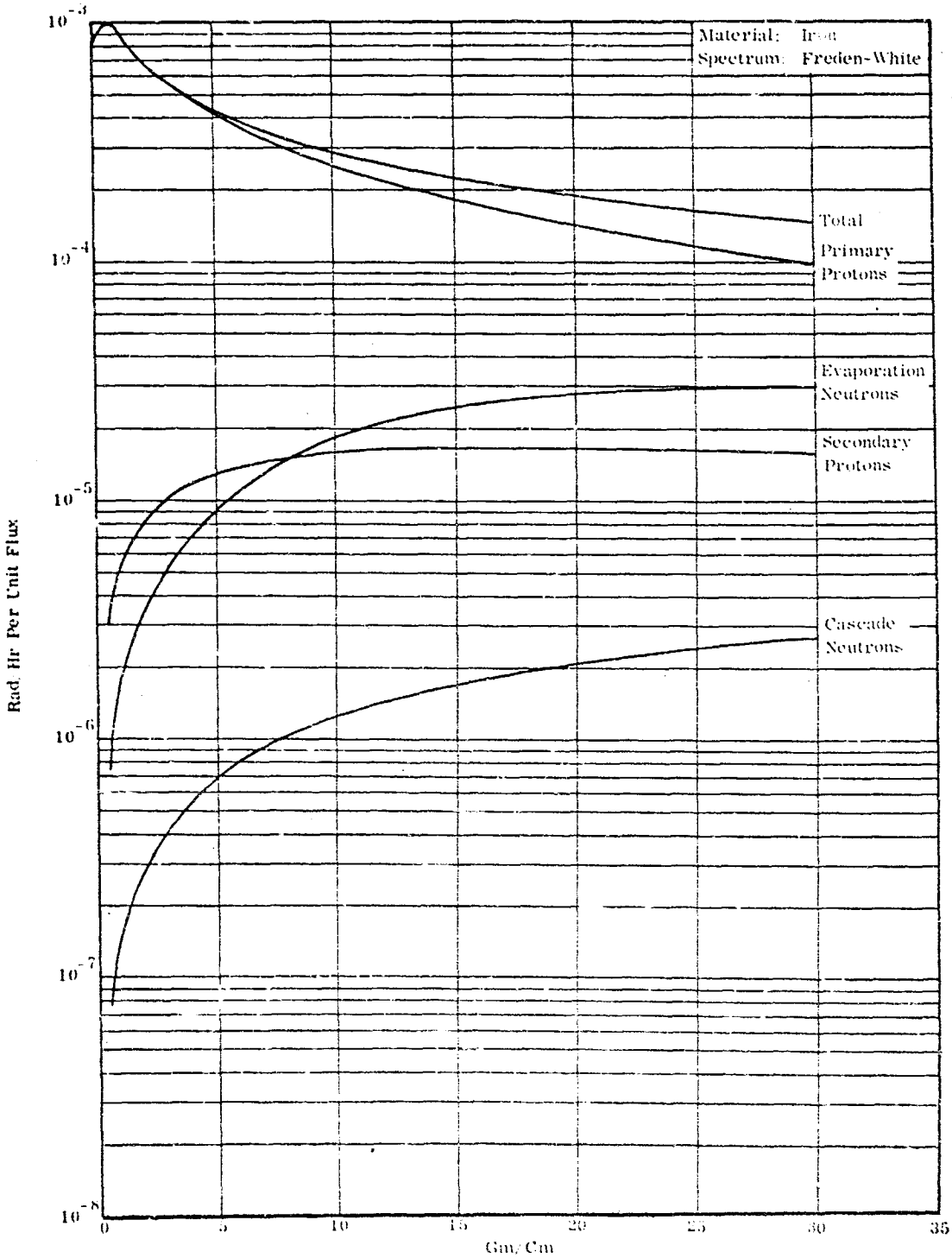

FIGURE II-10 LOSAGE AS A FUNCTION OF THICKNESS

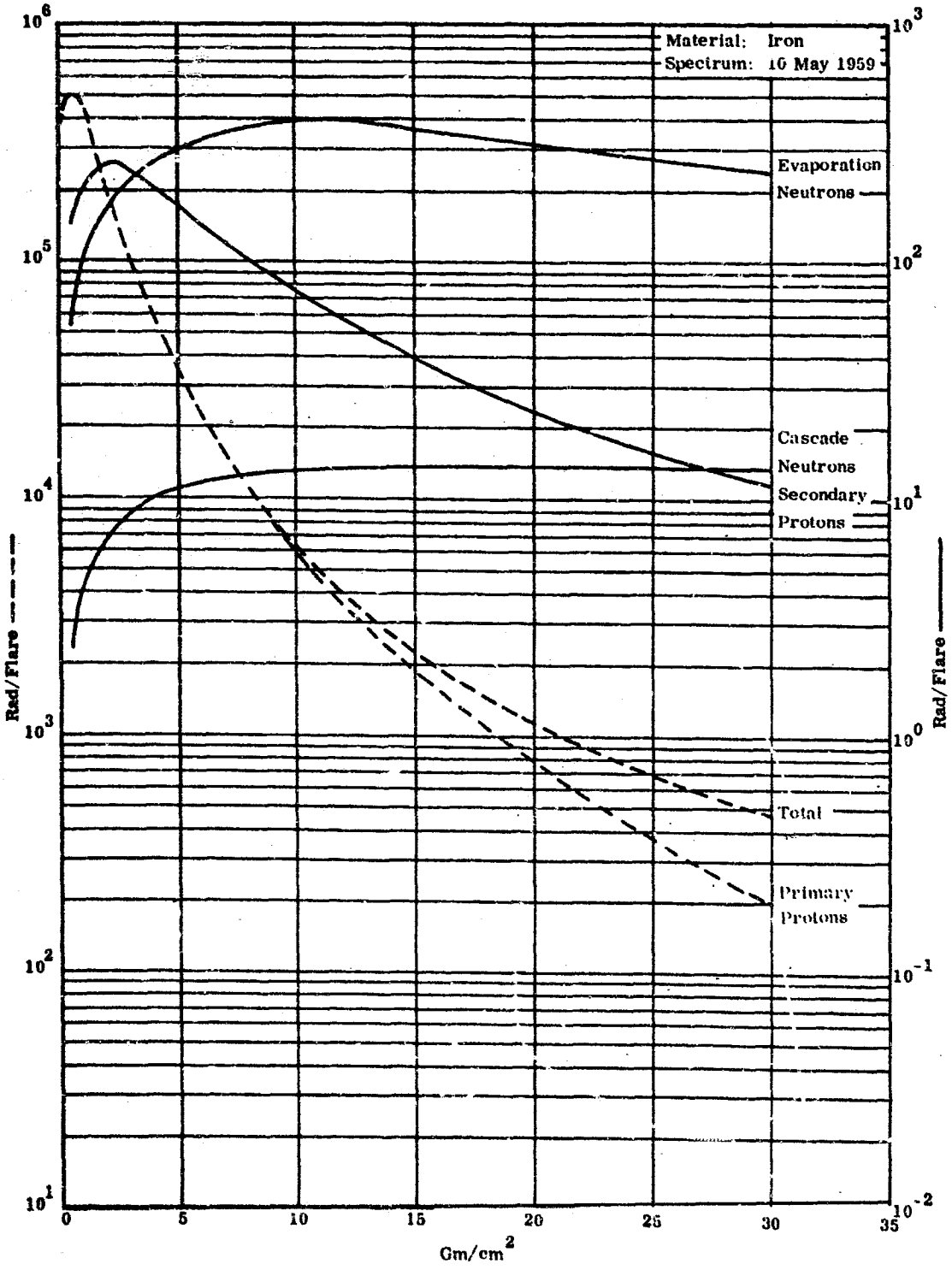

FIGURE II-11 DOSAGE AS A FUNCTION OF THICKNESS

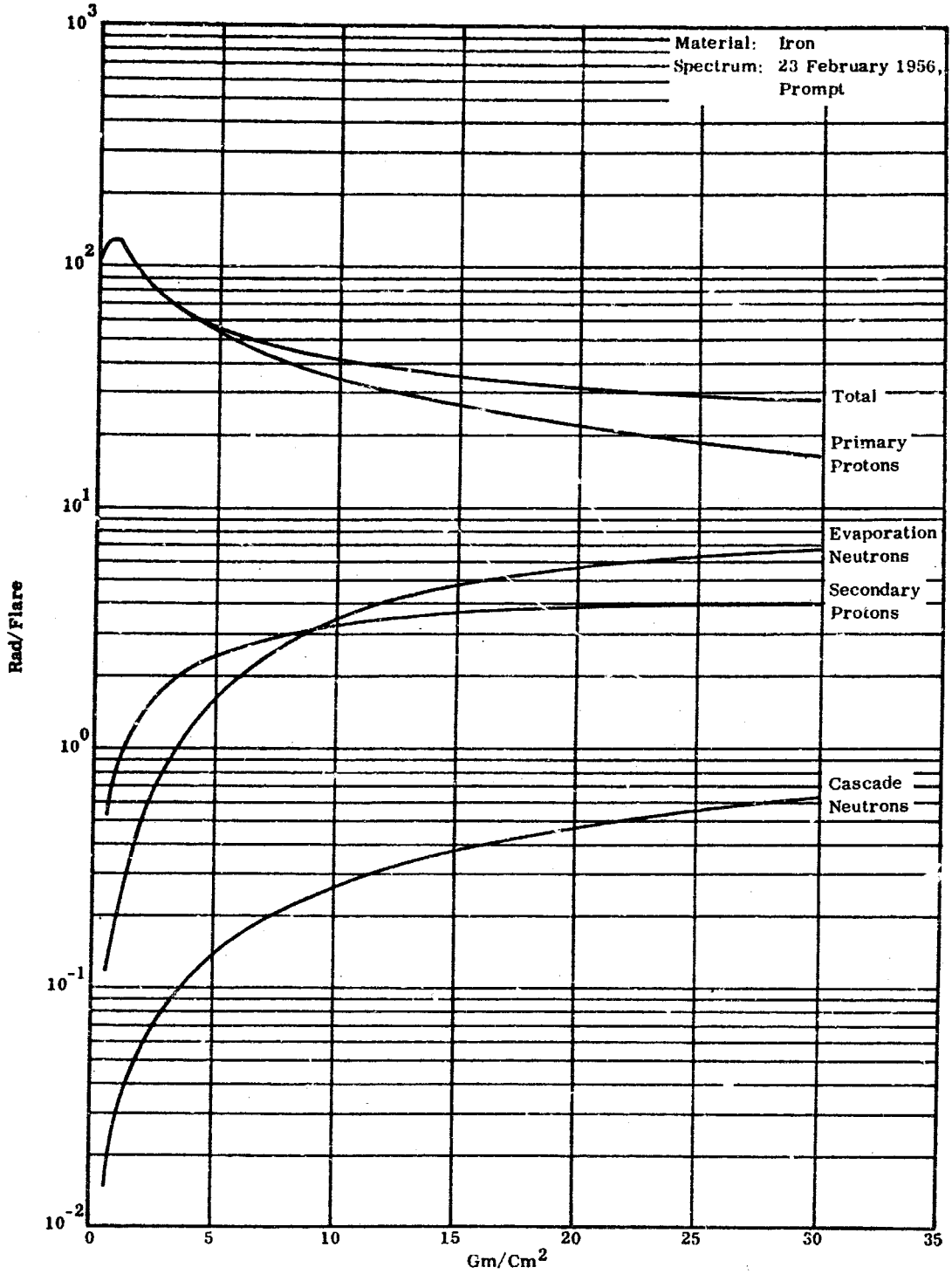

FIGURE II-12 DOSAGE AS A FUNCTION OF THICKNESS

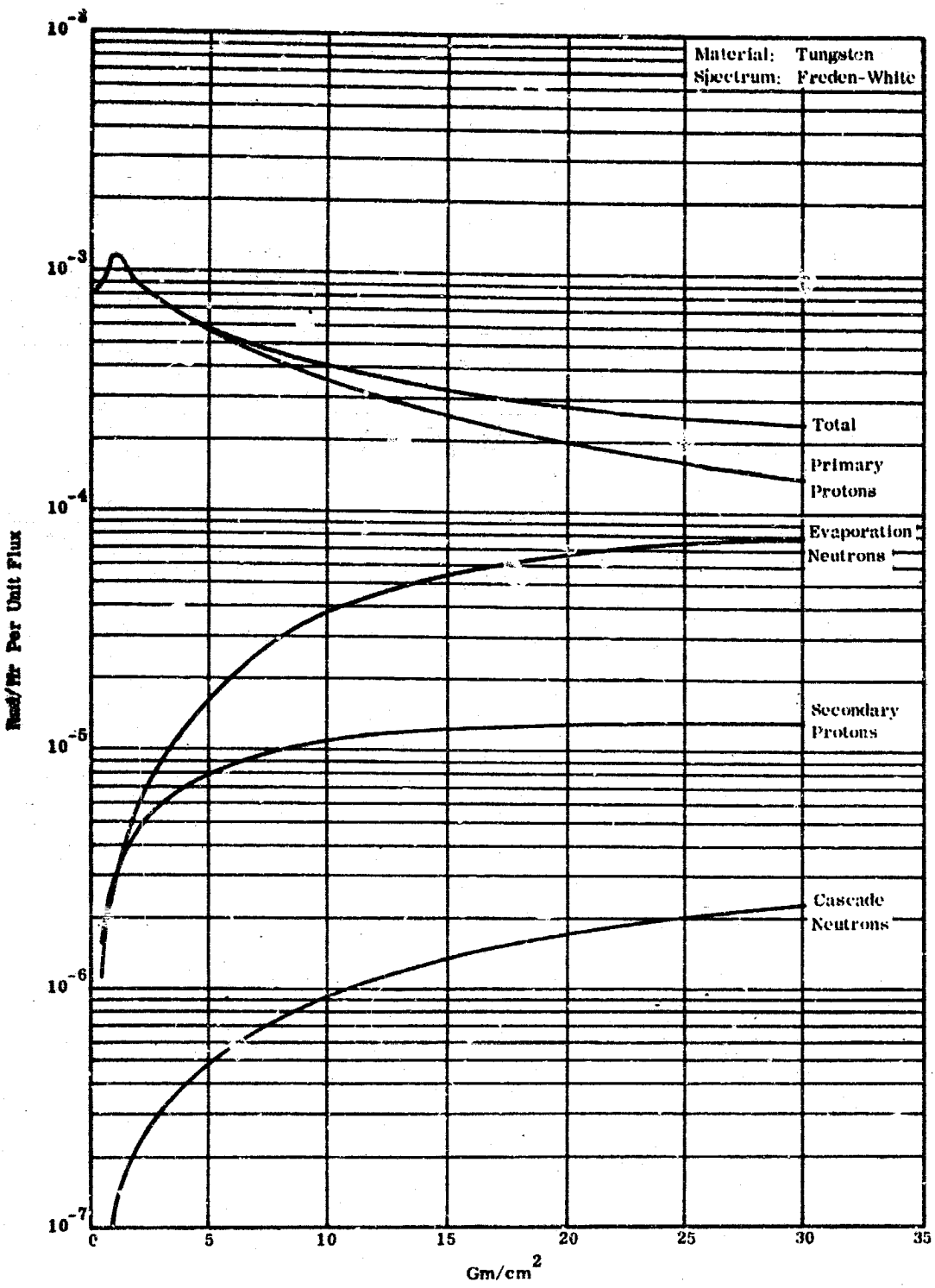

FIGURE II-13 DOSAGE AS A FUNCTION OF THICKNESS

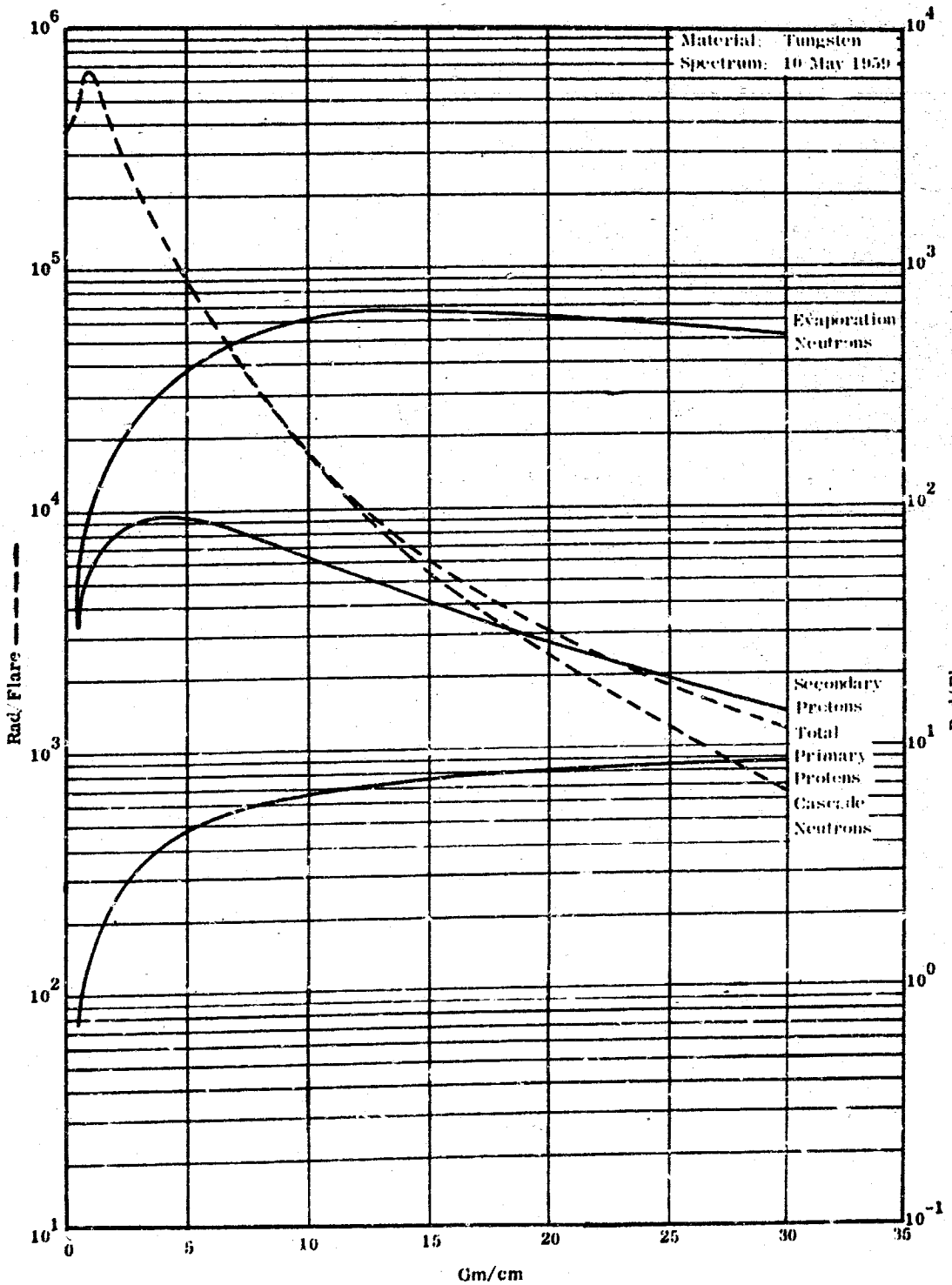

FIGURE II-1[illegible] DOSAGE AS A FUNCTION OF THICKNESS

APPENDIX III

```
CSOURCE     GENERATES SOURCE TERM PACKAGE FOR LPPC
      DIMENSIONH(12),FEI(50),EI(50),A(49),B(49),FEJ(250),
     1BL(49),L(10),FI(250),R(50),PIR(50),E(250),EIL(50),
     2FIA(250),FIT(250),EJ(250),AL(49),FEIL(50),KD(3)
      CALLTAPE(3,IN,IOT,IPH)
      C1=1876./2.
      C2=C1**2
    2 READINPUTTAPEIN,1000,H
C
C     IPT=1, INTEGRAL RIGIDITY SPECTRUM
C     IPT=2, INTEGRAL ENERGY SPECTRUM
C     IPT=3, DIFFERENTIAL RIGIDITY SPECTRUM,
C     IPT=4, RIGIDITY POWER LAW
C     IPT=5,INTEGRAL ENERGY POWER LAW
C
      READINPUTTAPEIN,1002,NEI,IPT
      GO TO (10, 11, 14, 100, 103), IPT
   10 READINPUTTAPEIN,1001,(R(I),I=1,NEI)
      DO12I=1,NEI
   12 EI(I)=SQRTF(R(I)**2+C2)-C1
      GOTO13
   11 READINPUTTAPEIN,1001,(EI(I),I=1,NEI)
   13 READINPUTTAPEIN,1001,(FEI(I),I=1,NEI)
      GOTO15
   14 READINPUTTAPEIN,1001,(R(I),I=1,NEI)
      READINPUTTAPEIN,1001,(PIR(I),I=1,NEI)
      DO16I=1,NEI
      FEJ(I)=PIR(I)*SQRTF(R(I)**2+C2)/R(I)
   16 EJ(I)=SQRTF(R(I)**2+C2)-C1
      NEJ=NEI
      GOTO16
  100 READ INPUT TAPE IN, 1001, AA, BB, (R(I), I=1,NEI)
      DO 101 I=1,NEI
  101 FEI(I)=(AA*R(I)**(-BB))
      DO 102 I=1,NEI
  102 EI(I)=SQRTF(R(I)**2+C2)-C1
      GO TO 15
  103 READ INPUT TAPE IN, 1001, AA, BB, (EI(I), I=1,NEI)
      DO 104 I=1,NEI
  104 FEI(I)=(AA*EI(I)**(-BB))
C
   15 CONTINUE
      DO 300 I=1,NEI
      EIL(I)=LOGF(EI(I))
      FEIL(I)=LOGF(FEI(I))
  300 CONTINUE
```

```
      READINPUTTAPE5N,1001,EMAX,EMIN,EB1,EB2,EB3,DEL1,DEL2,
     1DEL3,DEL4
      A=0.
      SENSE LIGHT 0
      EJ(1)=EMIN
      J=2
  200 IF(EJ(J-1)-EB1)205,206,201
  201 IF(EJ(J-1)-EB2)206,207,202
  202 IF(EJ(J-1)-EB3)207,208,203
  203 IF(EJ(J-1)-EMAX)208,204,204
  204 NEJ=J-1
      GOTO210
  205 EJ(J)=EJ(J-1)+DEL1
      GOTO209
  206 EJ(J)=EJ(J-1)+DEL2
      IF(SENSE LIGHT 2)306,307
  307 CONTINUE
      SENSE LIGHT 2
      KD(1)=J
  306 CONTINUE
      GOTO209
  207 EJ(J)=EJ(J-1)+DEL3
      IF(SENSE LIGHT 3)308,309
  309 CONTINUE
      SENSE LIGHT 3
      KD(2)=J
  308 CONTINUE
      GOTO209
  208 EJ(J)=EJ(J-1)+DEL4
      IF(SENSE LIGHT 4)310,311
  311 CONTINUE
      SENSE LIGHT 4
      KD(3)=J
  310 CONTINUE
  209 J=J+1
      IF(J-250)200,200,204
  210 CONTINUE
      DO 301 J=1,NEJ
      E(J)=LOGF(EJ(J))
      L(1)=XLOCF(L(1))
      L(2)=XLOCF(EIL(1))
      L(3)=XLOCF(FEIL(1))
      L(4)=1
      L(5)=1
      L(6)=3
      L(7)=NEJ
      L(8)=0
```

```
      FIT(J)=TABF(E(J),L(1))
      I=L(8)
      GO TO (312,313),I
  313 CONTINUE
      WRITE OUTPUT TAPE IOT,1008
 1008 FORMAT(16H1TAB FAIL FIT(J))
      CALL EXIT
  312 CONTINUE
C
C
      FIA(J)=EXPF(FIT(J))
  301 CONTINUE
C
C     CALC FIRST POINT
      DE=E(1)-E(2)
      DFIT=FIT(1)-FIT(2)
      FEJ(1)=-FIA(1)*DFIT/(EJ(1)*DE)
C
      NEJM=NEJ-1
      DO 304 J=2,NEJM
      IF((J+1)-KD(1))303,314,315
  314 CONTINUE
      DD=DEL1
      GO TO 320
  315 CONTINUE
      IF((J+1)-KD(2))303,316,317
  316 CONTINUE
      DD=DEL2
      GO TO 320
  317 CONTINUE
      IF((J+1)-KD(3))303,318,319
  318 CONTINUE
      DD=DEL3
  319 CONTINUE
      GO TO 303
  320 CONTINUE
      A=FIT(J+1)
      EE=LOGF(EJ(J)+DD)
      FIT(J+1)=TABF(EE,L(1))
      DE=E(J-1)-EE
      GO TO 3031
C
  303 CONTINUE
      DE=E(J-1)-E(J+1)
 3031 CONTINUE
      DFIT=FIT(J-1)-FIT(J+1)
      FEJ(J)=-FIA(J)*DFIT/(EJ(J)*DE)
```

```
      IF(A)321,304,321
  321 CONTINUE
      FIT(J+1)=A
      A=0.
  304 CONTINUE
C
      NEJ=J
      DE=E(J-1)-E(J)
      DFIT=FIT(J-1)-FIT(J)
      FEJ(J)=-FIA(J)*DFIT/(EJ(J)*DE)
C
   18 DO4J=1,NEJ
      N=NEJ+1-J
    4 FI(J)=TRINTF(XLOCVF(FEJ(J)),XLOCVF(EJ(J)),N)
      WRITEOUTPUTTAPEIOT,1003,H,IPT
      GO TO (19,19,20,19,19),IPT
   19 WRITEOUTPUTTAPEIOT,1005,(EI(I),FEI(I),I=1,NEI)
   20 WRITEOUTPUTTAPEIOT,1007,(EJ(I),FEJ(I),FI(I),I=1,NEJ)
      WRITEOUTPUTTAPEIPH,1006,NEJ,H,(EJ(I),FEJ(I),I=1,NEJ)
      GOTO2
 1000 FORMAT(12A6)
 1001 FORMAT(8E9.)
 1002 FORMAT(1415)
 1003 FORMAT(1H112A6,8HOPTION =I2)
 1005 FORMAT(6H0INPUT/6X1HE7X8HINTEGRAL/(1P2E12.4))
 1006 FORMAT(I3,12A6/(1P6E10.3))
 1007 FORMAT(7H0OUTPUT/6X1HE9X6HPHI(E)4X8HINTEGRAL/(1P3E12.4))
      END
```